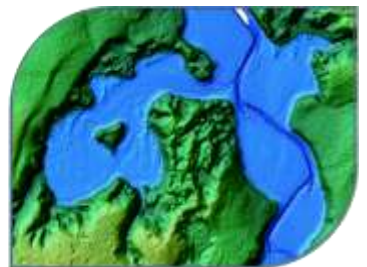
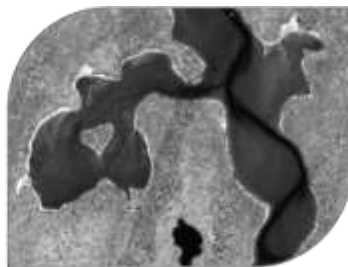
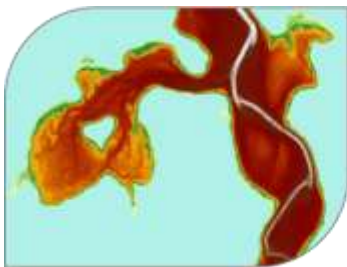


Topo-bathymetric Lidar Research for Aquaculture and Coastal Development in Nova Scotia: Final Report



Prepared by

Applied Geomatics Research Group
NSCC, Middleton
Tel. 902 825 5475
email: tim.webster@nsc.ca

Submitted to

Bill Whitman
Nova Scotia Department of Fisheries and
Aquaculture

March 31, 2017

How to cite this work and report:

AGRG. 2017. Topo-bathymetric Lidar Research for Aquaculture and Coastal Development in Nova Scotia: Final Report. Technical report, Applied Geomatics Research Group, NSCC Middleton, NS.

Copyright and Acknowledgement

The Applied Geomatics Research Group of the Nova Scotia Community College maintains full ownership of all data collected by equipment owned by NSCC and agrees to provide the end user who commissions the data collection a license to use the data for the purpose they were collected for upon written consent by AGRG-NSCC. The end user may make unlimited copies of the data for internal use; derive products from the data, release graphics and hardcopy with the copyright acknowledgement of **“Data acquired and processed by the Applied Geomatics Research Group, NSCC”**. Data acquired using this technology and the intellectual property (IP) associated with processing these data are owned by AGRG/NSCC and data will not be shared without permission of AGRG/NSCC.

Executive Summary

Three shallow, highly productive, eelgrass-rich estuaries on Nova Scotia's Northumberland Strait were surveyed in July 2016 using aerial topo-bathymetric lidar to collect seamless land-sea elevation and imagery data. AGRG's Chiroptera II integrated topo-bathymetric lidar sensor, equipped with a 60 megapixel multispectral camera, was used to survey Pugwash River and River Philip, Merigomish Harbour, and Mabou Harbour.

In Pugwash-River Philip the lidar was successful in penetrating the rivers up to the edge of the deep channels, where water clarity and depth combined to prevent lidar penetration; maximum penetration was ~-5 m CGVD28 in Pugwash Harbour (note, all elevations reported are referenced to CGVD28). In Merigomish Harbour the lidar penetrated to the seabed in most of the harbour outside of the deep channels, and maximum lidar penetration was ~-6.5 m near the seaward edge of the study area. At Mabou Harbour the lidar penetrated to ~-13 m in the clear water outside of the harbour but only to ~-6 m in the inner harbour where water clarity was poor.

The lidar data were validated using RTK GPS separately for topographic and bathymetric data points. The topographic validation was within the accuracy specs for the sensor (<0.1 m), and the bathymetric validation resulted in a negative mean ΔZ in all areas (<-0.25 m), an indication that the DEMs were shallower than the observed GPS points. This error was most pronounced in areas with thick vegetation on the seabed, and it is possible that the laser was unable to penetrate through the eelgrass canopy to the seabed.

AGRG researchers collected survey grade GPS points in each of the areas and measured water clarity, depth, and underwater photos of the seabed conditions and bottom type. Eelgrass maps were derived from the lidar and orthophotos and illustrate the presence of eelgrass throughout the study area. The study area at Pugwash-River Philip was classified as having 28% eelgrass coverage with 80% accuracy; at Merigomish 33% of the lidar study area had eelgrass coverage, with 83% accuracy; and at Mabou 27% of the study area had eelgrass, with 84% agreement with underwater imagery and 59% agreement with acoustic vegetation mapping.

Hydrodynamic models were developed to simulate current flow and water level variations within each study area. Acoustic Doppler Current Profilers were deployed by AGRG and DFO in each of the areas to measure the water level and current speeds throughout a tidal cycle to be used for model validation. The models were successful at simulating tidal elevations and currents at the ADCPs, and the two-dimensional model results show circulation throughout the study areas.

Table of Contents

Executive Summary.....	ii
Table of Contents.....	iii
Table of Figures.....	v
List of Tables.....	x
1 Introduction.....	1
1.1 Project Background.....	1
1.2 Study Area.....	1
2 Methods.....	2
2.1 Sensor Specifications.....	2
2.2 Lidar Survey Details.....	4
2.3 Ground Truth Data Collection.....	5
2.4 Time of Flight Conditions: Weather, Tide and Turbidity.....	2
2.5 Elevation Data Processing.....	6
2.5.1 Lidar processing.....	6
2.5.2 Ellipsoidal to Orthometric Height Conversion.....	9
2.5.3 Bottom Classification Maps.....	9
2.6 Lidar Validation.....	10
3 Results.....	10
3.1 Lidar Validation.....	10
3.1.1 Topographic Validation.....	10
3.1.2 Bathymetric Validation.....	11
3.2 Surface Models and Air Photos.....	12
3.2.1 Pugwash-River Philip.....	12
3.2.2 Merigomish.....	16
3.2.3 Mabou.....	20

3.3	Depth Distribution	25
3.4	Bottom Imagery.....	26
3.4.1	Pugwash-River Philip.....	26
3.4.2	Merigomish	28
3.4.3	Mabou	30
3.5	Bottom Classification Maps.....	33
3.5.1	Submerged Aquatic Vegetation Maps	33
3.5.2	Bottom Classification Maps.....	37
4	Hydrodynamic Modelling	39
4.1	Modelling Methods	39
4.1.1	Grid Preparation.....	39
4.1.2	Boundary Conditions.....	44
4.1.3	Model Parameters and Calibration	45
4.2	Modelling Validation and Results	47
4.2.1	Pugwash-River Philip.....	47
4.2.2	Merigomish	51
4.2.3	Mabou	58
5	Discussion and Conclusions.....	63
6	References.....	64
7	Acknowledgements.....	64
8	Appendix: Oceanographic Data.....	65
8.1	ADCP	65
8.1.1	PWRP	65
8.1.2	Merigomish	66
8.1.3	Mabou	68
	CTD.....	70

8.1.4 PWRP 70

8.1.5 Mabou 72

Table of Figures

Figure 1.1: The topographic-bathymetric lidar study areas in the Southern Gulf of St. Lawrence surveyed in July 2016 showing NS High Precision Network (HPN) stations (orange squares) and Environment Canada (EC) Weather Stations (green triangles)..... 2

Figure 2.1: (A) Example of the Chiroptera II green laser waveform showing the large return from the sea surface and smaller return from the seabed. (B) Schematic of the Chiroptera II green and NIR lasers interaction with the sea surface and seabed (adapted from Leica Geosystems). 3

Figure 2.2: (a) Aircraft used for 2016 lidar survey; (b) display seen by lidar operator in-flight; (c) main body of sensor (right) and the data rack(left); (d) large red circles are the lasers; the RCD30 lens (right) and low resolution camera quality control(left). 3

Figure 2.3: Flight lines for the 2016 study areas (A) Pugwash/River Philip, (B) Merigomish, and (C) Mabou. 5

Figure 2.4: Location of hard surface GPS validation points, AGRG and DFO boat-based ground truth waypoints at (A) Pugwash/River Philip, (B) Merigomish and (C) Mabou. The location of the ADCP deployed in Merigomish by DFO is unknown at this time, no CTD measurements were obtained in Merigomish, and a cube was deployed in Pugwash only. 6

Figure 2.5: Ground truth data collection at Pugwash and River Phillip. (a) Base station setup, (b) RiverRay ADCP being towed by AGRG boat, (c) ADCP deployment (d) cube, (e) AGRG and NSFA collaborating in Pugwash, (f) CTD..... 1

Figure 2.6: Ground truth data collection in Merigomish. (a) seabed elevation measurement with GPS antenna threaded onto pole, (b) AGRG and NSFA collaborating in Merigomish, (c) 0.25 m² quadrat being deployed, (d, e) clear water in Merigomish during the aerial and ground truth survey, (f) healthy eelgrass..... 1

Figure 2.7: Ground truth data collection in Mabou. (a) Base station setup, (b) RiverRay ADCP being towed from inflatable boat, (c) turbidity buoy on deployment data (July 13), (d) Humminbird echosounder for depth measurement, (e) GPS gear on both NSFA and AGRG boats in Mabou, (f) NSFA and AGRG collaboration in Mabou. 2

Figure 2.8: Caribou meteorological data (a) wind speed; (b) wind direction; (c) wind vectors indicating speed and direction wind is blowing towards; (d) daily rainfall; (e) predicted tide at River Phillip and Merigomish in Chart Datum. Lidar surveys at PWRP and MERI are highlighted in orange and green, respectively. Time axis is in UTC time zone. 3

Figure 2.9: (a- c): Wind speed and direction data recorded at Port Hawkesbury; (d) daily rainfall recorded at Cheticamp; (e) predicted tide at Port Hood in Chart Datum; (f) turbidity measured by AGRG buoy. The attempted and completed lidar surveys are highlighted in orange. Time axis is in UTC time zone..... 4

Figure 2.10: (a) High turbidity at Mabou on July 13; (b) varying turbidity during ground truth on July 21; (c) red sandstone cliffs that could contribute easily suspended sediment as they are eroded. 5

Figure 2.11: Mabou predicted tide and turbidity measured by the AGRG buoy, July 12 – 18. Peaks in turbidity line up with high tides. 5

Figure 2.12: Scatter plots depicting exponential decay of the depth normalized intensity points created from the drawn lines for (a) Pugwash-River Philip, (b) Merigomish, and (c) Mabou. 8

Figure 3.1: Topographic lidar validation for (a) Pugwash-River Philip, (b) Merigomish, and (c) Mabou. 11

Figure 3.2: Bathymetric lidar validation for (a) Pugwash-River Philip, (b) Merigomish, and (c) Mabou. 12

Figure 3.3: Digital Elevation Model for Pugwash-River Philip for entire study area, scaled to show bathymetry relief, and with insets showing smaller features. Insets are matched to the larger figure by border colour. 14

Figure 3.4: PWRP CSR for entire study area, with insets showing smaller features. Insets are matched to the larger figure by border colour. 14

Figure 3.5: PWRP orthophoto mosaic for entire study area with insets showing smaller features. Insets are matched to the larger figure by border colour. 15

Figure 3.6: Comparison between the intensity model and the depth normalized intensity model for PWRP. The depth normalized intensity is draped over the CSR to add context. The insets show smaller features for both models for comparison purposes. The insets are matched to the larger figure on the left and right by border colour. 15

Figure 3.7: Examples of the 5 cm resolution RCD30 orthophotos at a small scale. (a) The AGRG boat with large GPS pole obtaining ground truth measurements at PWRP; (b) aquaculture infrastructure at Merigomish; and (c) cattle grazing less than 100 m from the shoreline in Mabou. 16

Figure 3.8: Digital Elevation Model for Merigomish, scaled to show bathymetry relief, for entire study area (rotated 54° to the north), and with insets showing smaller features. Insets are matched to the larger figure by border colour. 17

Figure 3.9: Merigomish CSR for entire study area (rotated 54° to the north), with insets showing smaller features. Insets are matched to the larger figure by border colour. 18

Figure 3.10: Merigomish orthophoto mosaic for entire study area (rotated 54° to the north), with insets showing smaller features. Insets are matched to the larger figure by border colour. 19

Figure 3.11: Comparison between the intensity model and the depth normalized intensity model for Merigomish (rotated 54°). The depth normalized intensity is draped over the CSR to add context. The insets show smaller features for both models for comparison purposes. The insets are matched to the larger figure on the left and right by border colour. 20

Figure 3.12: Digital Elevation Model for Mabou, scaled to show bathymetry relief, for entire study area (rotated 9° to the north), and with insets showing smaller features. Insets are matched to the larger figure by border colour. 21

Figure 3.13: Mabou CSR for entire study area (rotated 9° to the north), with insets showing smaller features. Insets are matched to the larger figure by border colour..... 22

Figure 3.14: Mabou orthophoto mosaic for entire study area (rotated 9° to the north), with insets showing smaller features. Insets are matched to the larger figure by border colour..... 23

Figure 3.15: Comparison between the intensity model and the depth normalized intensity model for Mabou. The depth normalized intensity is draped over the CSR to add context. The insets show smaller features for both models for comparison purposes. The insets are matched to the larger figure on the left and right by border colour. 24

Figure 3.16: Relative depth distribution (relative number of observations: number of observations in bin / total number of observations) separated into 0.20 m depth bins..... 25

Figure 3.17: Pugwash River underwater photo ground truth. Background image is RCD30 orthophoto RGB mosaic. 27

Figure 3.18: Mouth of River Philip underwater photo ground truth. Background image is RCD30 orthophoto RGB mosaic. 27

Figure 3.19: River Philip underwater photo ground truth. Background image is RCD30 orthophoto RGB mosaic. 28

Figure 3.20: Merigomish underwater photo ground truth. Background image is RCD30 orthophoto RGB mosaic. 29

Figure 3.21: Merigomish underwater photo ground truth. Background image is RCD30 orthophoto RGB mosaic. 29

Figure 3.22: Merigomish underwater photo ground truth. Background image is RCD30 orthophoto RGB mosaic. 30

Figure 3.23: Mabou underwater photo ground truth. Background image is RCD30 orthophoto RGB mosaic..... 31

Figure 3.24: Mabou underwater photo ground truth. Background image is RCD30 orthophoto RGB mosaic..... 31

Figure 3.25: Mabou underwater photo ground truth. Background image is RCD30 orthophoto RGB mosaic..... 32

Figure 3.26: Mabou underwater photo ground truth. Background image is RCD30 orthophoto RGB mosaic..... 32

Figure 3.27: Correlation between eelgrass presence and AGRG ground truth results in PWRP..... 33

Figure 3.28: Correlation between eelgrass presence and AGRG ground truth results in northeast Merigomish Harbour. 34

Figure 3.29: Correlation between eelgrass presence and DFO Biosonics results in northeast Merigomish Harbour. 34

Figure 3.30: Correlation between eelgrass presence and DFO Biosonics results in southwest Merigomish Harbour. 35

Figure 3.31: Correlation between eelgrass presence and AGRG ground truth results in Western Mabou Harbour..... 35

Figure 3.32: Correlation between eelgrass presence and AGRG ground truth results in Eastern Mabou Harbour..... 36

Figure 3.33: Correlation between eelgrass presence and DFO Biosonics results in Western Mabou Harbour. 36

Figure 3.34: Correlation between eelgrass presence and DFO Biosonics results in Eastern Mabou Harbour..... 37

Figure 3.35: Seabed Cover Classification for PWRP showing the entire study area (top) and cropped to an area near the mouth of River Philip (lower panels). 38

Figure 4.1: Sources of model topographic and bathymetric data. 40

Figure 4.2: Mike 21 hydrodynamic model domain extents for PWRP showing boundaries, and Domain 3 grid draped over a 5x hillshade. 41

Figure 4.3: PWRP Domain 1: 9 m model grid draped over a 5x hillshade. 41

Figure 4.4: Mike 21 hydrodynamic model domain extents for Merigomish showing boundaries, and Domain 5 grid draped over a 5x hillshade. 42

Figure 4.5: Merigomish Domain 1: 9 m model grid draped over a 5x hillshade. The topographic lidar is draped over the modelled topography, which was clipped more closely to the coast. 42

Figure 4.6: Mike 21 hydrodynamic model domain extents for Mabou showing boundaries, and Domain 3 grid draped over a 5x hillshade. 43

Figure 4.7: Merigomish Domain 1: 9 m model grid draped over a 5x hillshade. The topographic lidar is draped over the modelled topography, which was clipped more closely to the coast. 43

Figure 4.8: Tidal elevations predicted for the duration of the PWRP model simulation across the boundaries. 44

Figure 4.9: Tidal elevations predicted for the duration of the Merigomish model simulation across the boundaries. 44

Figure 4.10: Tidal elevations predicted for the duration of the Mabou model simulation across the boundaries. 45

Figure 4.11: PWRP modelled and observed surface elevation and currents. Panels, from top to bottom: surface elevation; east-west current; north-south current; current speed; current direction..... 48

Figure 4.12: Comparison of PWRP depth-averaged currents to currents observed by the ADCP at all depths. 48

Figure 4.13: PWRP model results for (top) domain 1, and (bottom) cropped to an area near the ADCP during maximum flood tide on Sept. 6 at 3:00. The contour map is water depth and the vectors represent current speed and direction..... 49

Figure 4.14: PWRP model results for (top) domain 1, and (bottom) cropped to an area near the ADCP during maximum ebb tide on Sept. 5 at 20:00. The contour map is water depth and the vectors represent current speed and direction..... 50

Figure 4.15: Current vectors at (left) flood tide and (right) ebb tide draped over a contour plot of current speed. 51

Figure 4.16: Merigomish instrumentation by DFO: one ADCP and three Hobo water level sensors; also displayed is the mean modelled depth..... 51

Figure 4.17: Merigomish modelled and observed surface elevations..... 53

Figure 4.18: Merigomish modelled and observed ADCP currents. Panels, from top to bottom: east-west current; north-south current; current speed; current direction. 54

Figure 4.19: Comparison of Merigomish depth-averaged currents to currents observed by the ADCP at all depths..... 54

Figure 4.20: Merigomish model results for (top) Domain 1, and (bottom) cropped to an area near the ADCP and water level sensors during maximum ebb tide on Sept. 18 at 18:00. The contour map is water depth and the vectors represent current speed and direction..... 55

Figure 4.21: Merigomish model results for (top) Domain 1, and (bottom) cropped to an area near the ADCP and water level sensors during maximum flood tide on Sept. 19 at 00:00. The contour map is water depth and the vectors represent current speed and direction..... 56

Figure 4.22: Current vectors at (top) ebb tide and (bottom) flood tide draped over EW current speed (U velocity). 57

Figure 4.23: Mabou modelled and observed surface elevation and currents..... 59

Figure 4.24: Comparison of Mabou depth-averaged currents to currents observed by the ADCP at all depths..... 60

Figure 4.25: Mabou model results for (top) Domain 1, and (bottom) cropped to an area near the ADCP during maximum flood tide on Oct. 2 at 6:00. The contour map is water depth and the vectors represent current speed and direction. 61

Figure 4.26: Mabou model results for (top) Domain 1, and (bottom) cropped to an area near the ADCP during maximum ebb tide on Oct. 2 at 00:00. The contour map is water depth and the vectors represent current speed and direction. 62

Figure 8.1: Predicted tidal elevation for Pugwash and observed tidal elevation as recorded by the ADCP. 65

Figure 8.2: Depth averaged current speeds at Pugwash on the left y-axis with NS: solid blue line, EW: dashed blue line; ADCP depth on the right y-axis with solid orange line. 66

Figure 8.3: Contour plots of EW (top panel) and NS (lower) currents at Pugwash, with observed depth plotted as a black line. Current speed is represented by colour. The y-axis represents range away from the ADCP, the x-axis represents time..... 66

Figure 8.4: Predicted tidal elevation for Merigomish, observed tidal elevation as recorded by the ADCP and the three Hobo water level sensors. 67

Figure 8.5: Depth averaged current speeds at Merigomish on the left y-axis with NS: solid blue line, EW: dashed blue line; ADCP depth on the right y-axis with solid orange line. 67

Figure 8.6: Contour plots of EW (top panel) and NS (lower) currents at Merigomish, with depth observed by MGH1 plotted as a black line. Current speed is represented by colour. The y-axis represents range away from the ADCP, the x-axis represents time..... 68

Figure 8.7: Predicted tidal elevation for Mabou and observed tidal elevation as recorded by the ADCP. 68

Figure 8.8: Depth averaged current speeds at Mabou on the left y-axis with NS: solid blue line, EW: dashed blue line; ADCP depth on the right y-axis with solid orange line. 69

Figure 8.9: Contour plots of EW (top panel) and NS (lower) currents at Mabou, with observed depth plotted as a black line. Current speed is represented by colour. The y-axis represents range away from the ADCP, the x-axis represents time..... 69

Figure 8.10: Locations and IDs of Pugwash River CTD profiles. 70

Figure 8.11: Results of CTD depth profiles for salinity (in PSU), temperature (in °C), turbidity (in NTU), and chlorophyll (unitless). Each y-axis represents depth and each x-axis represents the parameter being measured. 71

Figure 8.12: Depth averaged salinity (left); and temperature (right) turbidity at each CTD profile location. 71

Figure 8.13: Depth averaged turbidity (left); and chlorophyll (right) turbidity at each CTD profile location..... 72

Figure 8.14: Locations and IDs of Mabou CTD profiles. 72

Figure 8.15: Results of Mabou CTD depth profiles for salinity (in PSU), temperature (in °C), turbidity (in NTU), and chlorophyll (unitless). Each y-axis represents depth and each x-axis represents the parameter being measured. The top panel shows data from July 13 and the lower panel shows data from July 21. 73

Figure 8.16: Depth averaged salinity values at each CTD profile location..... 73

Figure 8.17: Depth averaged temperature values at each CTD profile location. 74

Figure 8.18: Depth averaged turbidity values at each CTD profile location. 74

Figure 8.19: Depth averaged chlorophyll values at each CTD profile location. 74

List of Tables

Table 2.1: 2016 NSFA lidar survey dates, durations, areas, and flight lines. 4

Table 2.2: Ground truth data summary. * Indicates that the ground truth survey was occurring simultaneously with the lidar survey. GPS Column: Two Leica GPS systems were used the GS14 and the 530; a Garmin handheld unit was also employed. Depth Column: P=GPS antenna threaded onto the large pole for direct bottom elevation measurement; M>manual depth measurement using lead ball or weighted Secchi disk; ES=Single beam commercial grade Humminbird Echo Sounder; BioSon.=BioSonics brand echo sounder. Underwater Photos: P=GoPro camera secured to pole for underwater still photos; Q₅₀=0.25 m² quadrat with downward-looking GoPro camera. ADCP- Sentinel, Workhorse (WH) or RiverRay (RR). 1

Table 2.3. Lidar point classification Codes and descriptions. Note that ‘overlap’ is determined for points which are within a desired footprint of points from a separate flight line; the latter of which having less absolute range to the laser sensor..... 7

Table 3.1: Area of lidar DEM per depth contour, for each study area. 26

Table 3.2: Percentage agreement of eelgrass with AGRG drops and Biosonics and for each area, and the proportion of the lidar study area classified as eelgrass. 33

Table 4.1: HD model bathymetric data sources, resolution, domain and number of observations. NSDNR: Nova Scotia Department of Natural Resources. 39

Table 4.2: Model Parameters for each study area..... 46

1 Introduction

1.1 Project Background

Three study areas in Nova Scotia were surveyed in July 2016 with topographic-bathymetric lidar for the Nova Scotia Department of Fisheries and Aquaculture (NSFA). The bays are shallow, protected inlets vegetated with eelgrass that host aquaculture, recreational users, and seasonal residents. The motivation for this study was to use the lidar products (high resolution bathymetry, laser intensity, aerial photographs, and ground-truth data) to aid in NSFA aquaculture site selection. The data products were used to develop submerged aquatic vegetation maps for each area as secondary lidar products, and hydrodynamic models were developed to aid in understanding of water movement within the estuaries. The information on water movement, bottom type, and water depth provided by this project will allow NSFA to characterize the estuaries and make informed decisions on coastal development and aquaculture site selection.

This report highlights the results of the lidar survey and the derived data products, including the digital elevation models (DEM), digital surface models (DSM), and lidar intensity models, all derived from the lidar point cloud. Additionally, this report presents the high-resolution RCD30 60 megapixel (MPIX) imagery, processed using the aircraft trajectory and direct georeferencing. The results of the hydrodynamic models, which simulate current flow and water level variations within each study area, are presented. Eelgrass maps illustrate the presence of eelgrass in the study areas. Ground truth maps highlight the results of the ground truth survey such as bottom type, seagrass percentage and water clarity. For the intertidal and subtidal areas, this level of information has never been surveyed before with such sophisticated equipment and provides a rich series of GIS-ready data layers for capturing the baseline information for this study. The information on water movement, bottom type, and water depth provided by this project will help NSFA to characterize the estuaries and make informed decisions on coastal development and aquaculture site selection.

1.2 Study Area

The three study areas are located on the Nova Scotia shoreline of the Northumberland Strait (Figure 1.1). The most westerly study area is Pugwash-River Philip (PWRP), a survey that includes River Philip, the Pugwash River, the town of Pugwash and the harbour where the two rivers meet in the bay and enter the Strait. Merigomish Harbour is located in Pictou County and the study area encompasses the back harbour and a small strip of the exposed Strait. Mabou Harbour in western Cape Breton has a very narrow mouth to an inlet that has two major rivers draining into it.

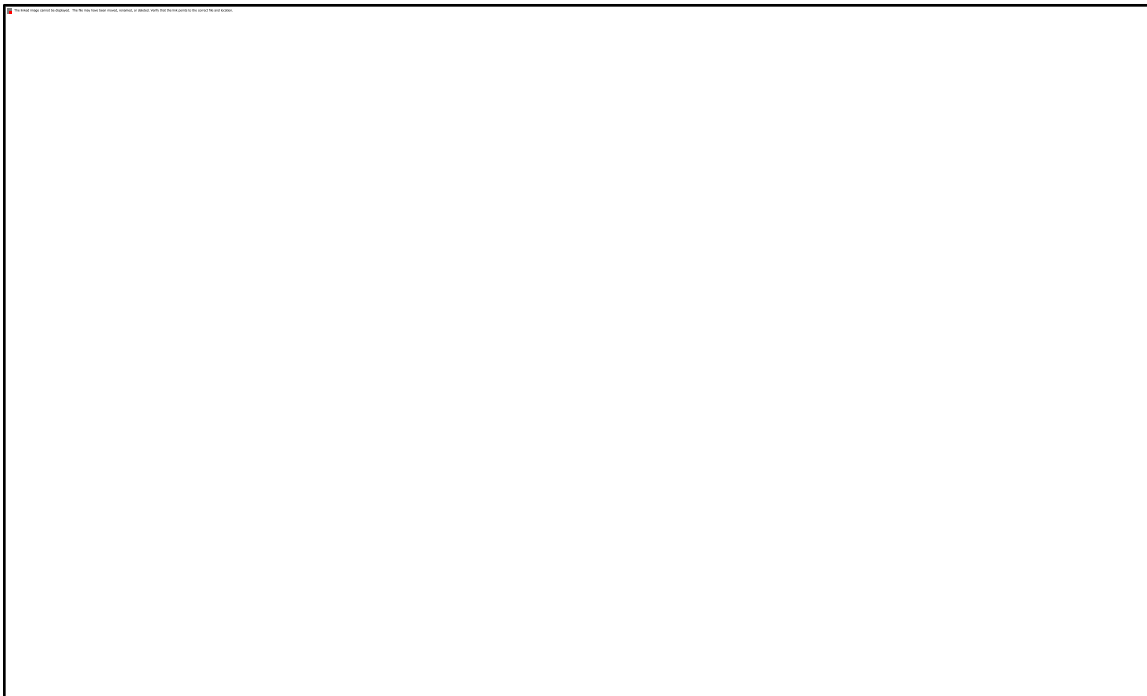


Figure 1.1: The topographic-bathymetric lidar study areas in the Southern Gulf of St. Lawrence surveyed in July 2016 showing NS High Precision Network (HPN) stations (orange squares) and Environment Canada (EC) Weather Stations (green triangles).

2 Methods

2.1 Sensor Specifications

The lidar sensor used in this study is a Chiroptera II integrated topographic-bathymetric lidar sensor equipped with a 60-megapixel multispectral camera. The system incorporates a 1064 nm near-infrared laser for ground returns and sea surface and a green 515 nm laser for bathymetric returns (Figure 2.1, Figure 2.2d). The lasers scan in an elliptical pattern, which enables coverage from many different angles on vertical faces, causes less shadow effects in the data, and is less sensitive to wave interaction. The bathymetric laser is limited by depth and clarity, and has a depth penetration rating of roughly 1.5 x the Secchi depth (a measure of turbidity or water clarity using a black and white disk). The Leica RCD30 camera (Figure 2.2d) collects co-aligned RGB+NIR motion compensated photographs, which can be mosaicked into a single image in post-processing, or analyzed frame by frame for maximum information extraction.

The calibration of the lidar sensor and camera have been documented in an external report which will be included as part of the deliverables for this project.

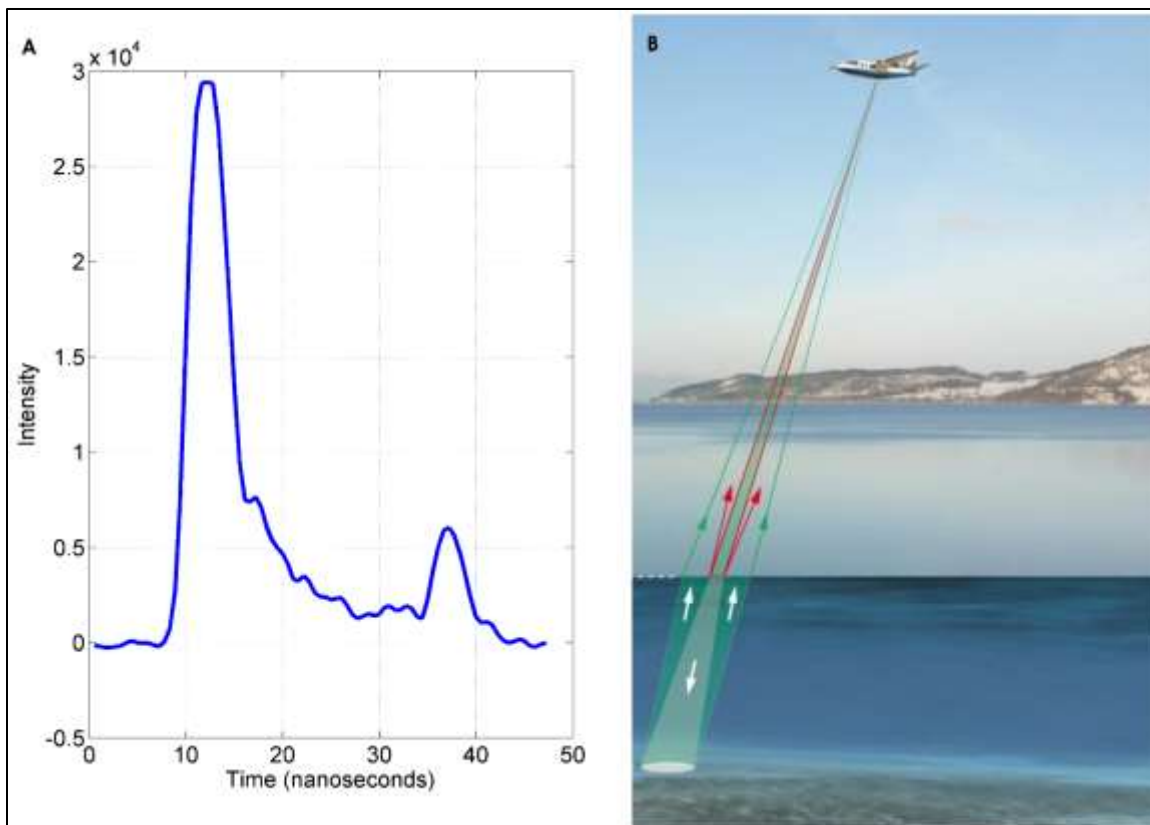


Figure 2.1: (A) Example of the Chiroptera II green laser waveform showing the large return from the sea surface and smaller return from the seabed. (B) Schematic of the Chiroptera II green and NIR lasers interaction with the sea surface and seabed (adapted from Leica Geosystems).

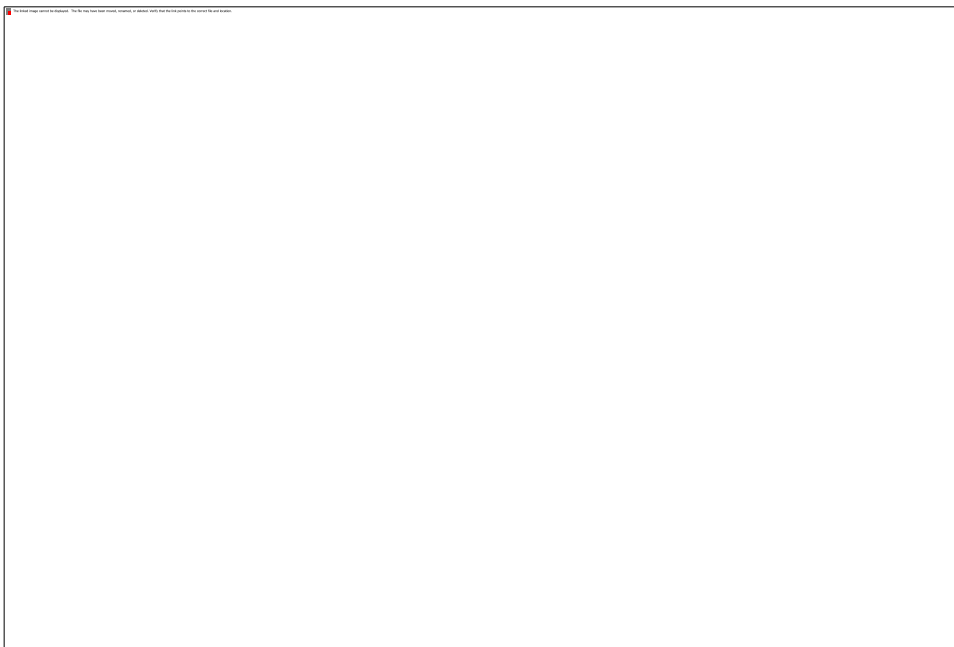


Figure 2.2: (a) Aircraft used for 2016 lidar survey; (b) display seen by lidar operator in-flight; (c) main body of sensor (right) and the data rack(left); (d) large red circles are the lasers; the RCD30 lens (right) and low resolution camera quality control(left).

2.2 Lidar Survey Details

The lidar surveys were conducted in July 2016 (Table 2.1). The surveys were planned using Mission Pro software and flown at an altitude of 400 m above ground at a flying speed of 62 m/s. The planned flight lines for each study area are shown in Figure 2.3. The aircraft required ground-based high precision GPS data to be collected during the lidar survey in order to provide accurate positional data for the aircraft trajectory. Our Leica GS14 RTK GPS system was used to set up a base station set to log observations at 1 second intervals over a Nova Scotia High Precision Network (HPN) (Figure 1.1).

The PWRP survey began on July 7 and was approximately two thirds completed when light rain forced the survey to be aborted and postponed until July 11, when it was completed in good weather conditions. The Merigomish survey was started on July 12 but the survey was postponed after one flight line had been completed because the aircraft had reached its maximum daily flight time; the survey was completed on July 13. The Merigomish study area was the largest (87 km²) and took 5.5 hours to complete. The Mabou survey was also attempted on July 12 and although the weather was suitable for lidar the water clarity conditions were poor and the survey was aborted with no good data collected. A field team was deployed on July 13 to deploy a turbidity buoy in Mabou on July 13 in order to monitor water clarity remotely (this will be discussed further in Section 2.3 and 2.4). Suitable weather and water clarity conditions were present on July 19 at Mabou and the survey was completed. At 25 km² and 21 flight lines Mabou was the smallest of the areas surveyed for this project.

Study Area	Abbreviated Name	Survey Date	Survey Time (UTC)	Survey Duration (hrs)	Number of Flight Lines	Area (km ²)
Pugwash/River Philip	PWRP	July 7	1245 - 1630, 1730 -1845	6	45	57
		July 11	2000 - 2100			
Merigomish	MERI	July 12	1930 - 2030	5.5	31	87
		July 13	1130 - 1400, 1630 - 1830			
Mabou	MAB	July 12 Aborted, no good data	1745 -1815	1	21	25
		July 19	1715 - 1945			

Table 2.1: 2016 NSFA lidar survey dates, durations, areas, and flight lines.

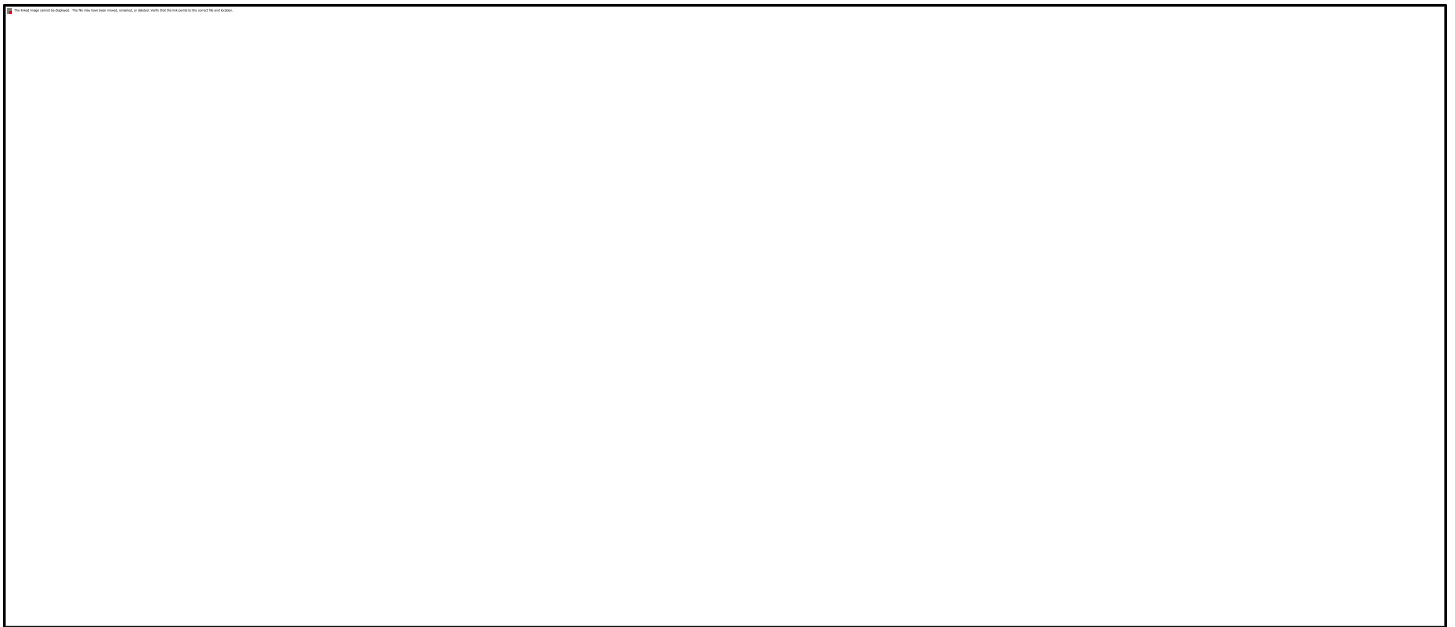


Figure 2.3: Flight lines for the 2016 study areas (A) Pugwash/River Philip, (B) Merigomish, and (C) Mabou.

2.3 Ground Truth Data Collection

Ground truth data collection is an important aspect of topo-bathymetric lidar data collection. In 2016 we conducted our traditional “time-of-flight” ground truth data including hard surface validation and depth measurements to validate the lidar, Secchi depth measurements for information on water clarity, and underwater photographs to obtain information on bottom type and vegetation (Table 2.2, Figure 2.5 - Figure 2.7). The seabed elevation was measured directly using a large pole onto which the RTK GPS was threaded, in addition to manual measurements using a lead ball on a graduated rope, and a commercial-grade single beam echo sounder. By threading the RTK GPS antenna on the pole and measuring the elevation of the seabed directly we eliminated errors introduced into depth measurements obtained from a boat such as those caused by wave action, tidal variation, and angle of rope for lead ball drop measurements (Figure 2.6a). Table 2.2 summarizes the ground truth measurements undertaken for the three NSFA study areas in 2016, and Figure 2.4 shows a map of the distribution of ground truth measurements.

Fieldwork for this project extended beyond the time of flight ground truth measurements to include current meters, depth profiling instruments, and turbidity buoys. A Teledyne RDI Sentinel V20 1000 kHz Acoustic Doppler Current Profiler (ADCP) was deployed at PWRP and Mabou to measure current speed and direction for minimum 35 days (Table 2.2, Figure 2.5, Figure 2.4). A 600kHz RiverRay ADCP was used in PWRP and Mabou to measure currents from a moving vessel; this ADCP was used to measure flow across different sections of River Phillip and at the narrow mouth of Mabou Harbour (Figure 2.5b, Figure 2.7b, Figure 2.4). At Merigomish, DFO partners deployed an RDI 1229 kHz Workhorse ADCP and three Hob water level sensors. A Seabird 25plus Conductivity Temperature Depth (CTD) sensor was used during the lidar survey on July 7 at PWRP and in Mabou on July 13 and 21 as another depth validation method, but also to measure changes in salinity and temperature at different locations within the study area, and through the water column (Figure 2.5f, Figure

2.4). A 1 m x 1 m steel cube was deployed at PWRP on July 7 to assess the lidar’s ability to detect such a shape (Figure 2.5d). A Nexsens Technology CB-50 Turbidity buoy equipped with a cell modem was deployed at Mabou on July 13 in order to remotely monitor water clarity (Figure 2.7c). The buoy monitored turbidity at 0.75 m below the water surface every 15 minutes and uploaded the data to a web server three times a day.

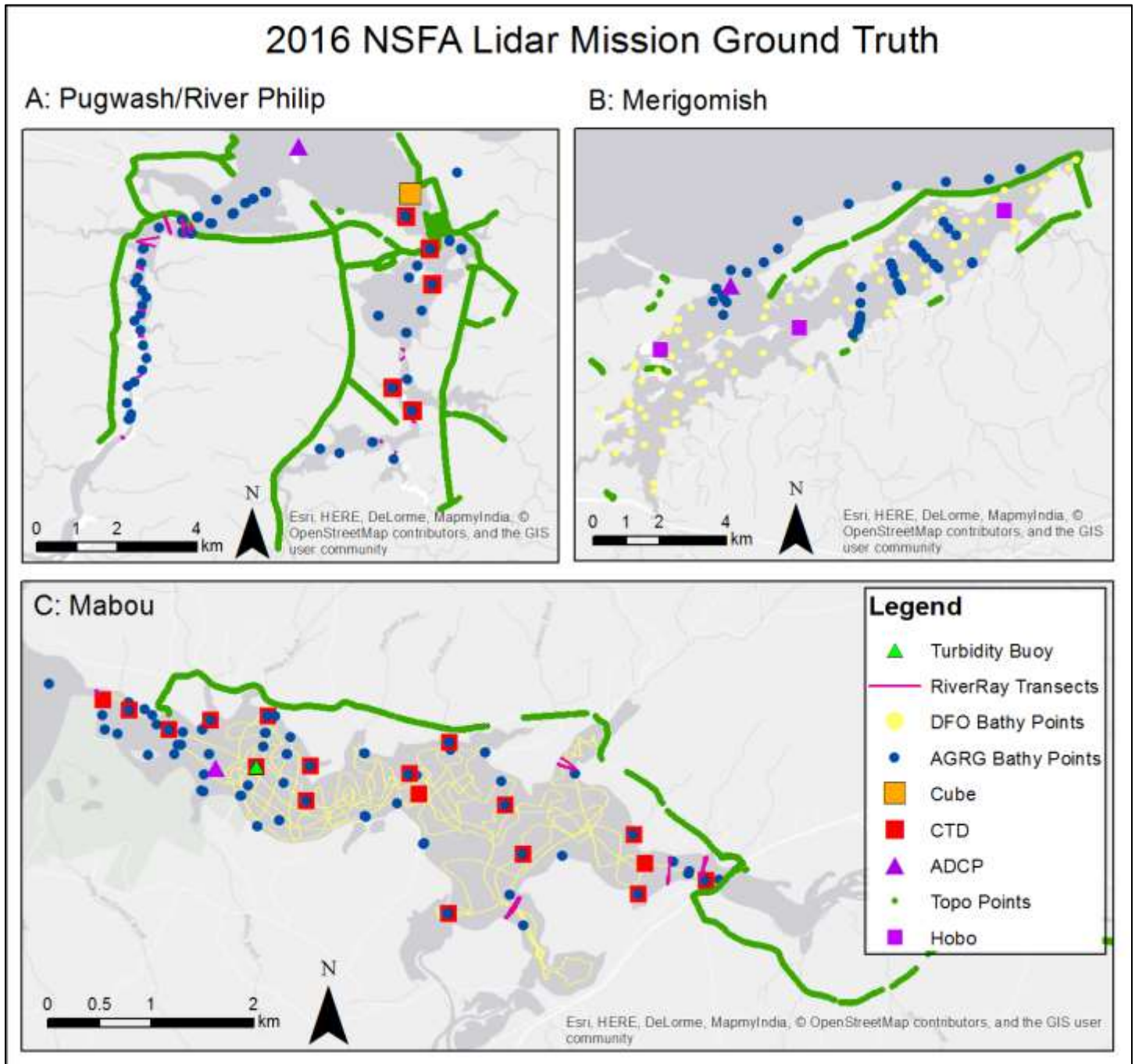


Figure 2.4: Location of hard surface GPS validation points, AGRG and DFO boat-based ground truth waypoints at (A) Pugwash/River Philip, (B) Merigomish and (C) Mabou. The location of the ADCP deployed in Merigomish by DFO is unknown at this time, no CTD measurements were obtained in Merigomish, and a cube was deployed in Pugwash only.

Location	Date	Base station	GPS System	Secchi	Depth	ADCP	Underwater Photos	Hard Surface GPS	CTD	Turbidity Buoy	Cube	Partner Participation
PWRP	July 7*	13698	GS14, 1200	Y	P, M, ES	RR	P, Q ₅₀	Y	Y	-	Dep. & Rec.	NSFA
	July 14	13698	GS14, 1200	-	ES	RR	P, Q ₅₀	-	-	-	-	NSFA
	Aug 5		GS14	-	-	Sentinel Deployed	-	-	-	-	-	
	Sept 9	-	-	-	-	Sentinel Recovered	-	-	-	-	-	
MERI	July 13*	21949	GS14, Garmin	Y	M	-	P, Q ₅₀	Y	-	-	-	NSFA
	July 18				M							DFO ONLY
	Aug 10				BioSon.							
	Sept 7					WH Deployed						
	Nov 22					WH Recovered						
MAB	July 13	-	Garmin	Y	ES	-	-	-	Y	Deployed	-	-
	July 21	214131	GS14, 1200, Garmin	Y	P, M	RR	P, Q ₅₀	Y	Y	Recovered	-	NSFA
	Aug 30				BioSon.							DFO ONLY
	Sept 15	-		-	-	Sentinel Deployed	-	-	-	-		
	Oct 27	-	-	-	-	Sentinel Recovered	-	-	-	-		

Table 2.2: Ground truth data summary. * Indicates that the ground truth survey was occurring simultaneously with the lidar survey. GPS Column: Two Leica GPS systems were used the GS14 and the 530; a Garmin handheld unit was also employed. Depth Column: P=GPS antenna threaded onto the large pole for direct bottom elevation measurement; M=manual depth measurement using lead ball or weighted Secchi disk; ES=Single beam commercial grade Humminbird Echo Sounder; BioSon.=BioSonics brand echo sounder. Underwater Photos: P=GoPro camera secured to pole for underwater still photos; Q₅₀=0.25 m² quadrat with downward-looking GoPro camera. ADCP- Sentinel, Workhorse (WH) or RiverRay (RR).



Figure 2.5: Ground truth data collection at Pugwash and River Phillip. (a) Base station setup, (b) RiverRay ADCP being towed by AGRG boat, (c) ADCP deployment (d) cube, (e) AGRG and NSFA collaborating in Pugwash, (f) CTD.

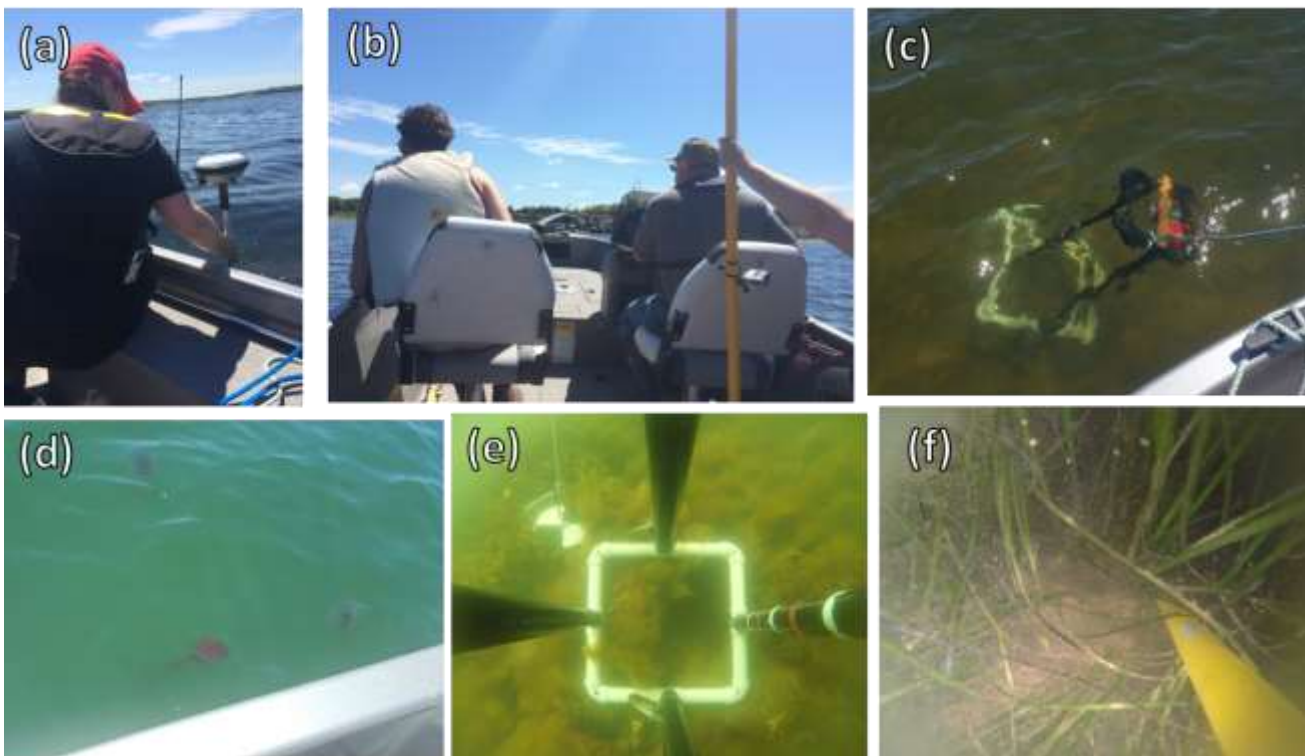


Figure 2.6: Ground truth data collection in Merigomish. (a) seabed elevation measurement with GPS antenna threaded onto pole, (b) AGRG and NSFA collaborating in Merigomish, (c) 0.25 m² quadrat being deployed, (d, e) clear water in Merigomish during the aerial and ground truth survey, (f) healthy eelgrass.

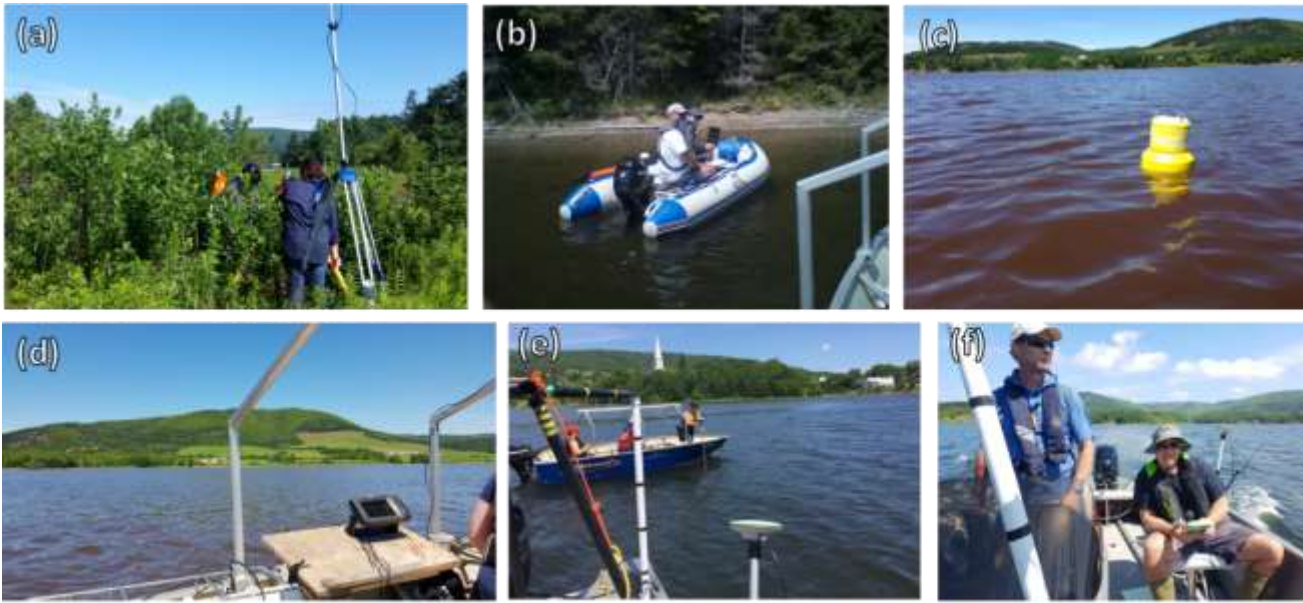


Figure 2.7: Ground truth data collection in Mabou. (a) Base station setup, (b) RiverRay ADCP being towed from inflatable boat, (c) turbidity buoy on deployment data (July 13), (d) Humminbird echosounder for depth measurement, (e) GPS gear on both NSFA and AGRG boats in Mabou, (f) NSFA and AGRG collaboration in Mabou.

2.4 Time of Flight Conditions: Weather, Tide and Turbidity

Meteorological conditions during and prior to topo-bathy lidar data collection are an important factor in successful data collection. As the lidar sensor is limited by water clarity, windy weather has the potential to stir up any fine sediment in the water and prevent good laser penetration. Rainy weather is not suitable for lidar collection, and the glare of the sun must also be factored in for the collection of aerial photography. Before each lidar survey we primarily monitored weather forecasts using four tools: the Environment Canada (EC) public forecast (<http://weather.gc.ca/>) for Caribou and Port Hawkesbury (Figure 1.1); EC’s Marine Forecast (https://weather.gc.ca/marine/index_e.html); SpotWx (www.spotwx.com), which allows the user to enter a precise location and choose from several forecasting models of varying model resolution and forecast length; and a customized EC forecast for the lidar study areas provided to AGRG every eight hours. Each of these tools had benefits and shortcomings, and it was through monitoring all four that a successful lidar mission was achieved. For example, the customized EC forecast was the only tool that provided a fog prediction, on an hourly basis. However, the SpotWx graphical interface proved superior for wind monitoring. Only the EC public forecast alerted us to Weather Warnings that were broadcast in real-time, such as thunderstorms, and the marine forecast provided the only information for offshore conditions. The tide is another important consideration in a bathymetric lidar survey, and ideally each survey would be flown as close to low tide as possible to extend the area of laser penetration.

Although the summer of 2016 was particularly hot and dry, the lidar mission was not without its metrological challenges. As mentioned in Section 2.2 the PWRP survey was completed during two separate flights after the first flight was aborted due to light rain, which can be seen starting late in the day on July 7 (Figure 2.8). Wind was between 10 and 20 km/hr blowing from the North during the survey and the tide began and low tide but was near high tide by the end of the survey. Wind in the days prior to the survey was low, staying mostly below 20 km/hr after July 3; it is not expected that wind at PWRP had an impact on water clarity on July 7. The survey was completed on July 11 in the sheltered River Phillip arm of the study area during a high tide. Although wind is reported to have been ~25 km/hr at Caribou there were no issues with wind during the flight and lidar penetration was good.

The Merigomish survey on July 12 was flown under low wind conditions (~5 km/hr), clear skies, and a high tide (Figure 2.8). The survey was restarted on July 13 on a falling tide to maximize the amount of survey time near low tide. Wind was between 5 and 15 km/hr during the survey and no rain was reported.

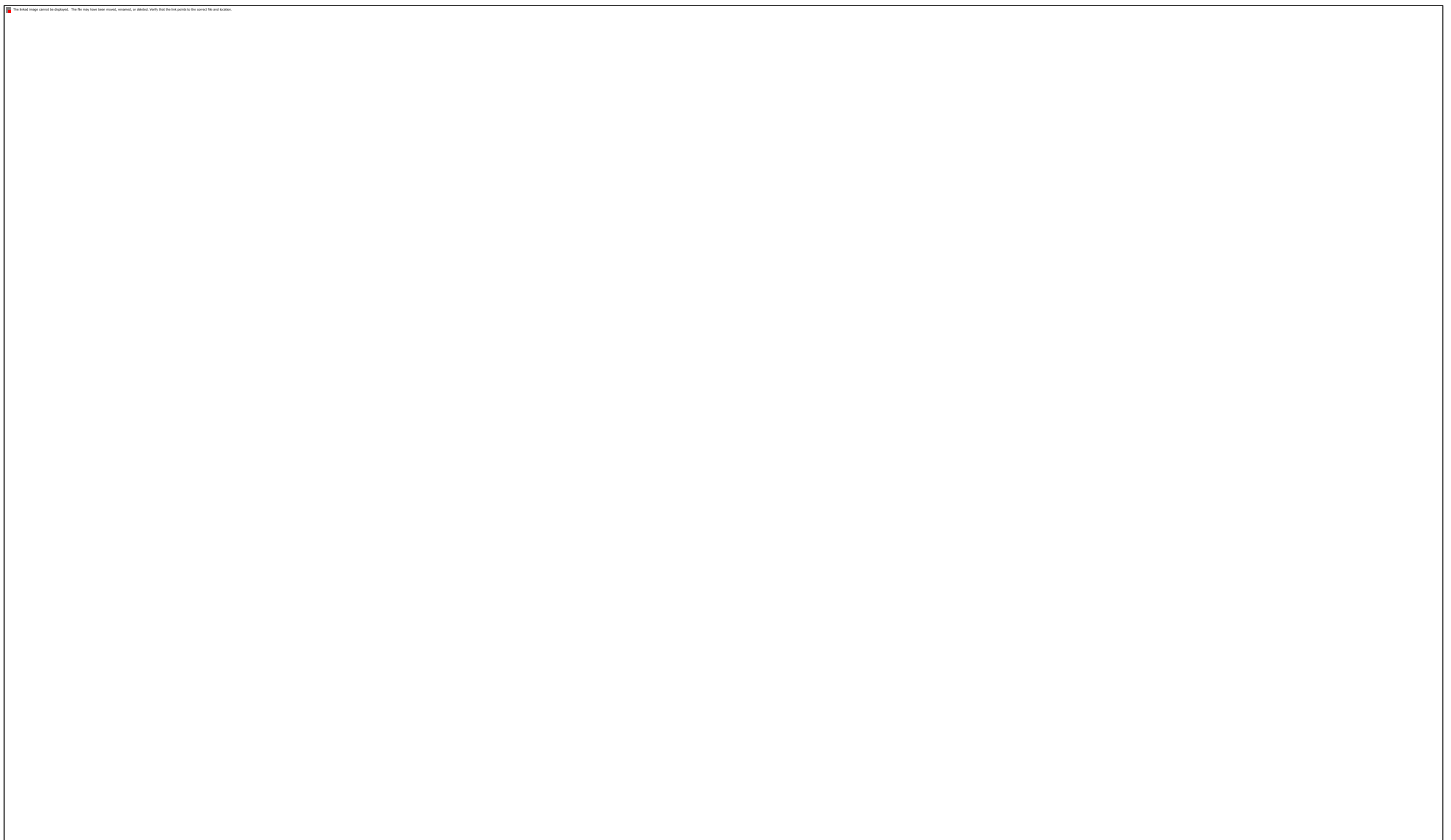


Figure 2.8: Caribou meteorological data (a) wind speed; (b) wind direction; (c) wind vectors indicating speed and direction wind is blowing towards; (d) daily rainfall; (e) predicted tide at River Phillip and Merigomish in Chart Datum. Lidar surveys at PWRP and MERI are highlighted in orange and green, respectively. Time axis is in UTC time zone.

The first survey at Mabou was attempted on July 12 in <20 km/hr northerly wind on a rising tide but was aborted due to poor lidar penetration. The lidar operator reported that the water appeared cloudy and red. There were several small rainfall events during the week prior to that survey, including July 11 where 11.2 mm of rain fell at Cheticamp (there is no

rainfall record at Port Hawkesbury) (Figure 2.9). This rainfall event, combined with 30 km/hr north wind on the same day, could have flushed sediment from the river systems into Mabou Harbour, or stirred up suspended sediments from the sandstone cliffs (Figure 2.10c). A field team was deployed to Mabou July 13 to deploy a turbidity buoy to monitor water clarity conditions at Mabou in real-time (Figure 2.10, Figure 2.11a) and local NSFA contacts were also enlisted to visually assess water clarity. The area was re-surveyed on July 19 when the water was reported to be clear of the red suspended sediment by the local contact, and the turbidity buoy indicated that water clarity had improved (Figure 2.9f). The survey was completed during a low tide with blowing from the north at ~15 km/hr. During ground truth surveys on July 21 turbidity varied from clear near the mouth of the harbour to reduced clarity farther up the inlet (Figure 2.10b). In between lidar surveys there was an event on July 15 where ~14 mm of rain was recorded at Cheticamp and the wind reached 30 km/hr blowing from the south; this event correlates with a small increase in turbidity that quickly decreased, and remained low until the buoy was removed on July 21 following the lidar survey. A correlation between high tide and high turbidity is apparent (Figure 2.11).

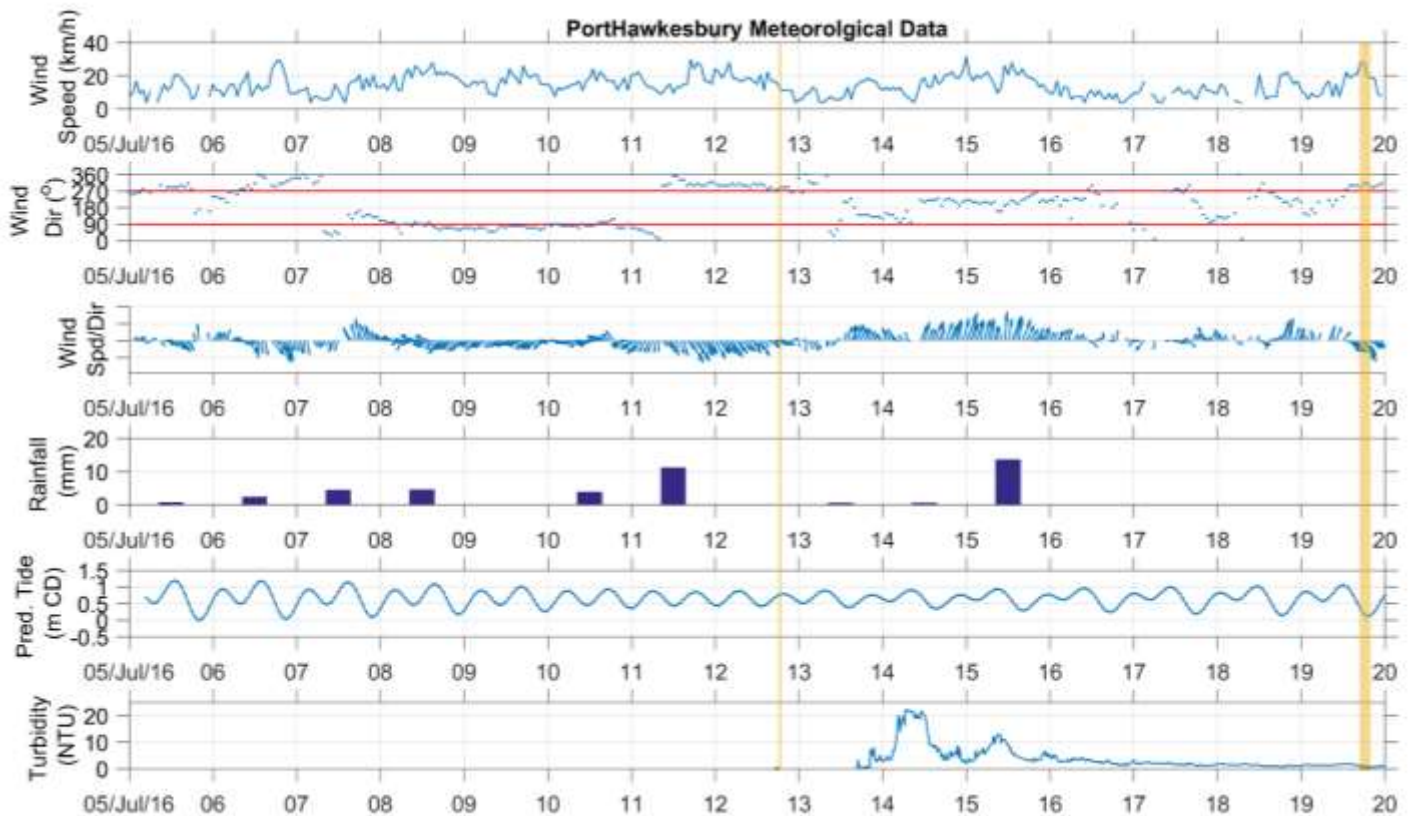


Figure 2.9: (a - c): Wind speed and direction data recorded at Port Hawkesbury; (d) daily rainfall recorded at Cheticamp; (e) predicted tide at Port Hood in Chart Datum; (f) turbidity measured by AGRG buoy. The attempted and completed lidar surveys are highlighted in orange. Time axis is in UTC time zone.

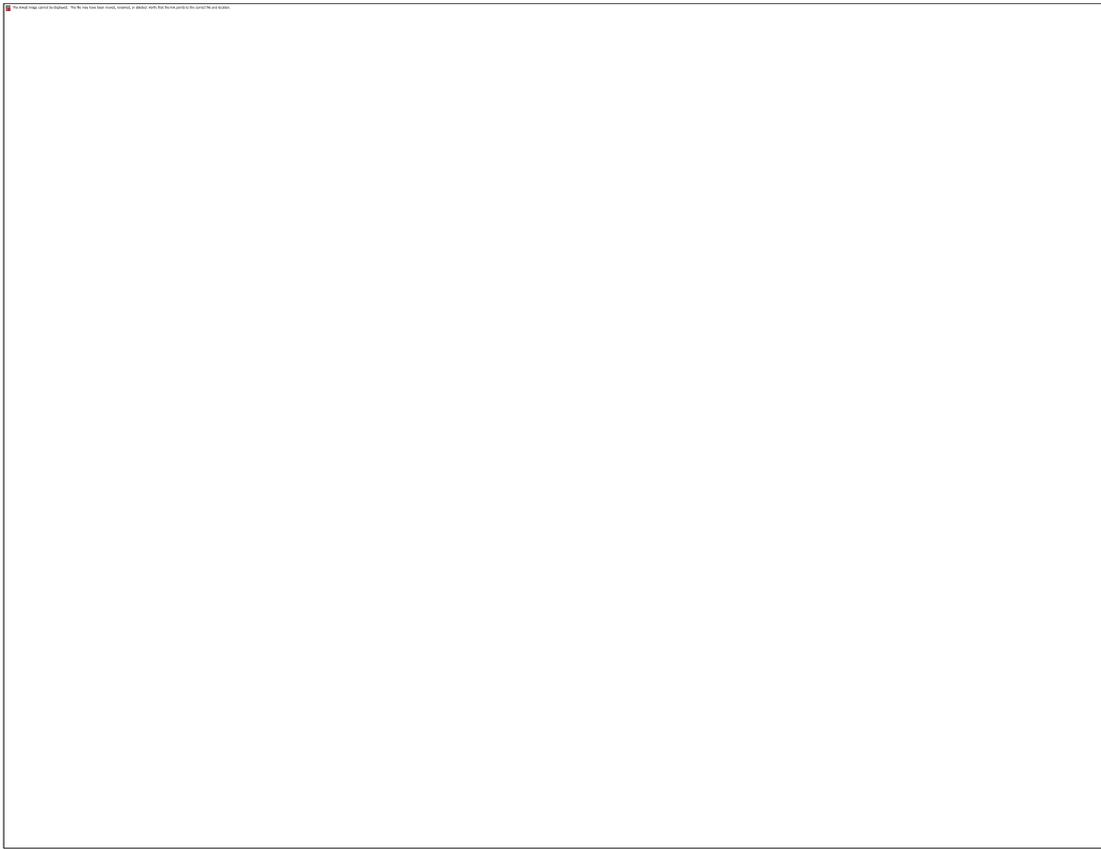


Figure 2.10: (a) High turbidity at Mabou on July 13; (b) varying turbidity during ground truth on July 21; (c) red sandstone cliffs that could contribute easily suspended sediment as they are eroded.

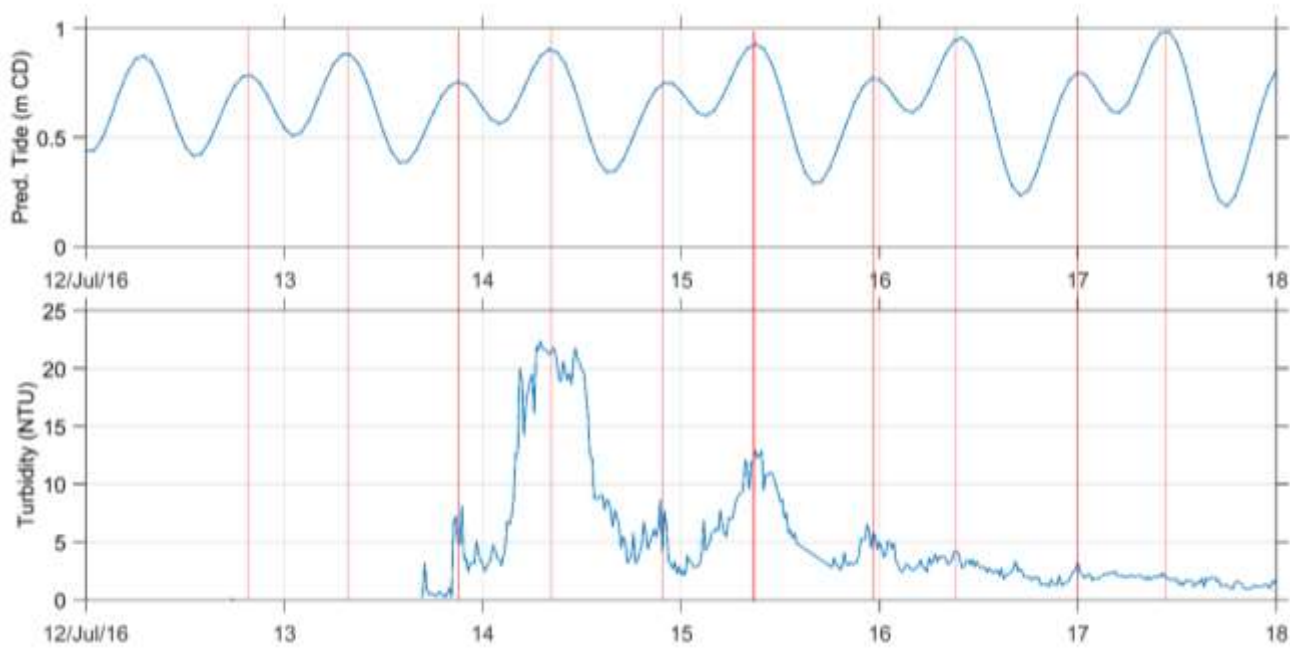


Figure 2.11: Mabou predicted tide and turbidity measured by the AGRG buoy, July 12 – 18. Peaks in turbidity line up with high tides.

2.5 Elevation Data Processing

2.5.1 Lidar processing

2.5.1.1 Point Cloud Processing

Once the GPS trajectory was processed for the aircraft utilizing the GPS base station and aircraft GPS observations were combined with the inertial measurement unit, the navigation data was linked to the laser returns and georeferenced. Lidar Survey Studio (LSS) software accompanies the Chiroptera II sensor and is used to process the lidar waveforms into discrete points. The data can then be inspected to ensure there was sufficient overlap (30%) and no gaps exist in the lidar coverage.

One critical step in the processing of bathymetric lidar is the ability to map the water surface. This is critical for two components of georeferencing the final target or targets that the reflected laser pulse recorded: the refraction of the light when it passes from the medium of air to water and the change in the speed of light from air to water. The LSS software computes the water surface from the lidar returns of both the topo and bathy lasers. In addition to classifying points as land, water surface or bathymetry, the system also computes a water surface that ensures the entire area of water surface is covered regardless of the original lidar point density. As mentioned, part of the processing involves converting the raw waveform lidar return time series into discrete classified points using LSS signal processing; points include ground, water surface, seabed, etc. Waveform processing may include algorithms specifically for classifying the seabed. The points were examined in LSS both in plan view and in cross-section view. The waveforms can be queried for each point so that the location of the waveform peak can be identified and the type of point defined, for example water surface and bathymetry.

The LAS files were read into TerraScan™ with the laser returns grouped by laser type so they could be easily separated, analyzed and further refined. Because of the differences in the lidar footprint between the topo and bathy lasers, the bathy point returns would be used to represent the water surface and bathymetry points and the topo points would be used to represent targets on the land. See Table 2.3 and the attached Data Dictionary report for the classification codes for the delivered LAS 1.2 files. The refined classified LAS files were read into ArcGIS™ and a variety of raster surfaces at a 1 m spatial sampling interval were produced.

Table 2.3. Lidar point classification Codes and descriptions. Note that ‘overlap’ is determined for points which are within a desired footprint of points from a separate flight line; the latter of which having less absolute range to the laser sensor.

Class number	Description
0	Water model
1	Bathymetry (Bathy)
2	Bathy Vegetation
3	N/A
4	Topo laser Ground
5	Topo laser non-ground (vegetation & buildings)
6	Hydro laser Ground
7	Bathy laser non-ground
8	Water
9	Noise
10	Overlap Water Model
11	Overlap Bathy
12	Overlap Bathy Veg
13	N/A
14	Overlap Topo Laser Ground
15	Overlap Topo Laser Veg
16	Overlap Bathy Laser Ground
17	Overlap Bathy Laser Veg
18	Overlap Water
19	Overlap Noise

2.5.1.2 Gridded Surface Models

There are three main data products derived from the lidar point cloud. The first two are based on the elevation and include the Digital Surface Model (DSM) that incorporates valid lidar returns from vegetation, buildings, ground and bathymetry returns, and the Digital Elevation Model (DEM) that incorporates ground returns above and below the water line. The third data product is the intensity of the lidar returns, or the reflectance of the bathy laser. The lidar reflectance, or the amplitude of the returning signal from the bathy laser, is influenced by several factors including water depth, the local angle of incidence with the target, the natural reflectivity of the target material, the transmission power of the laser and the sensitivity of the receiver.

2.5.1.3 Depth Normalization of the Green Laser

The amplitude of the returning signal from the bathy laser provides a means of visualizing the seabed cover, and is influenced by several factors including water depth and clarity, the local angle of incidence with the target, the natural

reflectivity of the target material, and the voltage or gain of the transmitted lidar pulse. The raw amplitude data are difficult to interpret because of variances as a result of signal loss due to the attenuation of the laser pulse through the water column at different scan angles. Gridding the amplitude value from the bathy lidar results in an image with a wide range of values that are not compensated for depth and have significant differences for the same target depending on the local angle of incidence from flight line to flight line. As a result, these data are not usable as is for quantitative analysis and are difficult to interpret for qualitative analysis. A process has been developed to normalize the amplitude data for signal loss in a recent publication (Webster et al., 2016). The process involved sampling the amplitude data from a location with homogeneous seabed cover (e.g., sand or eelgrass) over a range of depths. These data were used to establish a relationship between depth and the logarithm of the amplitude value. The inverse of this relationship was used with the depth map to adjust the amplitude data so that they could be interpreted without the bias of depth. A depth normalized amplitude/intensity image (DNI) was created for each study site using this technique that can be more consistently interpreted for the seabed cover material. Note that this analysis considers only bathymetric lidar values and ignores any topographic elevation points (Figure 2.12).

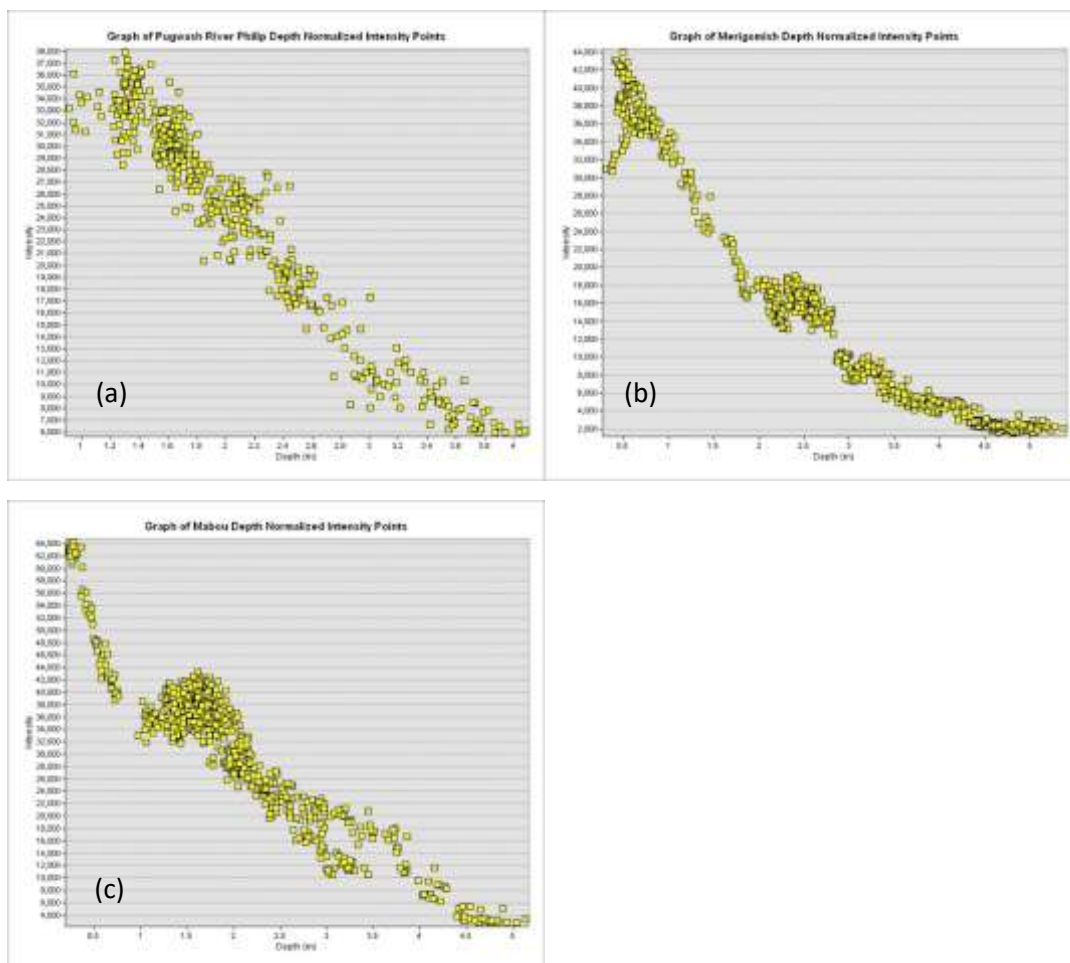


Figure 2.12: Scatter plots depicting exponential decay of the depth normalized intensity points created from the drawn lines for (a) Pugwash-River Philip, (b) Merigomish, and (c) Mabou.

2.5.1.4 *Aerial Photo Processing*

The RCD30 60 MPIX imagery was processed using the aircraft trajectory and direct georeferencing. The low altitude and high resolution of the imagery required that the lidar data be processed first to produce bare-earth digital elevation models (DEMs) that were used in the orthorectification process. The aircraft trajectory, which blends the GPS position and the IMU attitude information into a best estimate of the overall position and orientation of the aircraft during the survey. This trajectory, which is linked to the laser shots and photo events by GPS based time tags, is used to define the Exterior Orientation (EO) for each of the RCD30 aerial photos that were acquired. The EO, which has traditionally been calculated by selecting ground control point (x, y, and z) locations relative to the air photo frame and calculating a bundle adjustment, was calculated using direct georeferencing and exploiting the high precision of the navigation system. The EO file defines the camera position (x, y, z) for every exposure as well as the various rotation angles about the x, y and z axis known as omega, phi and kappa. The EO file along with a DEM was used with the aerial photo to produce a digital orthophoto. After the lidar data were processed and classified into ground points, the lidar-derived DEM (above and below the water line) was used in the orthorectification process in Erdas Imagine software and satisfactory results were produced.

2.5.2 **Ellipsoidal to Orthometric Height Conversion**

The original elevation of any lidar products are referenced to the same elevation model as the GPS with which they were collected. This model is a theoretical Earth surface known as the ellipsoid, and elevations referenced to this surface are in ellipsoidal height (GRS80). To convert them to orthometric height (OHT), which is height relative to the Canadian Geodetic Vertical Datum of 1928 (CGVD28), an offset must be applied. The conversions are calculated based on the geoid-ellipsoid separation model, HT2, from Natural Resources Canada.

2.5.3 **Bottom Classification Maps**

Submerged Aquatic Vegetation (SAV) maps were derived from the lidar and orthophotos and included the water depth raster, derived from the DEM, lidar bottom reflectance intensity, and the true-color aerial photograph orthomosaic. The approach used the red and green imagery bands, which were extracted from the true-color aerial photograph orthomosaic. Ratios of their differences and of their sums were added together and weighted by the interlaced lidar intensity data. The result was then normalized by the effects of depth. The resulting raster represents vegetation presence index, and was subject to a threshold procedure to result in a final shapefile of vegetation presence or absence. The procedure to produce the final SAV map involved manual editing of the shapefile using the RGB photos for interpretation, and included removing shadows created by overlapping trees in the imagery and clipping of the dataset to the relevant area.

In addition to the SAV map a full bottom classification map was developed with separate classes for sand, rock with seaweed, and eelgrass. This was a new area of research with numerous challenges, and the resulting map required

significant manual intervention in order to separate the classes. This will be an area of continued research in the future at AGRG.

2.6 Lidar Validation

Ground elevation measurements obtained using the RTK GPS system were used to validate the topographic lidar returns on areas of hard, flat surfaces. At each study area, the GPS antenna was mounted on a vehicle and data were collected along roads within the study areas, and points were collected manually along wharves (green lines on Figure 2.4).

Boat-based ground truth data were used to validate the bathymetric lidar returns (blue dots on Figure 2.4). Although various methods were used to measure depth during fieldwork, for this interim report only points measured using the large pole fitted with the RTK GPS antenna to directly measure the seabed elevation were used for the accuracy assessment; points that measured depth using sonar or a weighted rope were not considered at this time.

For both hard surface and boat-based GPS points, the differences in the GPS elevation and the lidar elevation (ΔZ) were calculated by extracting the lidar elevation from the DEM at the checkpoint and subtracting the lidar elevation from the GPS elevation. GPS points were subject to a quality control assessment such that the standard deviation of the elevation was required to be < 0.05 m.

3 Results

3.1 Lidar Validation

3.1.1 Topographic Validation

At PWRP there were 6818 data points collected along the roads with a calculated mean of ΔZ of -0.07 m \pm 0.03 m; at Merigomish there were 1902 data points collected along the roads with a mean ΔZ of -0.069 m \pm 0.03 m; at Mabou there were 1160 data points collected along the roads, mean ΔZ was 0.09 m \pm 0.04 m.

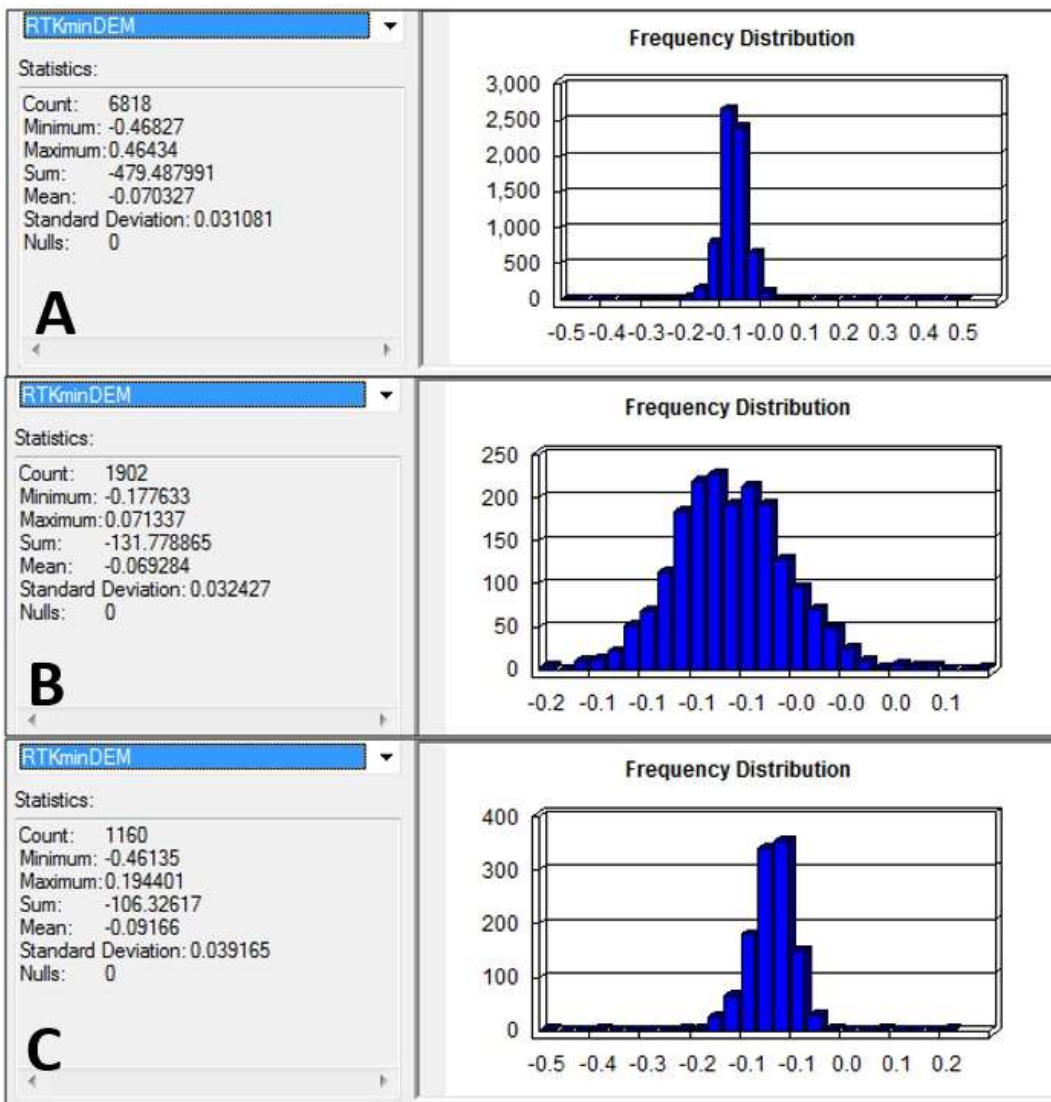


Figure 3.1: Topographic lidar validation for (a) Pugwash-River Philip, (b) Merigomish, and (c) Mabou.

3.1.2 Bathymetric Validation

At all three study areas the mean ΔZ was negative, an indication that the DEM elevation is less (shallower) than the observed GPS point. At Pugwash-River Philip, there were 37 direct seabed elevation measurements with mean ΔZ -0.19 m \pm 0.18 m; at Merigomish, there were 26 direct seabed elevation measurements with mean ΔZ -0.07 m \pm 0.38 m; at Mabou there were 19 direct seabed elevation measurements with mean ΔZ -0.24 m \pm 0.17 m (Figure 3.2). It is possible that the bathymetric laser encountered difficulty in penetrating through the vegetation cover to the seabed, resulting in a derived seabed that is actually representative of the elevation of the eelgrass beds. Further investigation of this issue will follow in the final project report.

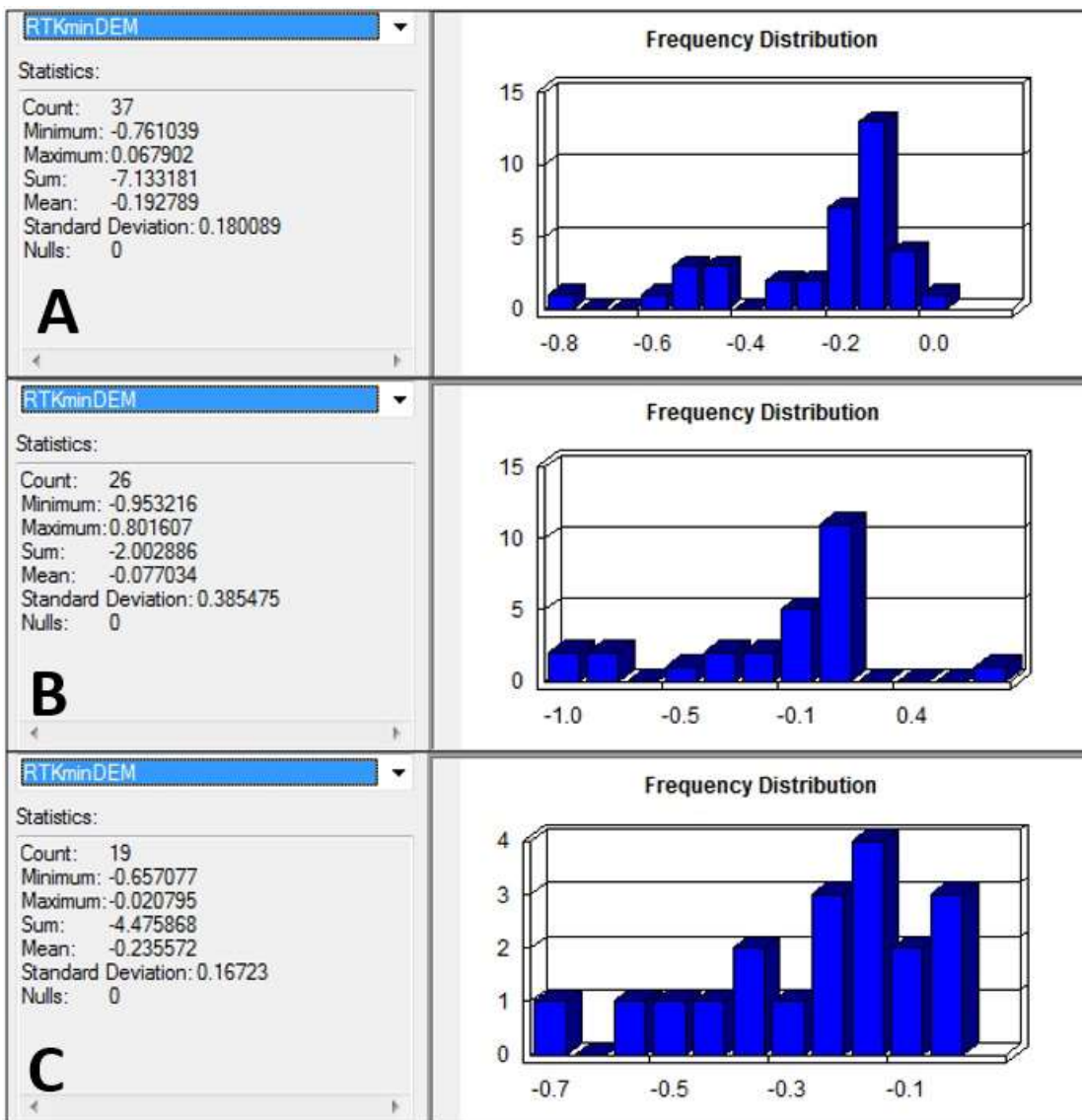


Figure 3.2: Bathymetric lidar validation for (a) Pugwash-River Philip, (b) Merigomish, and (c) Mabou.

3.2 Surface Models and Air Photos

3.2.1 Pugwash-River Philip

The lidar survey at PWRP was successful in penetrating to the seabed in most of the study area; the exceptions were the river channels and the deeper parts of the coastal area (Figure 3.3). The minimum elevation achieved by the lidar was -5.27 m CGVD28 near the river mouths at the coast (note that all elevations reported will be in CGVD28). Outside of the river channels the bathymetry was typically flat and between 0 and -1 m elevation. The sub-panels highlight some of the finer bathymetry details that cannot be seen in the full figure extent. The blue panel shows a tributary where a small stream cuts through the flats towards the main River Philip channel. The lidar reached -2.5 m elevation in River Philip at the edges of the channel, which reached 10 m in some places. The orange panel shows ripples in the sand near outer edge

of the study area and a gently sloping shore, with a change in elevation from the shoreline to -4 m near the edge of the panel. The red panel shows some of the flat parts of the Pugwash River, mostly at -0.5 m, interspersed with narrow tributaries reaching elevations of -2 m.

The Colour Shaded Relief (CSR) models show the topography relief in shades of green-red-yellow, and the bathymetry relief in shades of blue where darker blue represents deeper water (Figure 3.4). CSRs provide an exaggerated relief model (5x actual height) and artificial shading to accentuate topographic and bathymetric features. This map is especially useful for identifying where the land ends and the water begins. At PWRP the differences between River Philip and the Pugwash River are noticeable: River Philip becomes wider, with less flat areas on either side of the channel, whereas the Pugwash River becomes narrower upstream and still shows wide flat areas on either side of the channel. The smaller features highlighted in the panels are easily interpreted in the CSR format.

The orthophoto mosaics provide insights into land use, water clarity, bottom type, wave action, and river morphology. The orthophoto panels show the different levels of water clarity throughout the study area. At PWRP submerged features such as vegetation and the deep river channel can be identified in the blue panel; at the orange panel the sand ripples can be seen; and at the red panel the small tributaries can be discerned with some effort (Figure 3.5). The details that can be seen in the 5 cm resolution orthophotos at a very small scale are highlighted in Figure 3.7.

The Depth Normalized Intensity model (DNIs) can be a powerful tool to reveal submerged features and bottom type information that the air photos and DEM may not show. The intensity data show the contrast between brightly coloured seabed and the dark colour of eelgrass or other submerged vegetation. At PWRP the river channels appear mainly dark, suggesting a large quantity of submerged vegetation, or dark sediment; near the harbour mouth the DNI appears brighter, suggesting a sandy bottom (Figure 3.6).

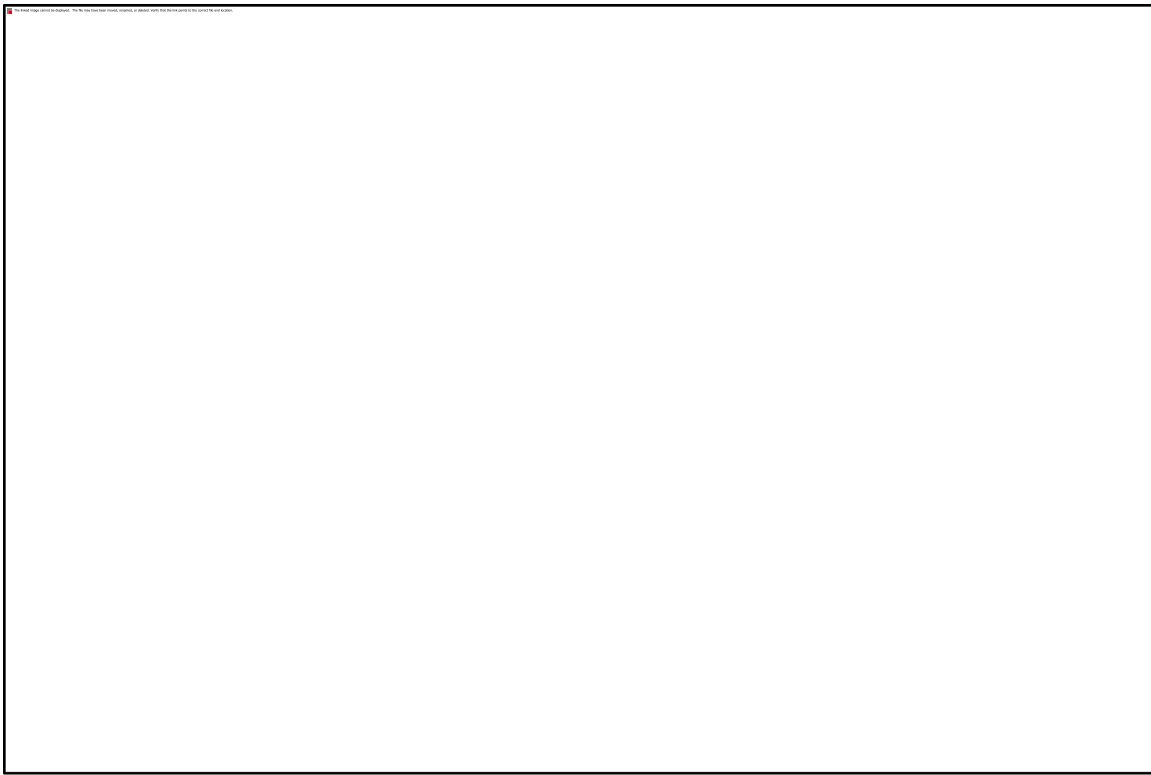


Figure 3.3: Digital Elevation Model for Pugwash-River Philip for entire study area, scaled to show bathymetry relief, and with insets showing smaller features. Insets are matched to the larger figure by border colour.



Figure 3.4: PWRP CSR for entire study area, with insets showing smaller features. Insets are matched to the larger figure by border colour.

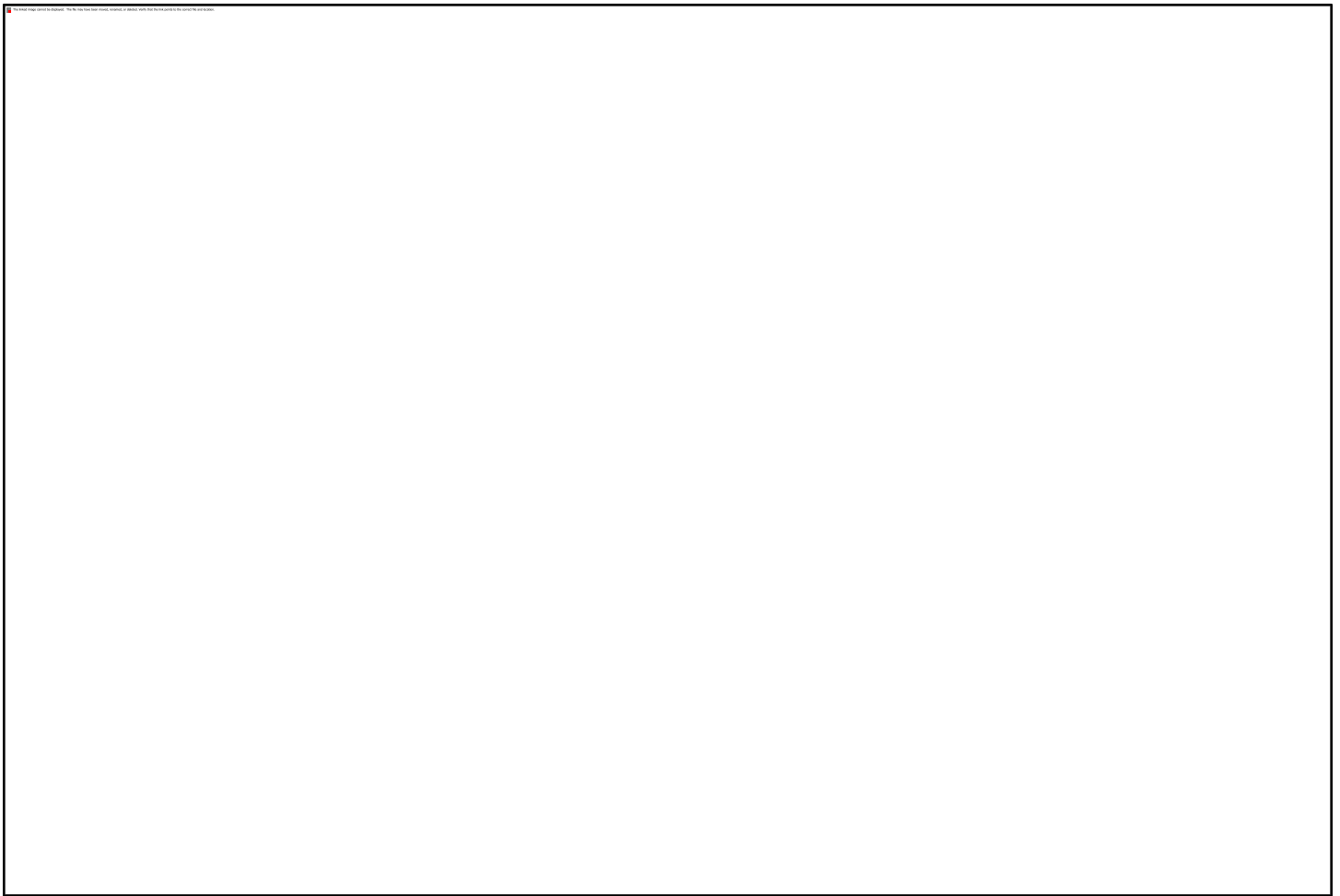


Figure 3.5: PWRP orthophoto mosaic for entire study area with insets showing smaller features. Insets are matched to the larger figure by border colour.

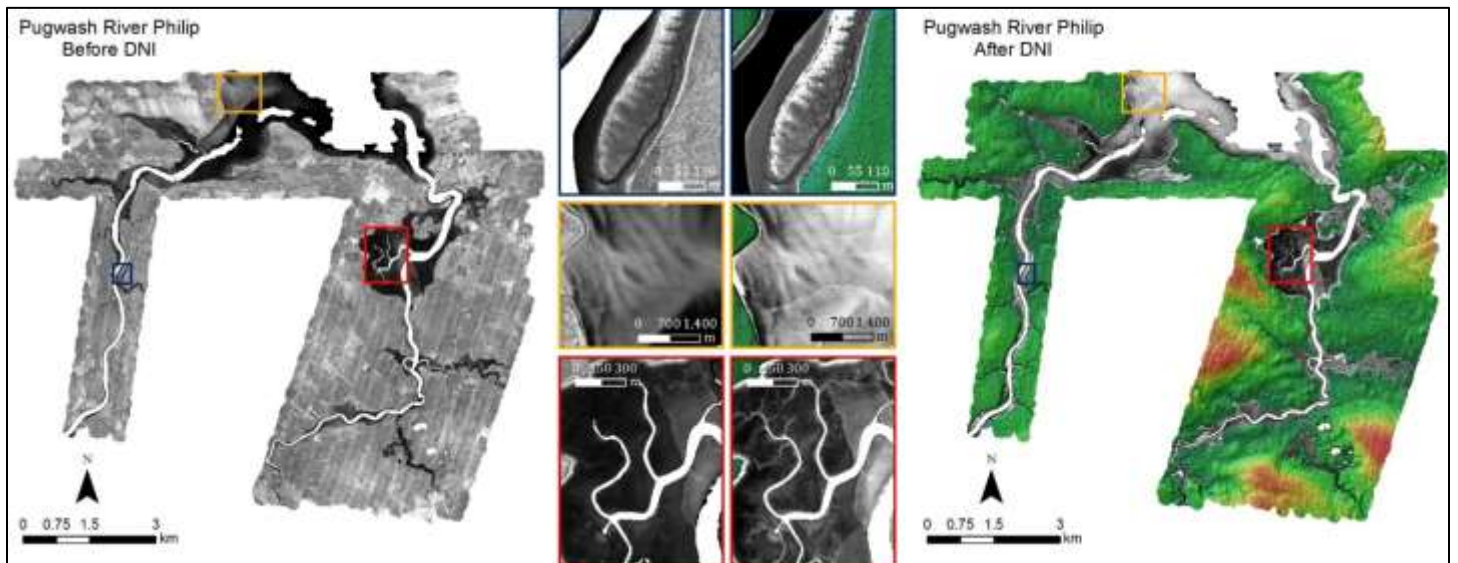


Figure 3.6: Comparison between the intensity model and the depth normalized intensity model for PWRP. The depth normalized intensity is draped over the CSR to add context. The insets show smaller features for both models for comparison purposes. The insets are matched to the larger figure on the left and right by border colour.

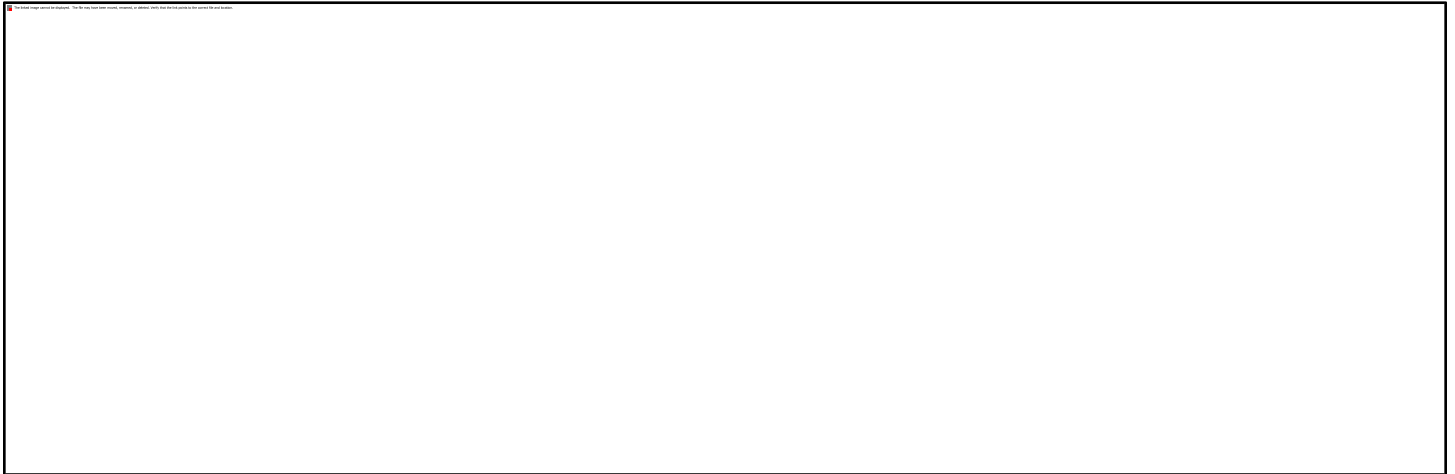


Figure 3.7: Examples of the 5 cm resolution RCD30 orthophotos at a small scale. (a) The AGRG boat with large GPS pole obtaining ground truth measurements at PWRP; (b) aquaculture infrastructure at Merigomish; and (c) cattle grazing less than 100 m from the shoreline in Mabou.

3.2.2 Merigomish

At Merigomish the lidar penetrated to -6.66 m CGVD28 at the seaward edge of the study area, and the majority of elevations deeper than -4 m occurred outside of Merigomish Harbour (Figure 3.8). The lidar did not penetrate to the bottom of the channels or to the bottom of deeper areas in the southern half of the harbour. The blue panel highlights the shallow sand ripples on the backside of the barrier beach in the northern part of the study area; the orange panel shows similar ripples near the harbour mouth; and the red panel shows the changes in bathymetry where a river enters the harbour. The CSR for Merigomish shows a clear separation between land and sea and the panels show bathymetric ripples in finer detail in the blue and orange panels (Figure 3.9). The blue panel appears noisy and suggests that the bathymetric laser was reflecting off the top of eelgrass rather than penetrating to the bottom; this requires further investigation and will be addressed in the final report. The orthophotos add weight to this suspicion, as the blue panel clearly shows sand and then something darker, which is either much deeper bathymetry or vegetation (Figure 3.10). The orthophotos show a variety of land uses, such as agricultural, residential, and beach. The DNI suggests sandy areas outside the harbour and at the harbour mouth, while the dark areas of the DNI suggest submerged vegetation (Figure 3.11).



Figure 3.8: Digital Elevation Model for Merigomish, scaled to show bathymetry relief, for entire study area (rotated 54° to the north), and with insets showing smaller features. Insets are matched to the larger figure by border colour.

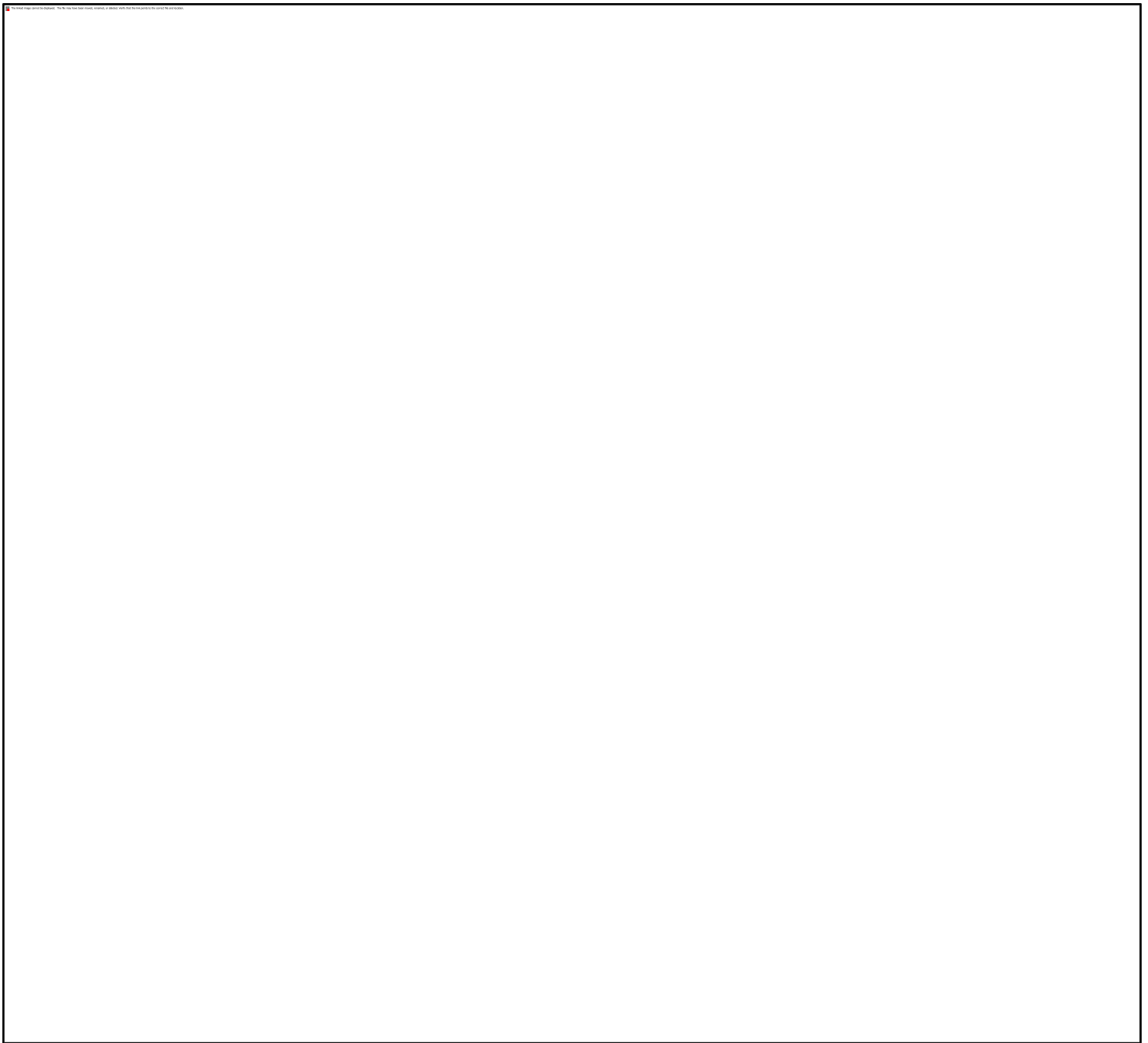


Figure 3.9: Merigomish CSR for entire study area (rotated 54° to the north), with insets showing smaller features. Insets are matched to the larger figure by border colour.

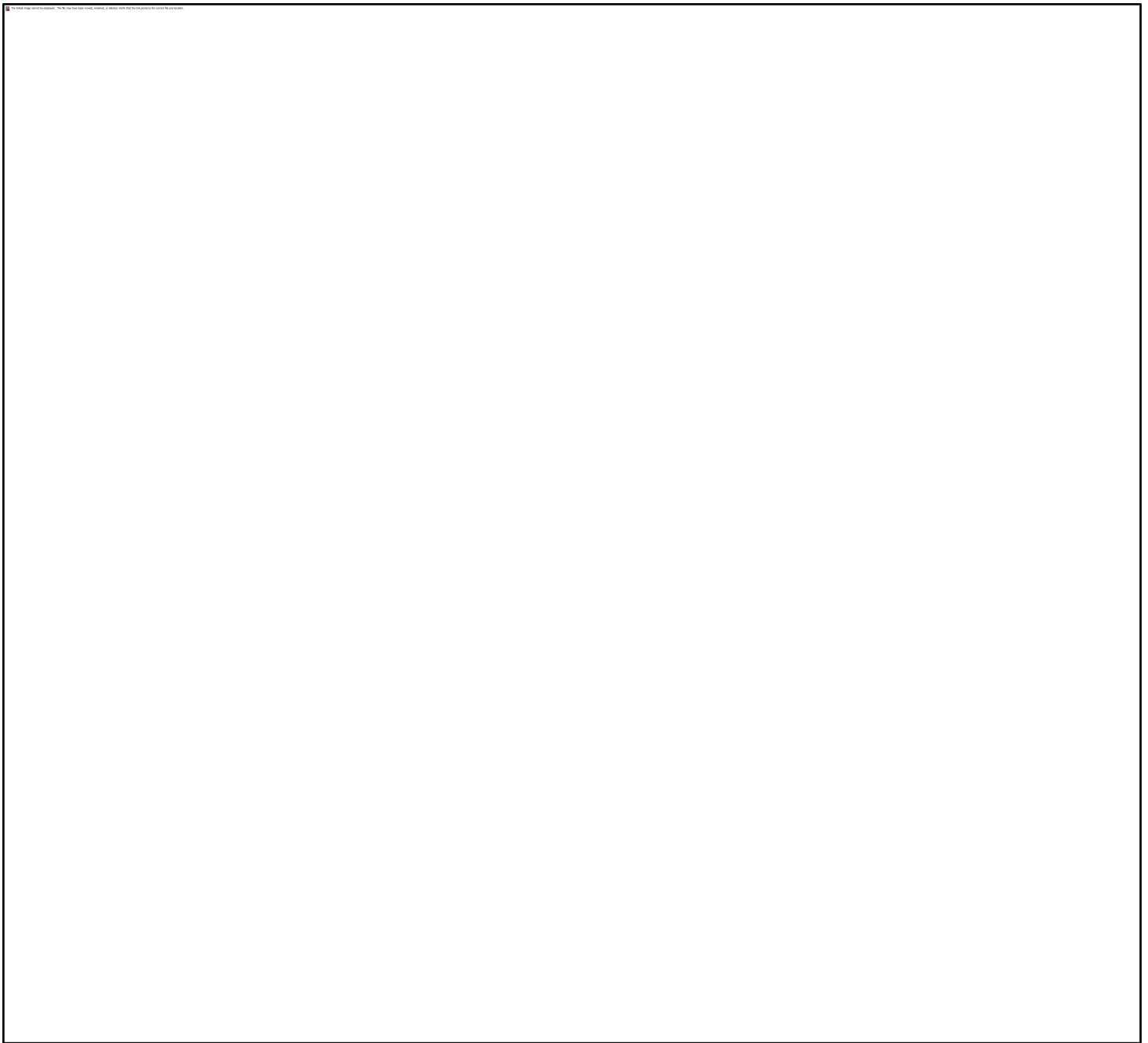


Figure 3.10: Merigomish orthophoto mosaic for entire study area (rotated 54° to the north), with insets showing smaller features. Insets are matched to the larger figure by border colour.

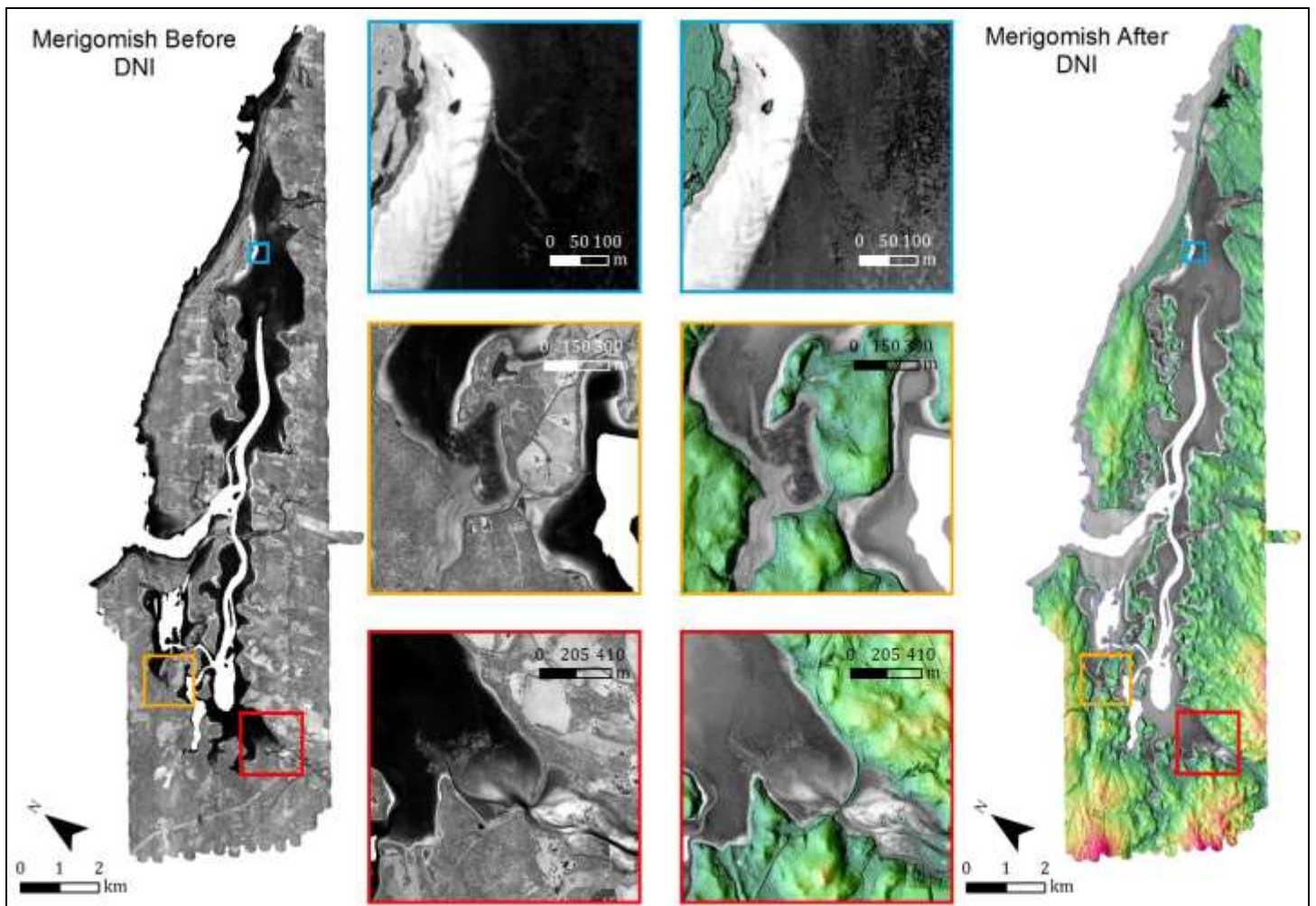


Figure 3.11: Comparison between the intensity model and the depth normalized intensity model for Merigomish (rotated 54°). The depth normalized intensity is draped over the CSR to add context. The insets show smaller features for both models for comparison purposes. The insets are matched to the larger figure on the left and right by border colour.

3.2.3 Mabou

The lidar was successful in penetrating through the water outside of Mabou Harbour and reached its minimum elevation of -12.66 m there (Figure 3.12). There was good penetration in the westward end of the harbour, up to -6 m in the channel, and in the shallow areas where rivers enter the harbour. However, the main portion of the harbour was not successfully penetrated, aside from the area very near the shoreline, which appeared to drop off quickly to deeper water. The lack of penetration was likely due to a combination of water clarity and depth issues, and will be discussed in the final project report. The blue panel emphasizes the excellent penetration outside of the harbour; the orange and red panels show the success of the lidar in the river channel areas. The Colour Shaded Relief map shows the topography relief in shades of green-red-yellow, and the bathymetry relief in shades of blue where darker blue represents deeper water (Figure 3.13). This map is especially useful for identifying where the land ends and the water begins. The orthophoto mosaic provides

insights into land use, water clarity, bottom type, wave action, and river morphology (Figure 3.14). The differences in apparent water clarity match the lidar penetration remarkably. The depth normalized intensity model (DNI) for Mabou, similarly to PWRP and MERI, shows bright areas where sand is known to exist, and dark areas where the bottom is likely vegetation (Figure 3.15).

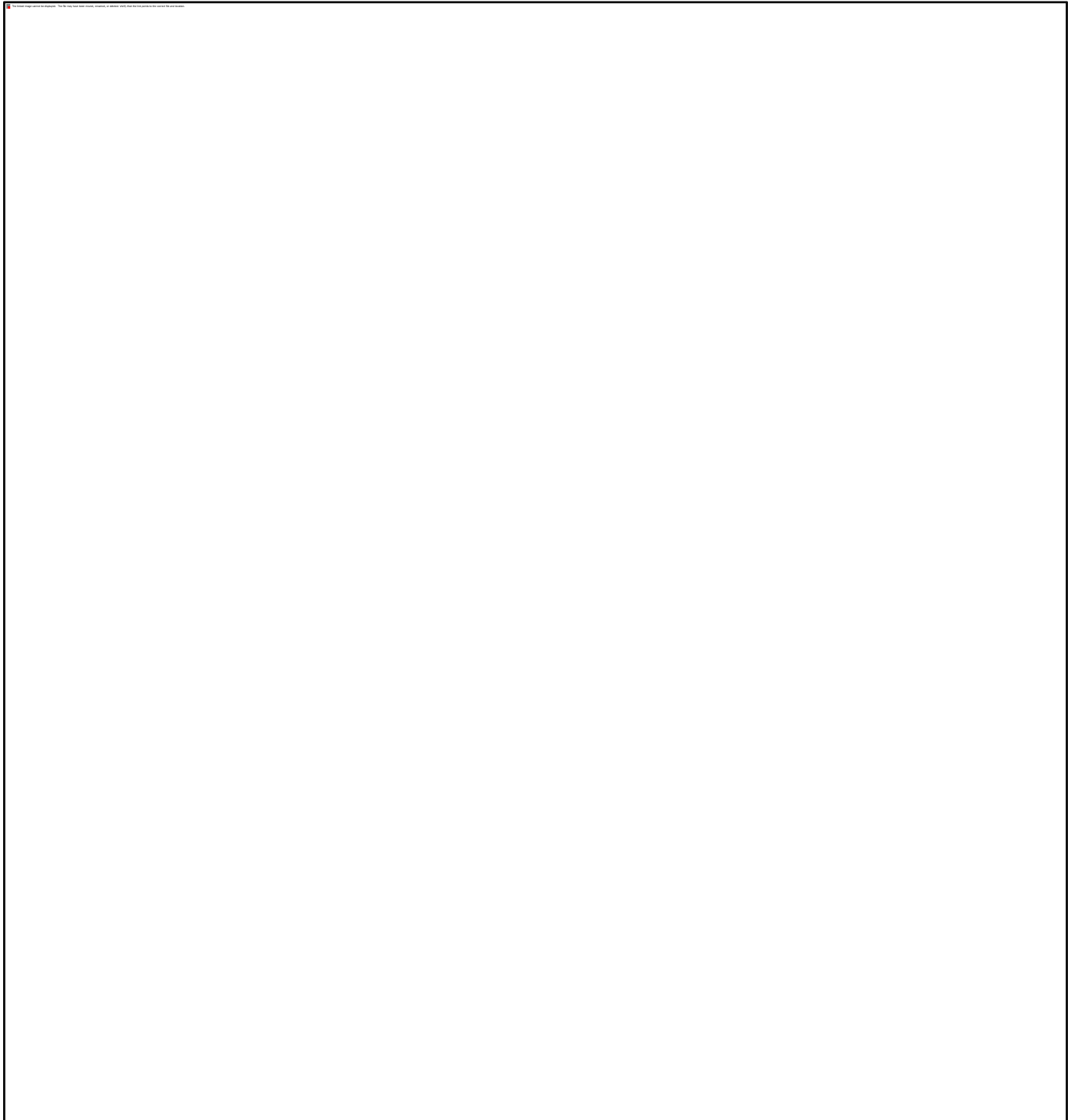


Figure 3.12: Digital Elevation Model for Mabou, scaled to show bathymetry relief, for entire study area (rotated 9° to the north), and with insets showing smaller features. Insets are matched to the larger figure by border colour.

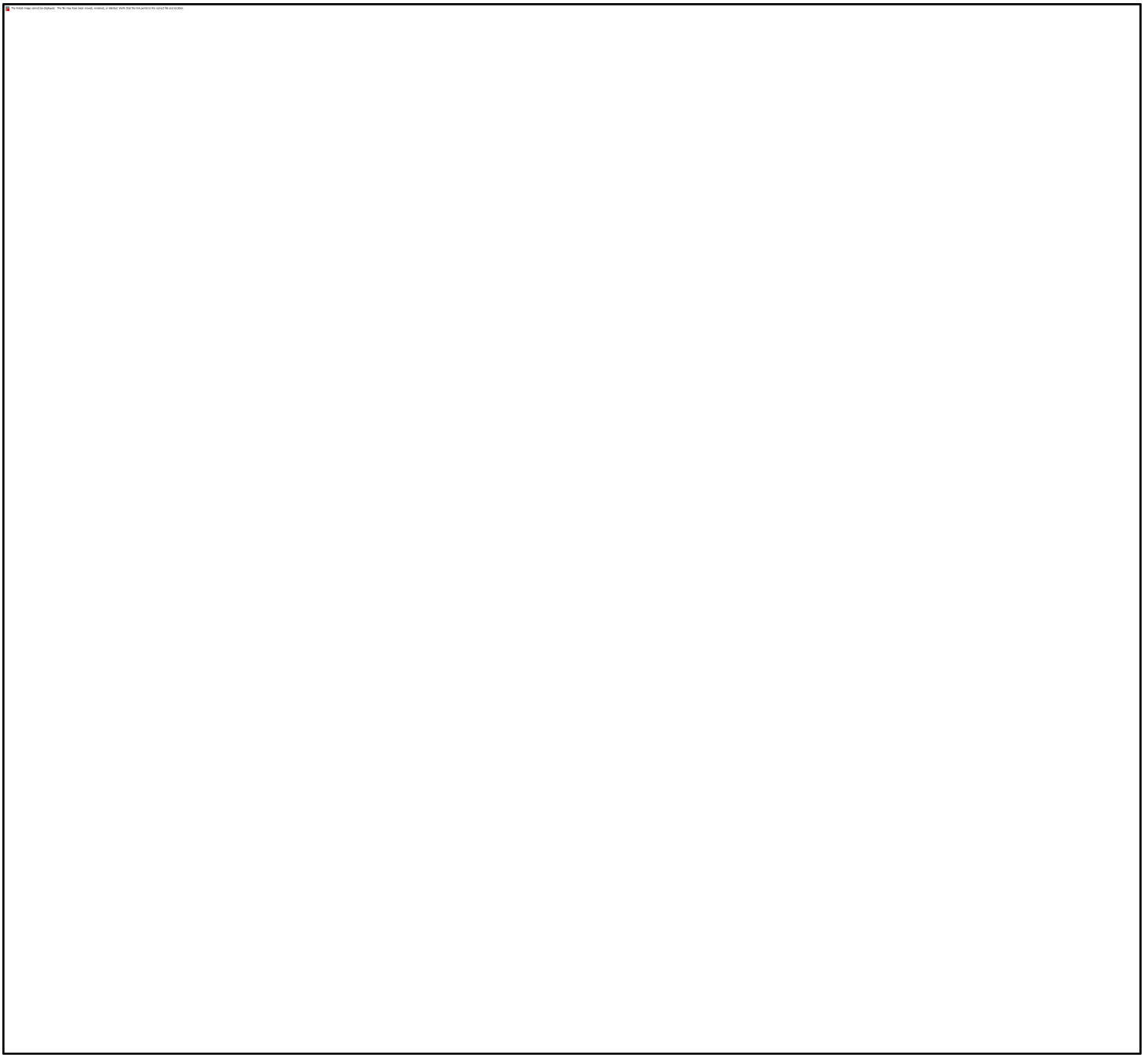


Figure 3.13: Mabou CSR for entire study area (rotated 9° to the north), with insets showing smaller features. Insets are matched to the larger figure by border colour.

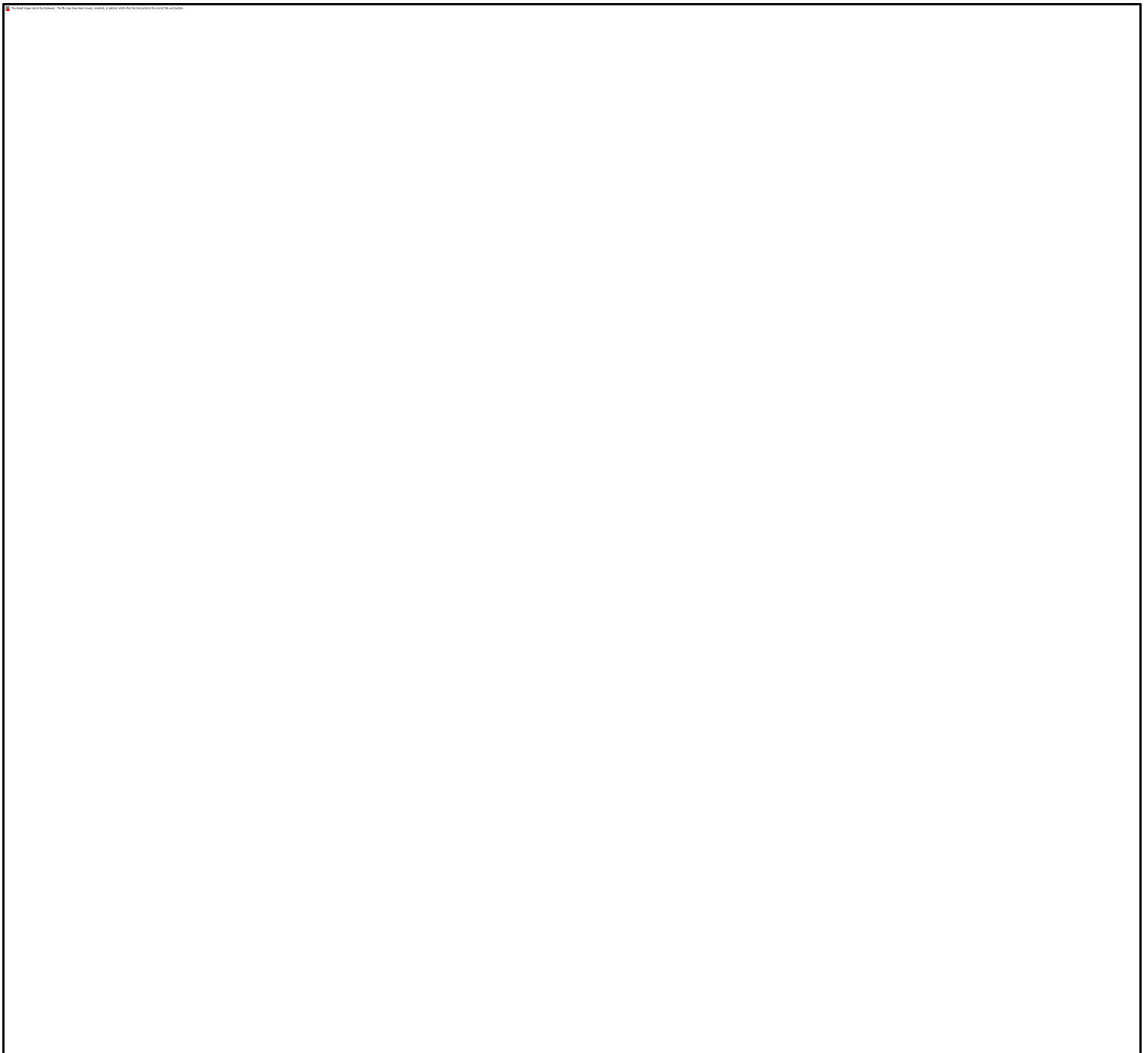


Figure 3.14: Mabou orthophoto mosaic for entire study area (rotated 9° to the north), with insets showing smaller features. Insets are matched to the larger figure by border colour.

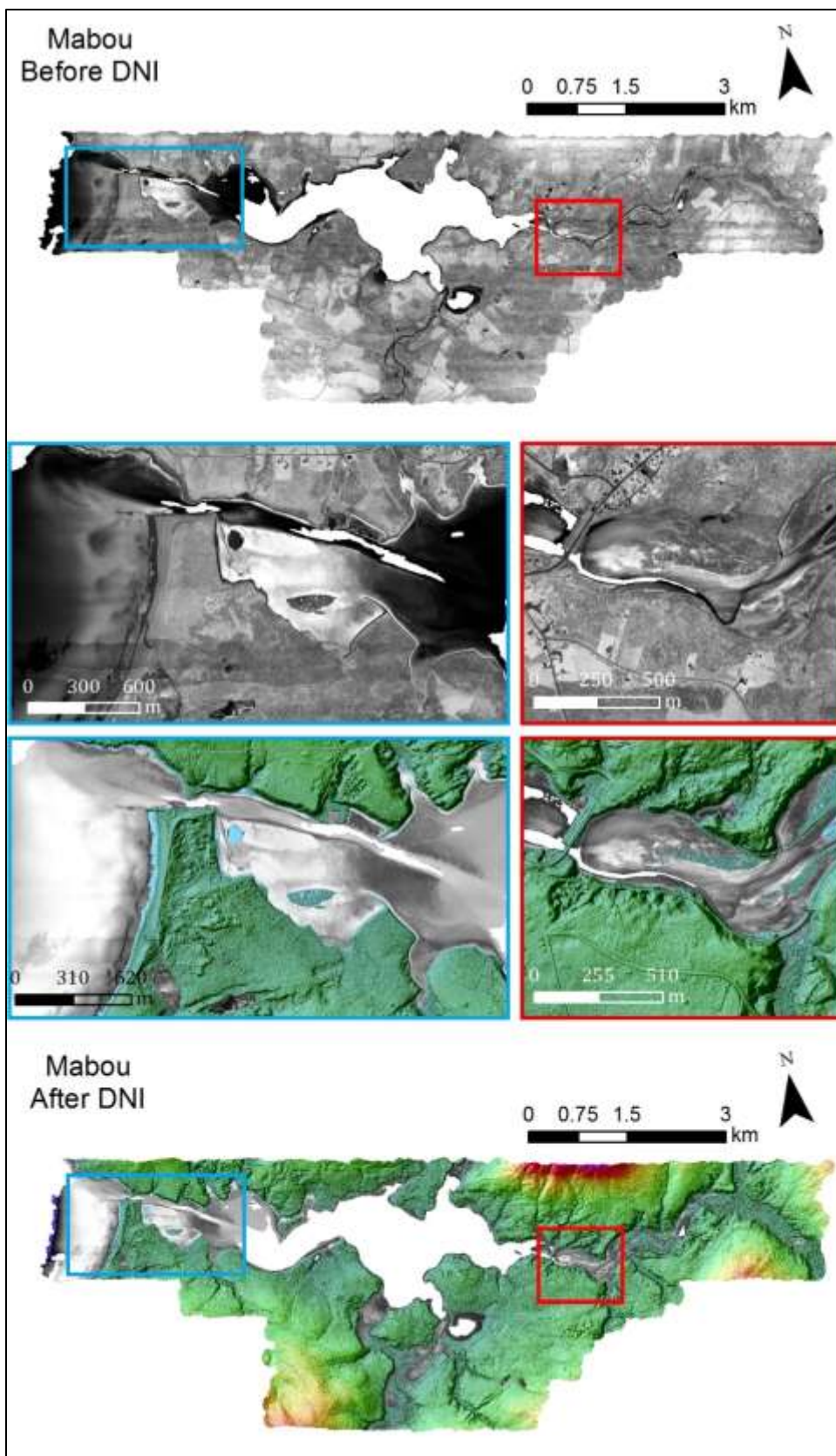


Figure 3.15: Comparison between the intensity model and the depth normalized intensity model for Mabou. The depth normalized intensity is draped over the CSR to add context. The insets show smaller features for both models for comparison purposes. The insets are matched to the larger figure on the left and right by border colour.

3.3 Depth Distribution

The distribution of depth within each lidar study area was calculated (Figure 3.16, Table 3.1). The depth distribution histograms provide information on how much of the study area fell into each depth range, and how deep the lidar penetrated, while the table provides the square kilometers of lidar study area that fell within each depth contour. Each of the three study areas were predominantly shallow bays, with most of the observations falling in the top 1 or 2 m.

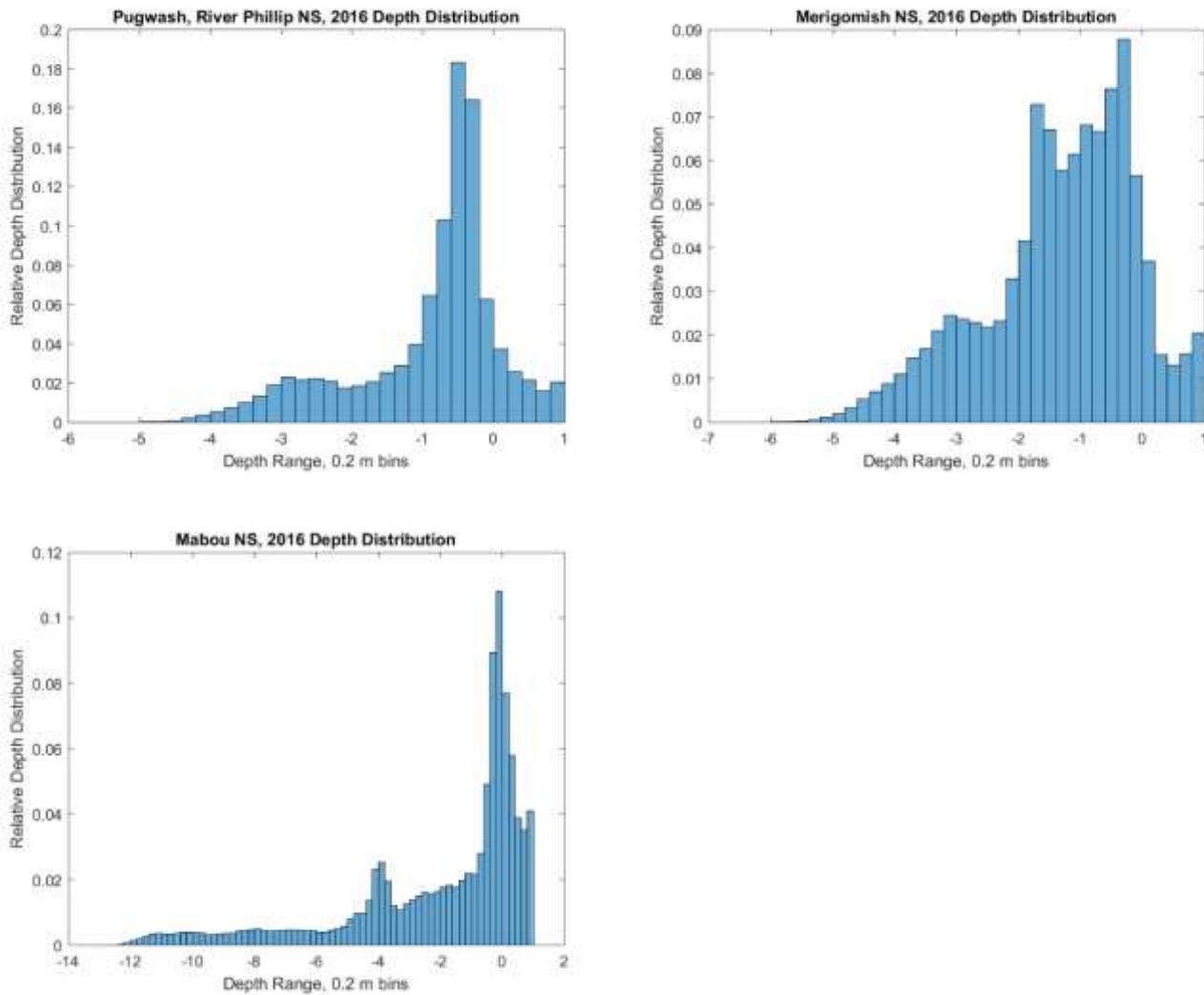


Figure 3.16: Relative depth distribution (relative number of observations: number of observations in bin / total number of observations) separated into 0.20 m depth bins.

Contour	PWRP		Merigomish		Mabou	
	Area (km ²)	% Total Area	Area (km ²)	% Total Area	Area (km ²)	% Total Area
0 < z <= 1	1.67	12	2.91	10	1.32	25
-1 < z <= 0	8.00	58	10.18	36	1.57	30
-2 < z <= -1	1.85	13	8.61	30	0.50	10
-3 < z <= -2	1.46	11	3.57	12	0.41	8
-4 < z <= -3	0.76	6	2.53	9	0.42	8
-5 < z <= -4	0.10	1	0.76	3	0.34	6
-6 < z <= -5	0.0002	0	0.07	0	0.12	2
-7 < z <= -6			0.001	0	0.12	2
z < -7					0.48	9
SUM	13.84	100	28.62	100	5.30	100

Table 3.1: Area of lidar DEM per depth contour, for each study area.

3.4 Bottom Imagery

The underwater photographs taken using a GoPro camera are useful indicators of bottom type throughout the study areas. The following sections present some of the images obtained during the field season displayed on the RCD30 5 cm resolution orthophoto mosaics.

3.4.1 Pugwash-River Philip

The bottom type at the mouths of the Pugwash River and River Philip was a combination of sand and thick, healthy eelgrass, and the water appears clear (Figure 3.17, Figure 3.18). Farther upstream in River Philip the water colour is darker and the bottom type appears to be composed mainly of mud and sand (Figure 3.19).

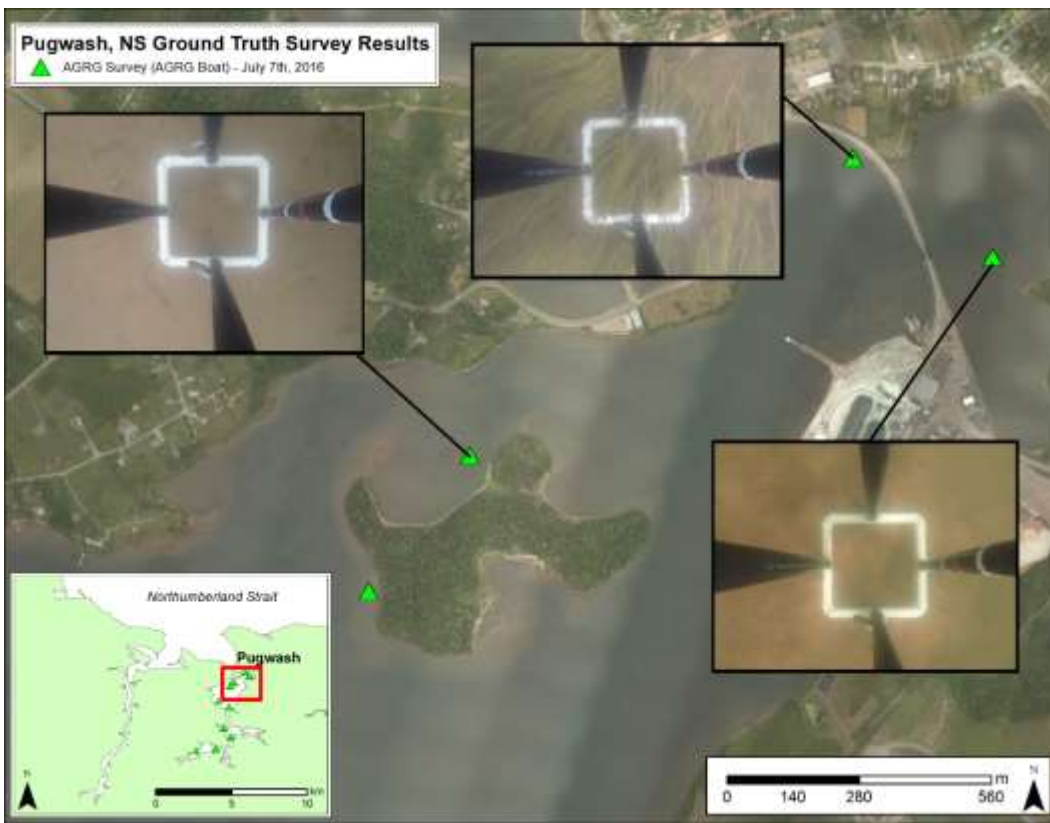


Figure 3.17: Pugwash River underwater photo ground truth. Background image is RCD30 orthophoto RGB mosaic.

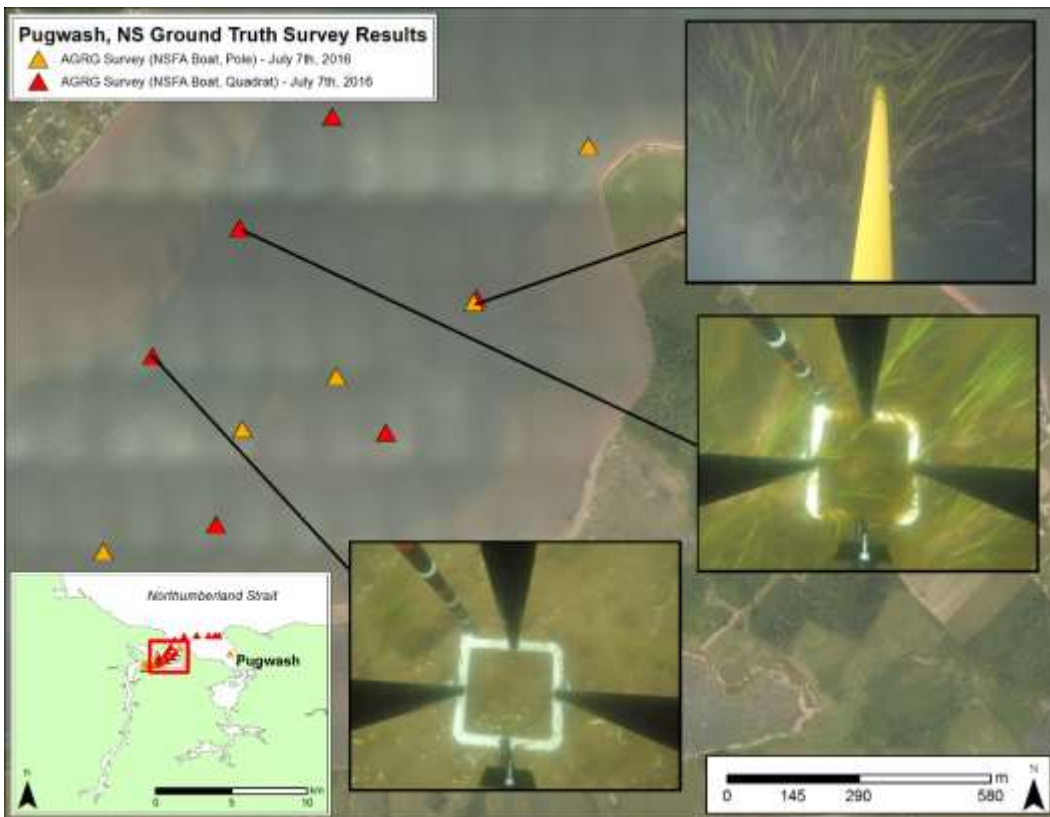


Figure 3.18: Mouth of River Philip underwater photo ground truth. Background image is RCD30 orthophoto RGB mosaic.

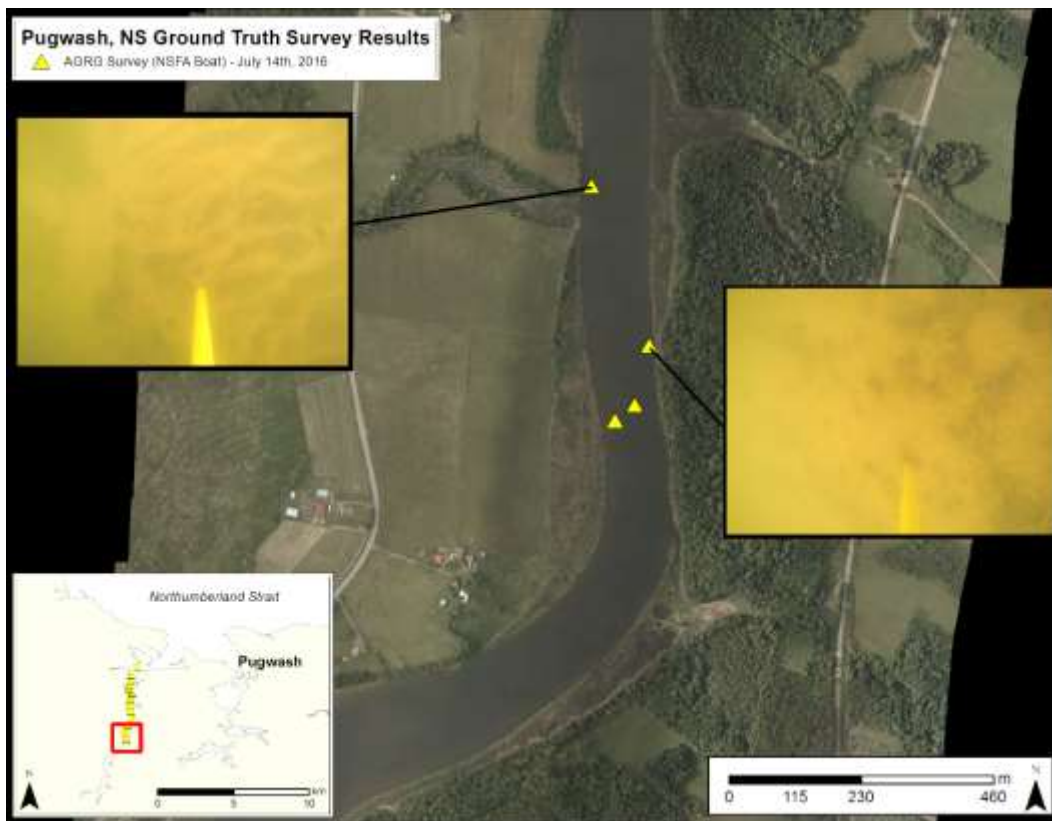


Figure 3.19: River Philip underwater photo ground truth. Background image is RCD30 orthophoto RGB mosaic.

3.4.2 Merigomish

The seaward side of Merigomish Harbour appears to be characterized by a sandy bottom with focus or rockweed (Figure 3.20, Figure 3.21), whereas the inner harbour appears to contain thick, healthy eelgrass growing on a sandy bottom (Figure 3.20 - Figure 3.22). Water clarity appears good both inside and outside the harbour.



Figure 3.20: Merigomish underwater photo ground truth. Background image is RCD30 orthophoto RGB mosaic.

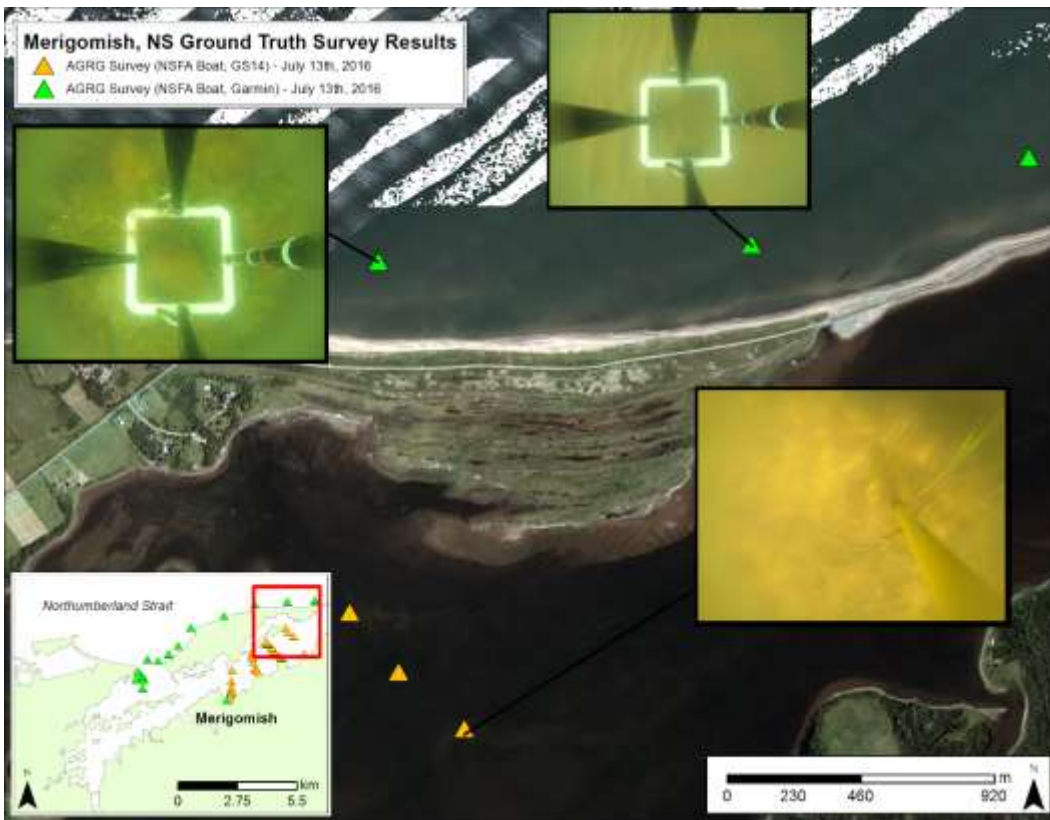


Figure 3.21: Merigomish underwater photo ground truth. Background image is RCD30 orthophoto RGB mosaic.

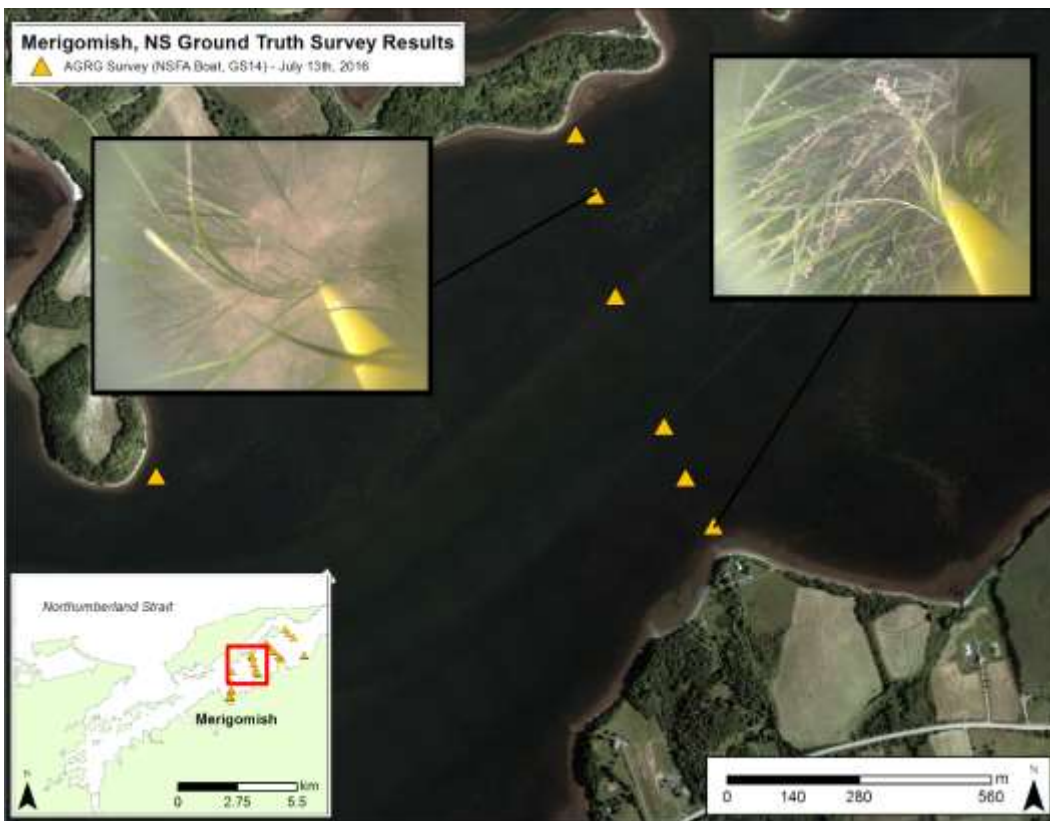


Figure 3.22: Merigomish underwater photo ground truth. Background image is RCD30 orthophoto RGB mosaic.

3.4.3 Mabou

The bottom at Mabou contains patches of eelgrass throughout the length of the inlet, and sediment such as mud, sand, and other vegetation (Figure 3.23 - Figure 3.26). The eelgrass appears thicker and healthier in the clearer water near the harbour mouth, and becomes sparser and browner nearer the mouth of the rivers where the water clarity is moderately reduced.



Figure 3.23: Mabou underwater photo ground truth. Background image is RCD30 orthophoto RGB mosaic.

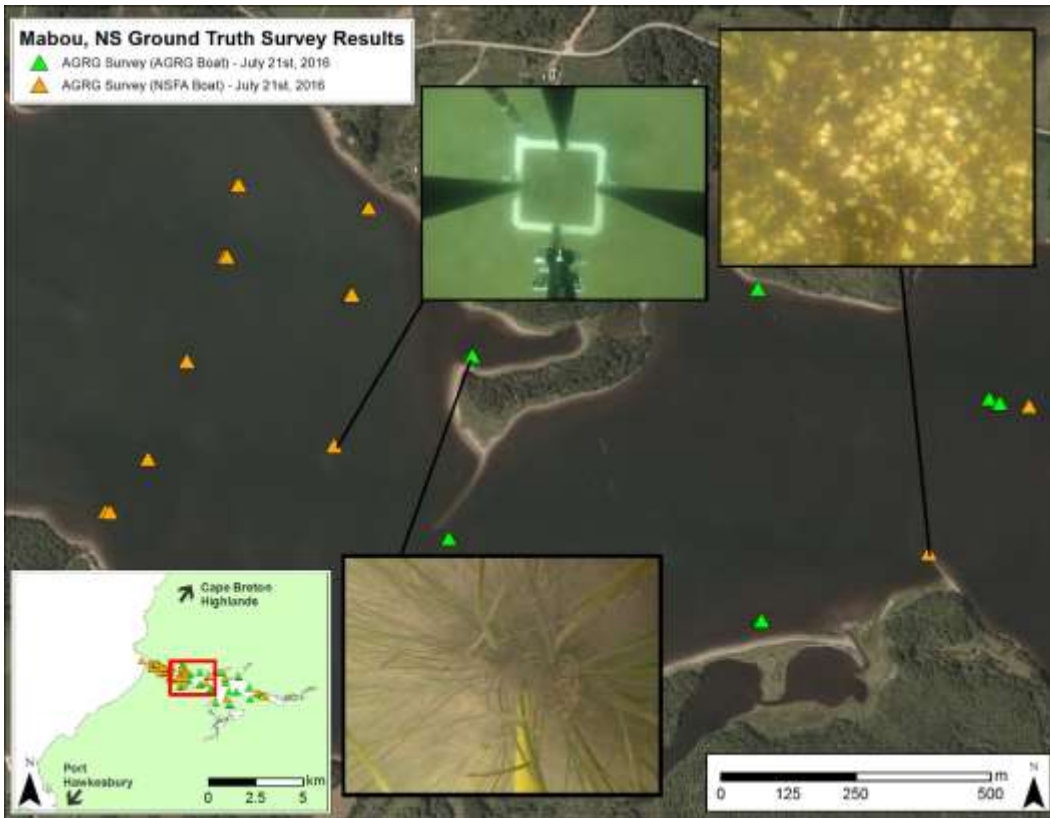


Figure 3.24: Mabou underwater photo ground truth. Background image is RCD30 orthophoto RGB mosaic.

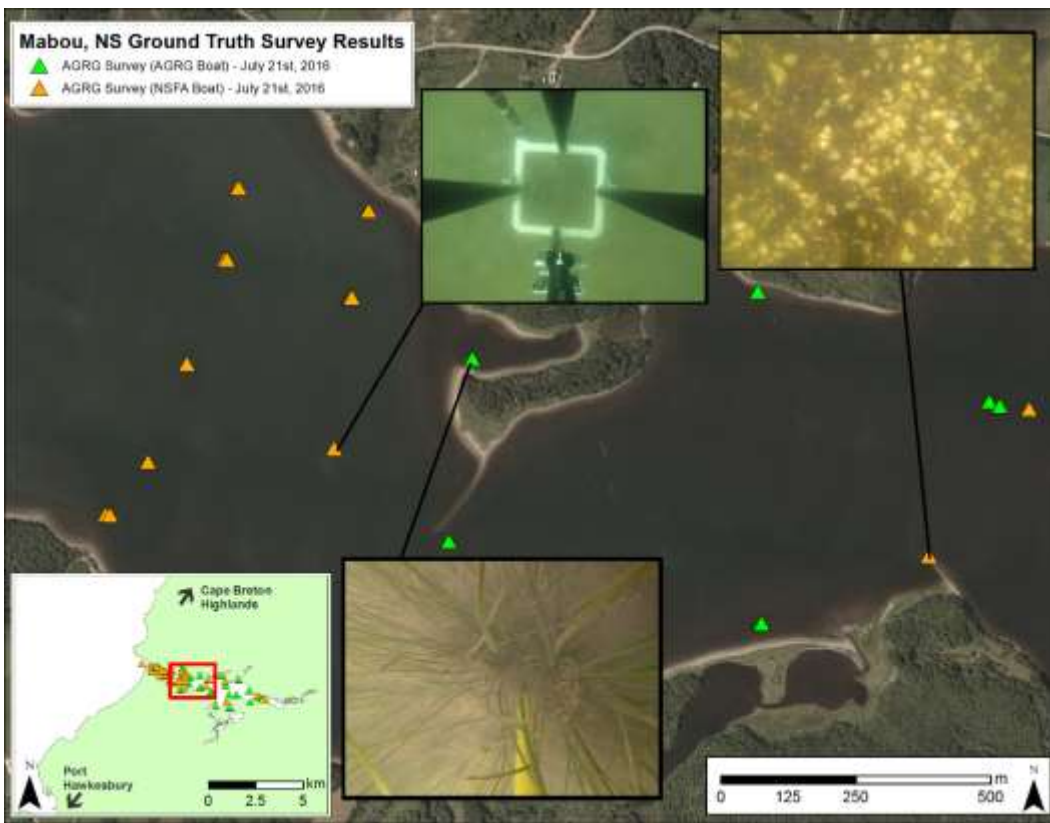


Figure 3.25: Mabou underwater photo ground truth. Background image is RCD30 orthophoto RGB mosaic.

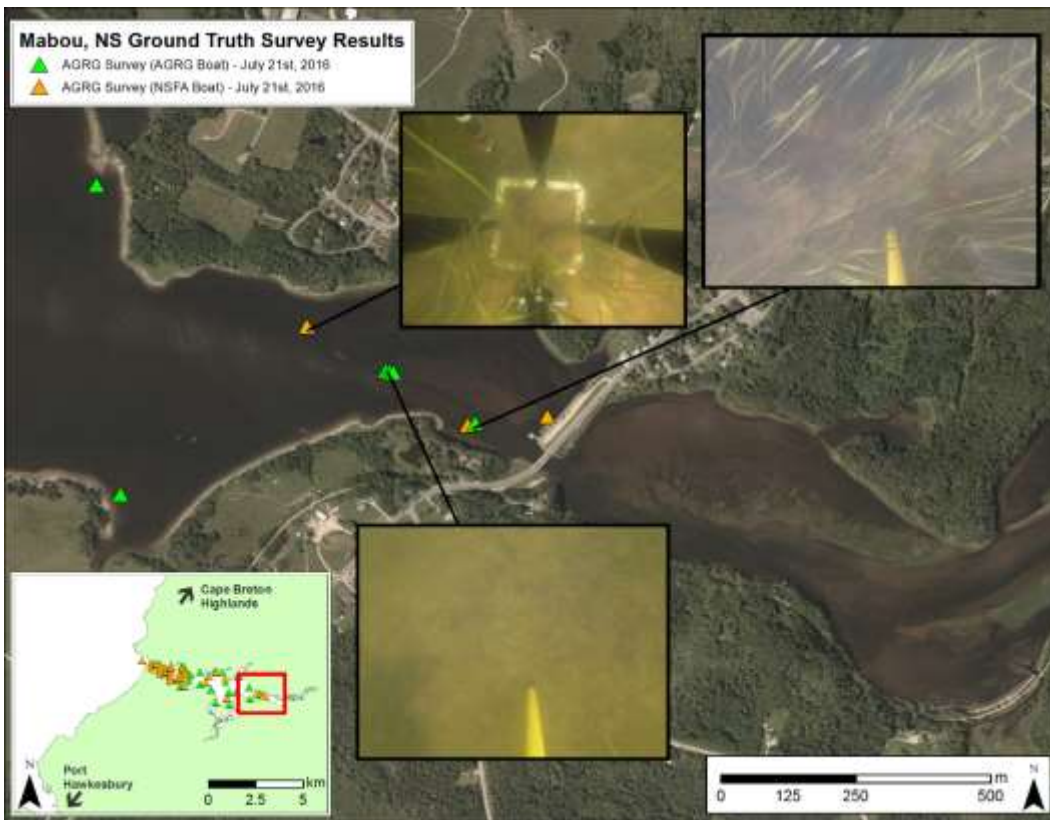


Figure 3.26: Mabou underwater photo ground truth. Background image is RCD30 orthophoto RGB mosaic.

3.5 Bottom Classification Maps

3.5.1 Submerged Aquatic Vegetation Maps

The submerged aquatic vegetation (SAV) maps developed using the lidar and photo products were compared to bottom classification data collected by AGRG using the GoPro underwater camera imagery presented in Section 3.4. Agreement of the SAV classification and the imagery ranged from 80% to 84% (Table 3.2, Figure 3.27, Figure 3.28, Figure 3.31, Figure 3.32). At Merigomish and Mabou the SAV maps were evaluated against bottom classification data collected by DFO using a BioSonics instrument, which uses acoustics to map the submerged vegetation. At Merigomish, the derived SAV map agreed 83% of the time with the BioSonics vegetation detection map (Table 3.2, Figure 3.29, Figure 3.30). At Mabou the derived SAV map agreed 59% of the time with the BioSonics vegetation detection map (Table 3.2, Figure 3.33, Figure 3.34).

Study Area	% Agreement of Eelgrass – AGRG Quadrat Camera Drops	% Agreement of Eelgrass - Biosonics	% Eelgrass
Pugwash-River Philip	80%	N/A	28%
Merigomish	83%	83%	33%
Mabou	84%	59%	27%

Table 3.2: Percentage agreement of eelgrass with AGRG drops and Biosonics and for each area, and the proportion of the lidar study area classified as eelgrass.

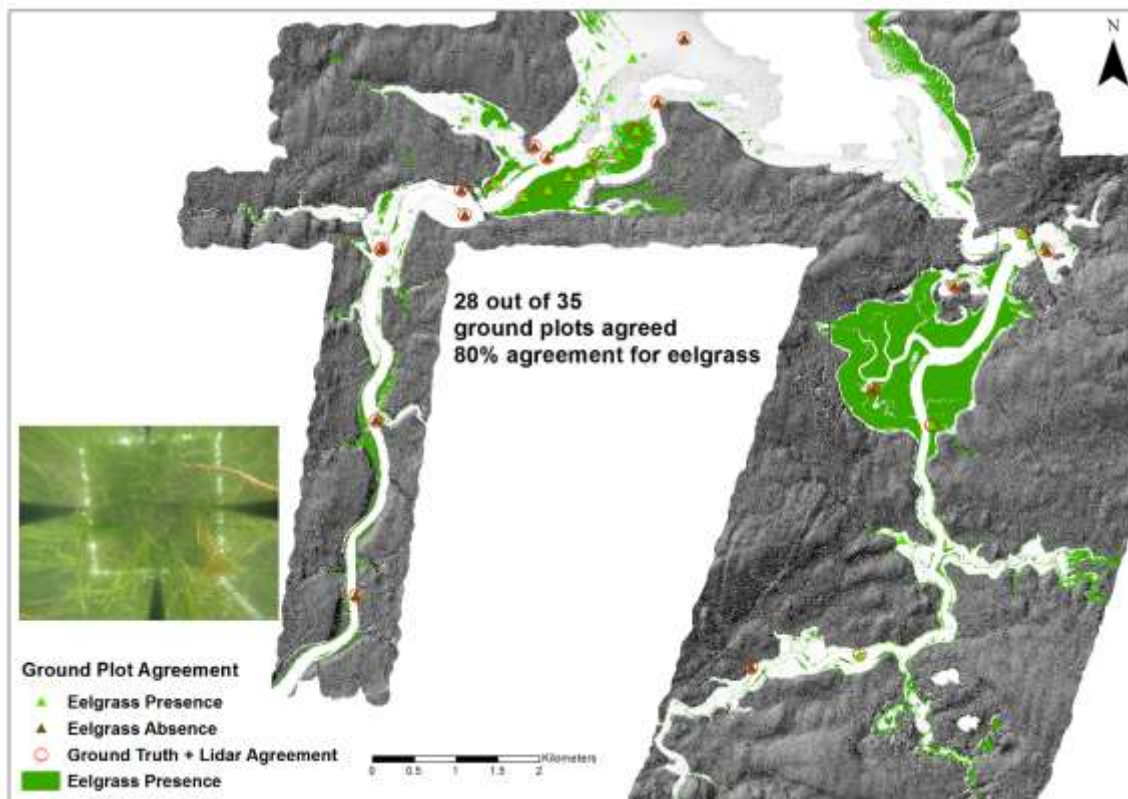


Figure 3.27: Correlation between eelgrass presence and AGRG ground truth results in PWRP.

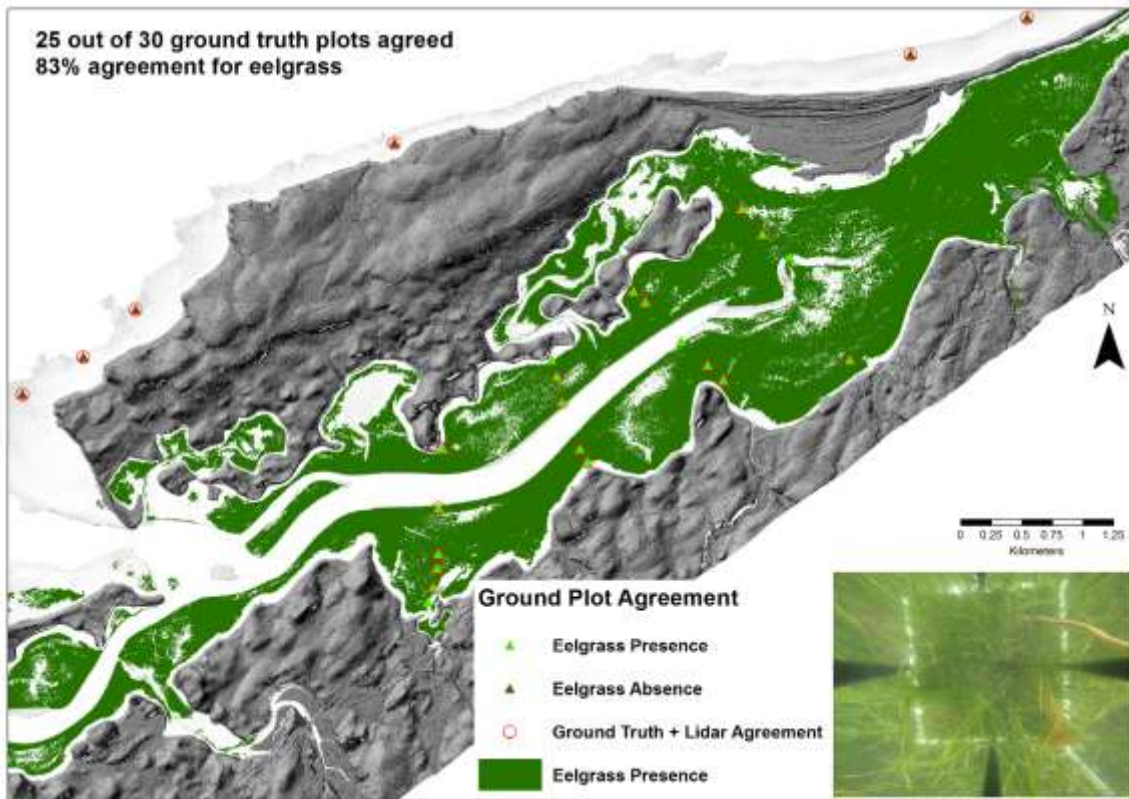


Figure 3.28: Correlation between eelgrass presence and AGRG ground truth results in northeast Merigomish Harbour.

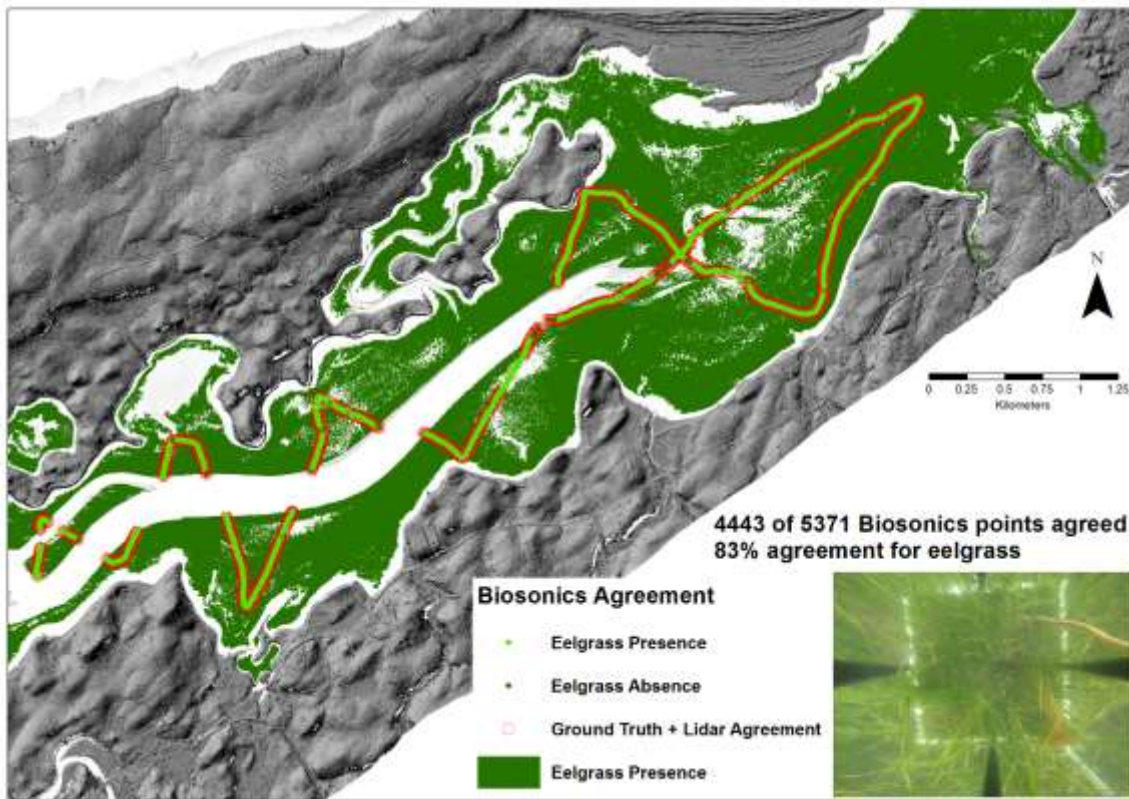


Figure 3.29: Correlation between eelgrass presence and DFO Biosonics results in northeast Merigomish Harbour.

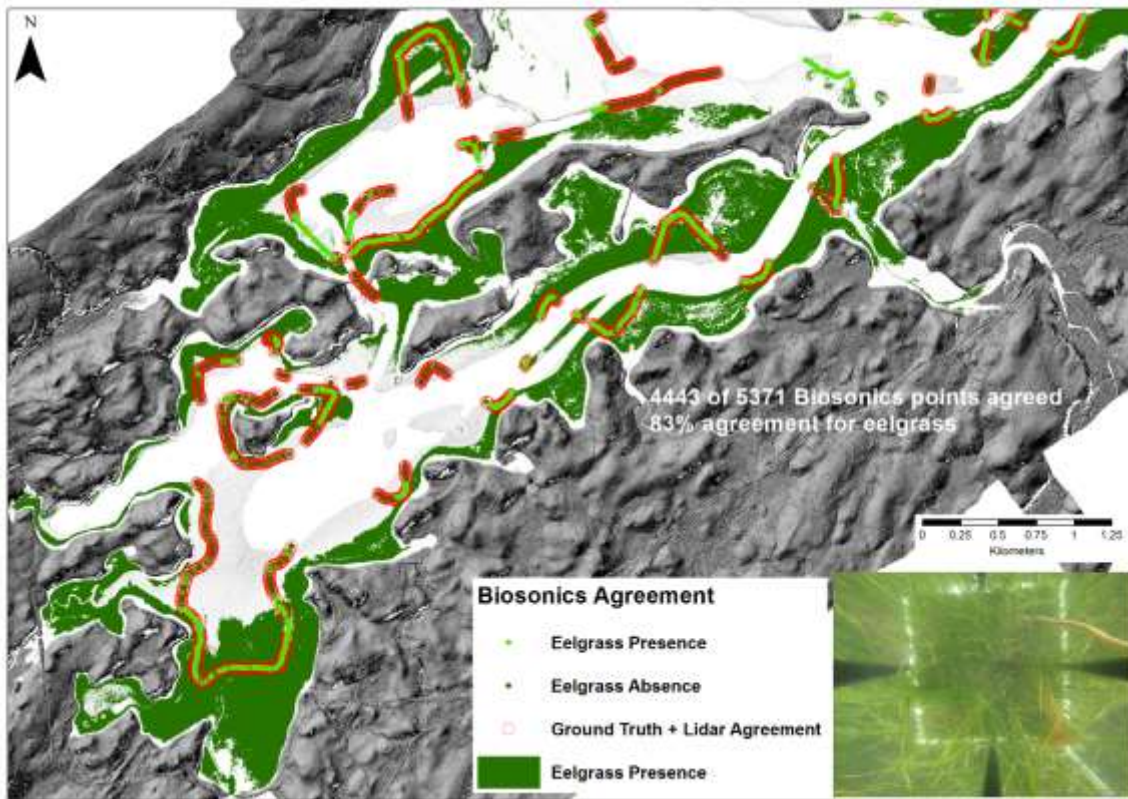


Figure 3.30: Correlation between eelgrass presence and DFO Biosonics results in southwest Merigomish Harbour.

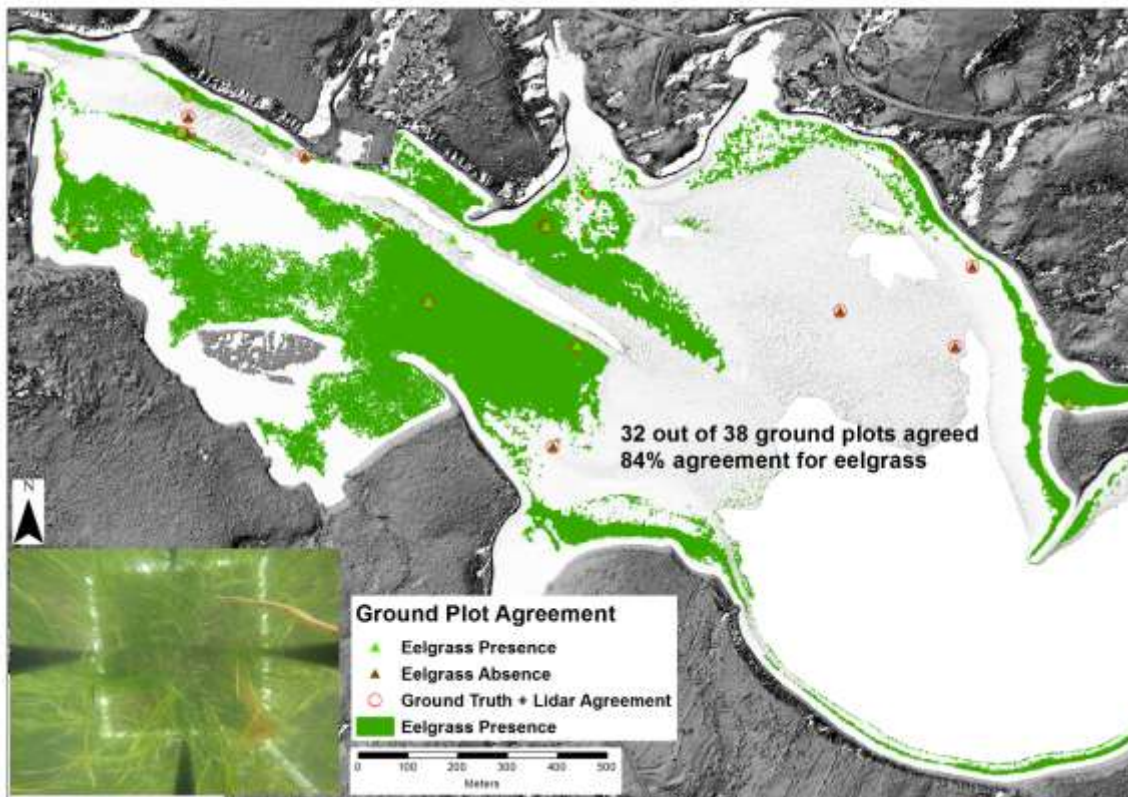


Figure 3.31: Correlation between eelgrass presence and AGRG ground truth results in Western Mabou Harbour.

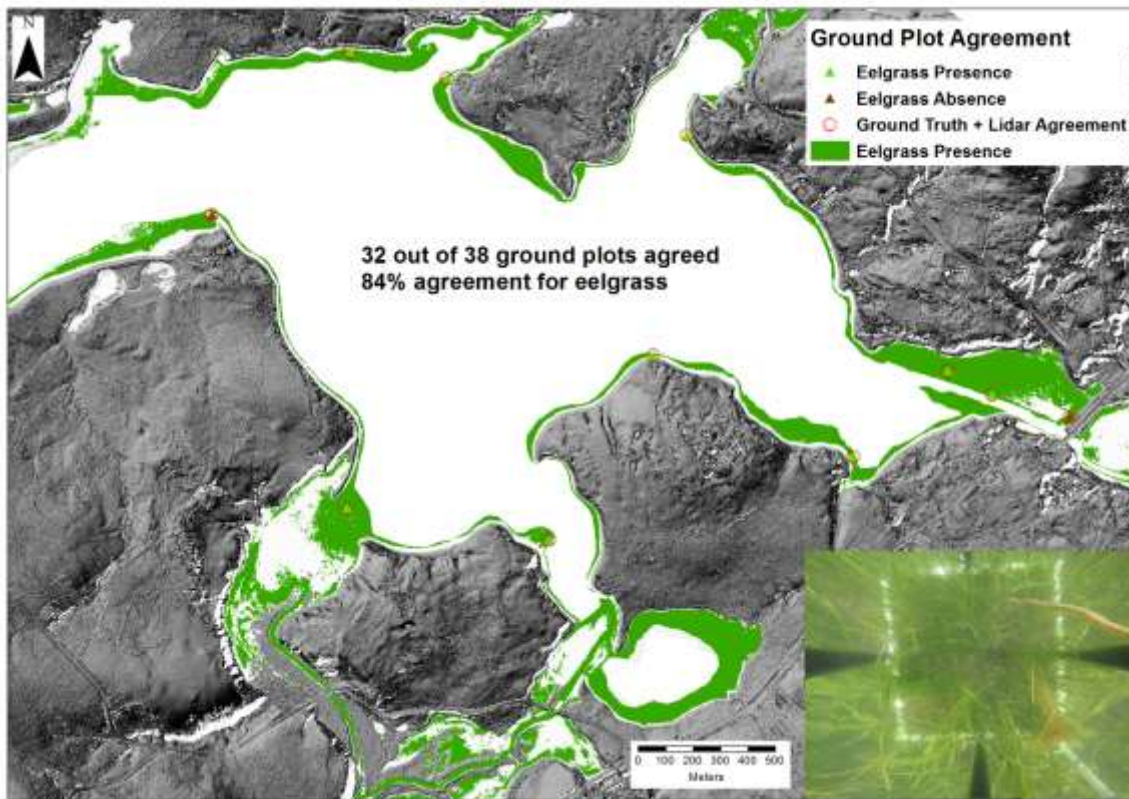


Figure 3.32: Correlation between eelgrass presence and AGRG ground truth results in Eastern Mabou Harbour.

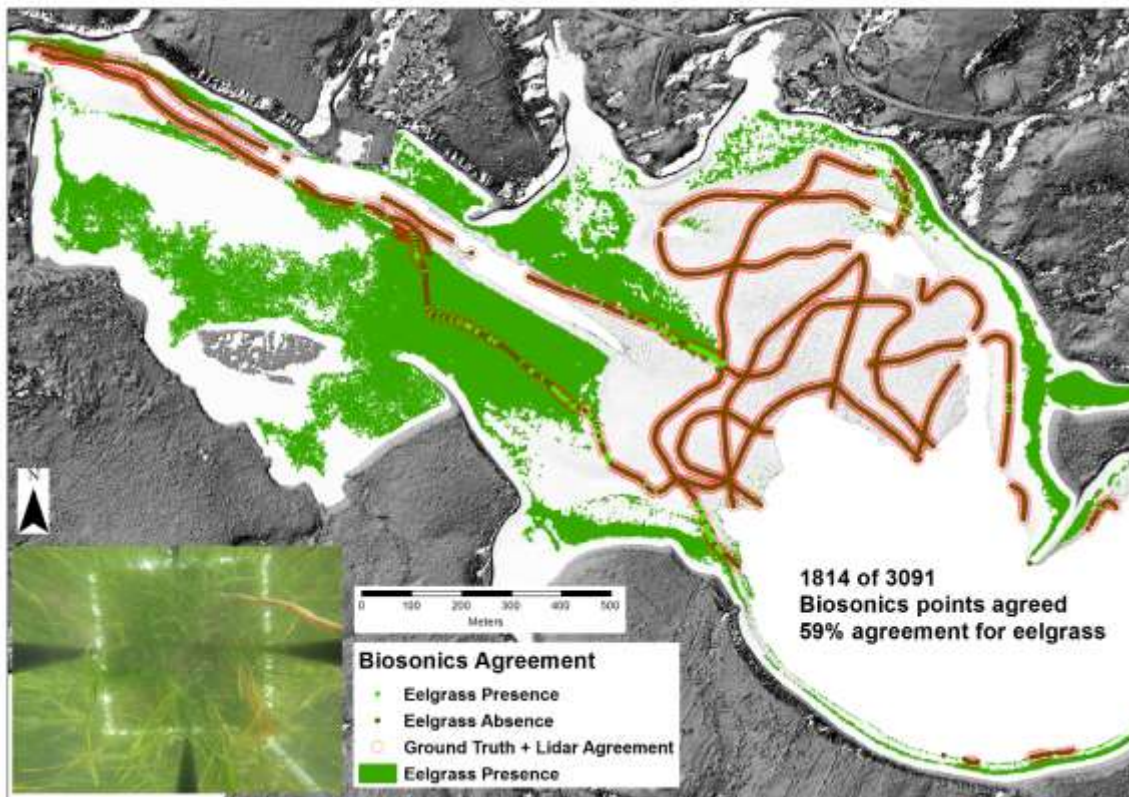


Figure 3.33: Correlation between eelgrass presence and DFO Biosonics results in Western Mabou Harbour.

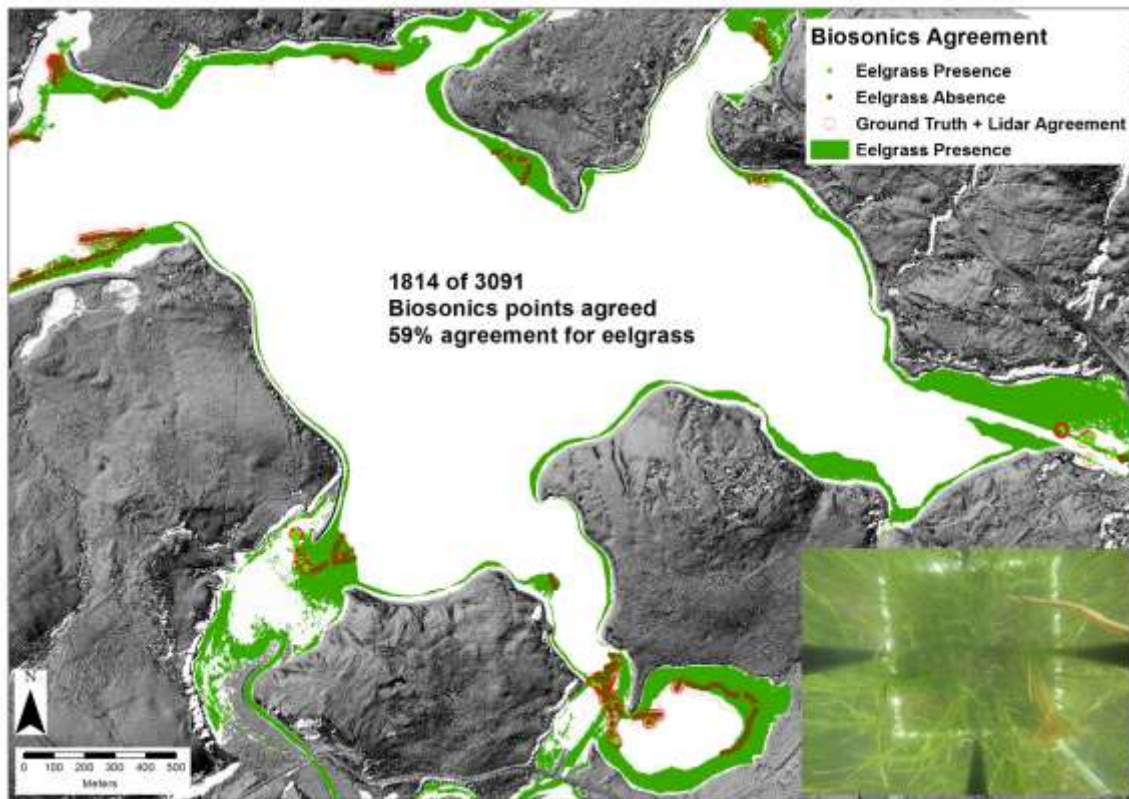


Figure 3.34: Correlation between eelgrass presence and DFO Biosonics results in Eastern Mabou Harbour.

3.5.2 Bottom Classification Maps

The preliminary bottom classification map produced for PWRP shows separate classes for eelgrass, sand/mud, and seaweed/rocks (Figure 3.35). The study area was 34% eelgrass, 62% sand/mud, and 4% rock/seaweed.

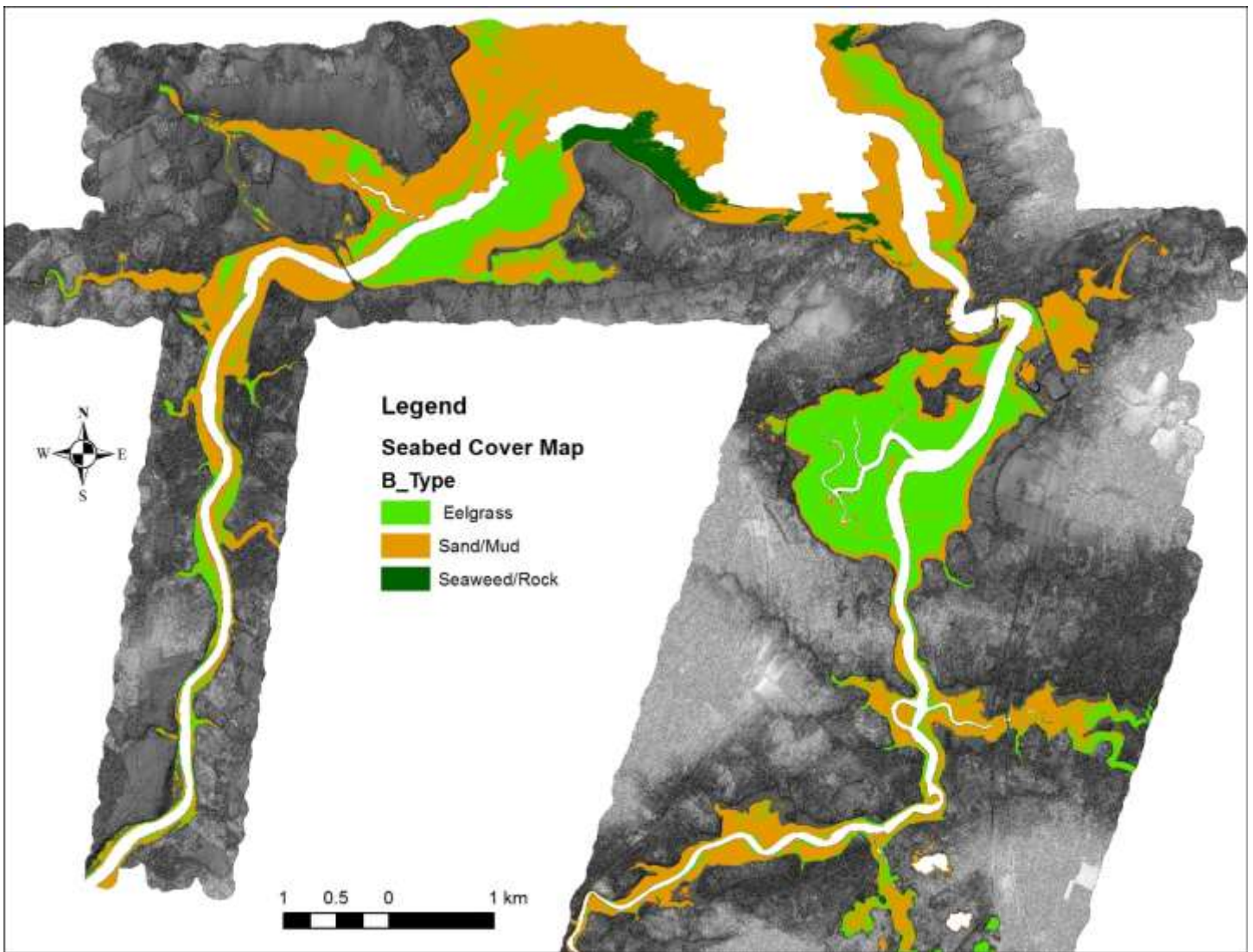


Figure 3.35: Seabed Cover Classification for PWRP showing the entire study area (top) and cropped to an area near the mouth of River Philip (lower panels).

4 Hydrodynamic Modelling

High-resolution 2-D hydrodynamic (HD) models were developed using the DHI Mike-21™ software module to simulate current flow and water level variations within the each study area. For each study area, the model domains were designed to be much larger than the lidar study area in order to properly model the circulation in the region through the Northumberland Strait into the inner harbours. Model inputs included bathymetry and boundaries, described in the following sections.

4.1 Modelling Methods

4.1.1 Grid Preparation

A variety of sources and resolutions of topography and bathymetry were required in order to complete the model depth grids (Table 4.1, Figure 4.1). Topo-bathymetric lidar data from 2014 (Little Harbour) and 2016 (Pictou Harbour in addition to the three study areas of this report) were re-sampled from 1 m to 9 m for computational efficiency. Other bathymetric data included a digital compilation of bathymetry data from various sources (e.g. multibeam, single beam, seismic, etc.) aggregated by CHS (Varma et al., 2008) near 5 m resolution at best, single beam echo soundings collected by AGRG in 2009 using a Humminbird echo sounder, single beam echo sounding data collected by DFO project partners for Mabou using a BioSonics instrument, and 5 m multibeam data for Merigomish Harbour and approach. A 20 m resolution database from the Nova Scotia Dept. of Natural Resources was used for the NS topography not included in the lidar dataset, and topographic lidar data collected by AGRG for PEI was used for the PEI coastline.

Provider	Source	Study Area	Native Resolution	Domain
AGRG	Lidar: Pictou Harbour, Merigomish Harbour, Little Harbour, Mabou Harbour, Pugwash Harbour and River Philip	All	2 m	Topo/Bathy
CHS	Multibeam	MERI	5 m	Bathy
CHS	Variable (Echo soundings, digitized paper charts, etc.)	ALL	Variable	Bathy
DFO, AGRG	Single Beam Echo Soundings (BioSonics, Humminbird)	PWRP, MABOU	Variable (< 5 m)	Bathy
AGRG	RiverRay ADCP	PWRP	1 m	Bathy
AGRG	Lidar: PEI	MERI	2 m	Topo
NSDNR	Rasterized 1:10 000 Contour Data	ALL	20 m	Topo

Table 4.1: HD model bathymetric data sources, resolution, domain and number of observations. NSDNR: Nova Scotia Department of Natural Resources.

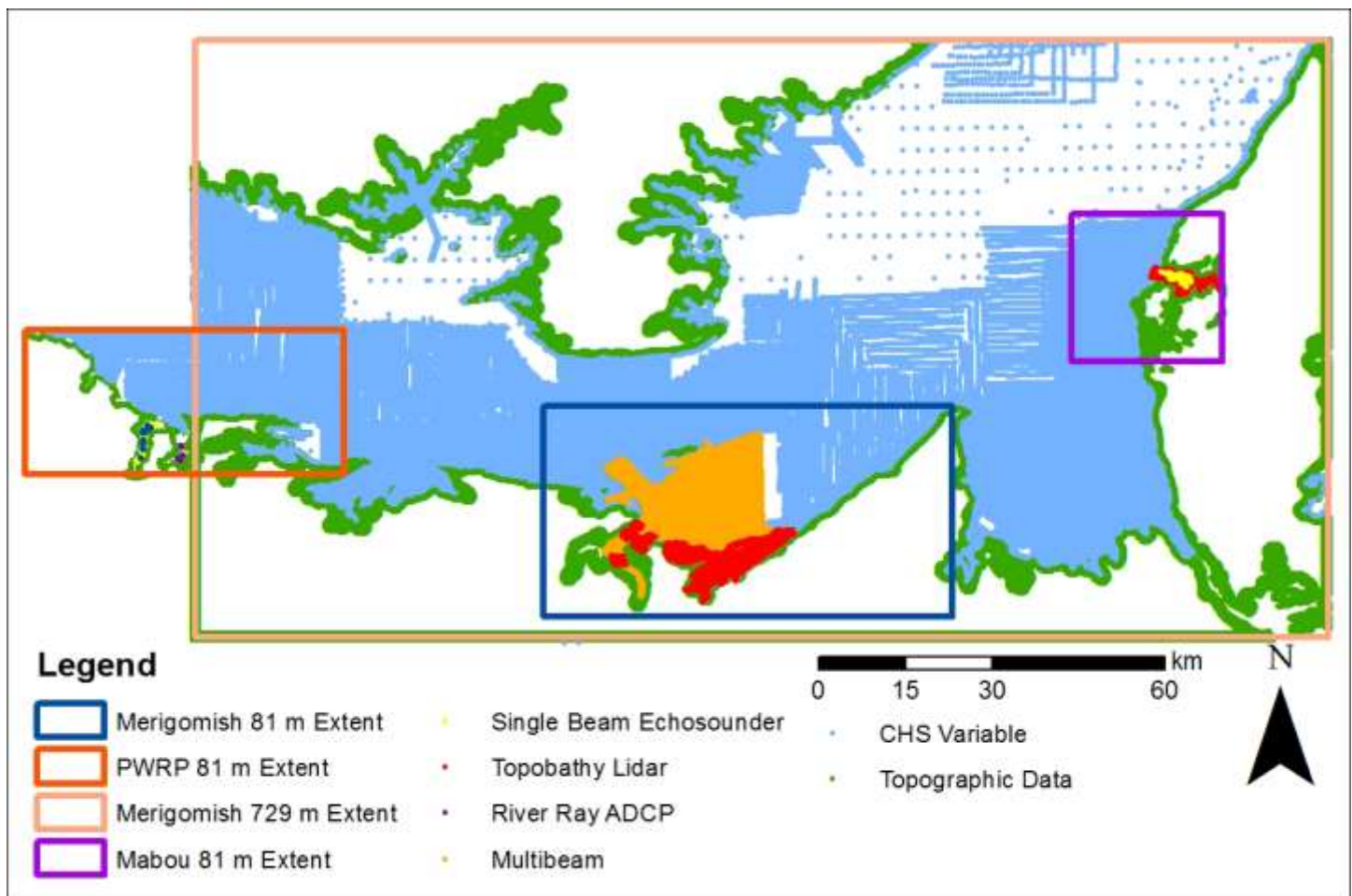


Figure 4.1: Sources of model topographic and bathymetric data.

A nested grid model approach was used to reduce the calculations required by the models. Merigomish was the first study area to be modelled, and a five-grid system was generated to be used there based on the results of a single-grid model. However, as will be discussed later in the report, the five-grid system did not improve model results noticeably over the single grid-approach; therefore, more computationally efficient three-grid systems were developed for PWRP and Mabou. Each nest used a 3:1 resolution step (Figure 4.2, Figure 4.4, Figure 4.6). To generate each grid, the bathymetry and topography datasets were subject to rigorous quality control procedures to ensure continuity between the various data sources, were clipped to remove overlapping data points, giving preference to the higher resolution dataset, and topography datasets were clipped to the coastline to reduce dataset size. The lowest resolution grids (Merigomish Domains 4 and 5) were generated using only the coastal topographic data points and the CHS database bathymetry points, and were interpolated into rasters at their required resolutions (243 m and 729 m) using the ArcMap *Topo to Raster* tool to fill gaps in the different resolution datasets. The interpolation technique ensured a smooth elevation surface despite the coarse and irregular point spacing of the different datasets. All of the datasets (lidar, multibeam, topo points, etc.) were used to generate 9 m resolution datasets to fit each Domain 3; this was resampled and clipped to make the remaining model domains (Figure 4.3, Figure 4.5, Figure 4.7). Once the datasets were imported into the modelling software, additional minor bathymetry edits were made.

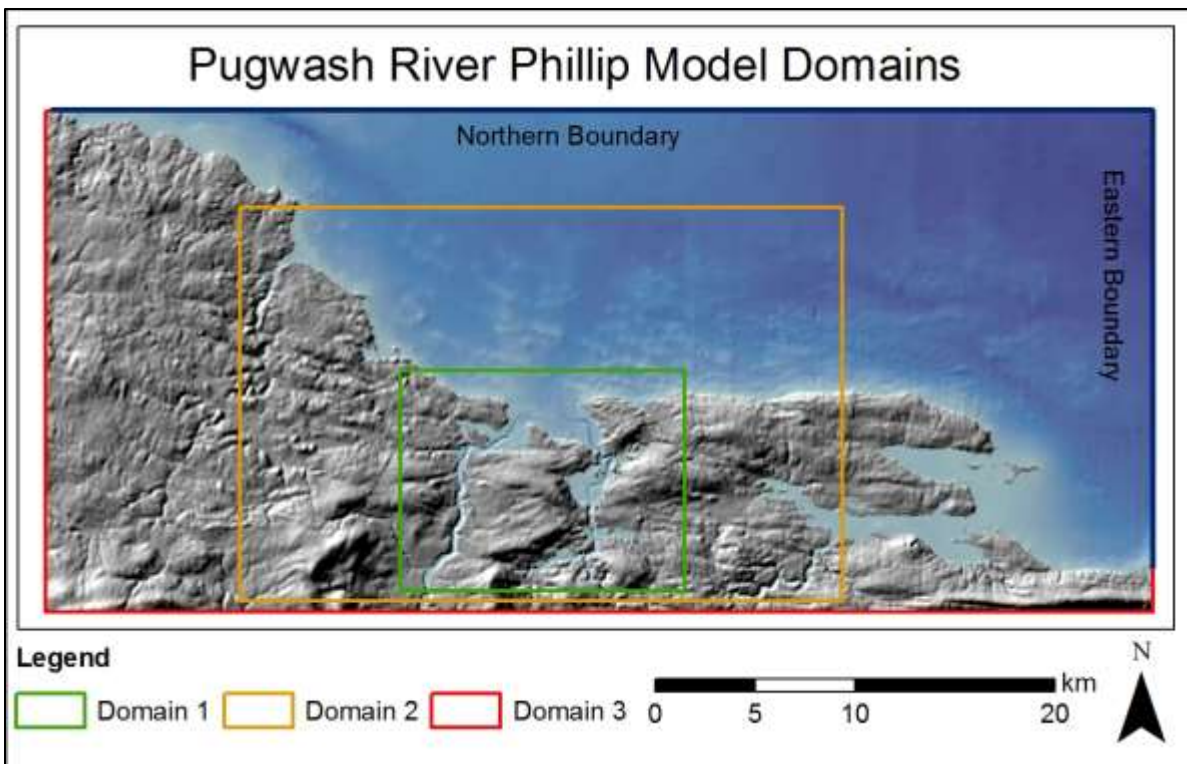


Figure 4.2: Mike 21 hydrodynamic model domain extents for PWRP showing boundaries, and Domain 3 grid draped over a 5x hillshade.

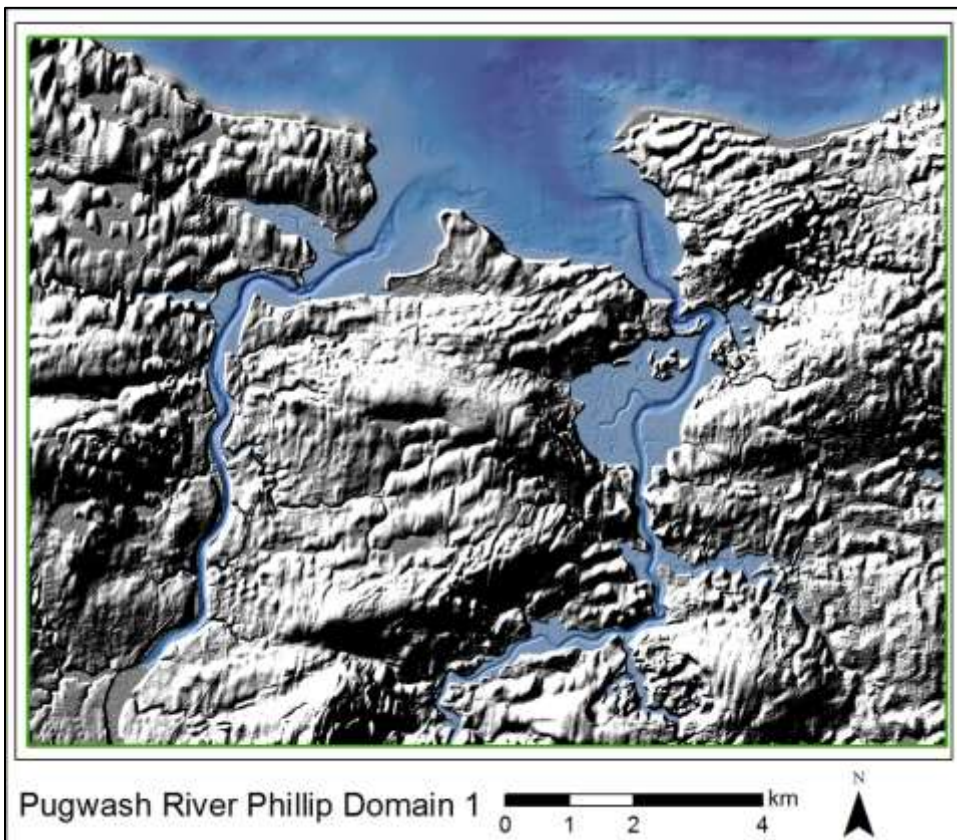


Figure 4.3: PWRP Domain 1: 9 m model grid draped over a 5x hillshade.

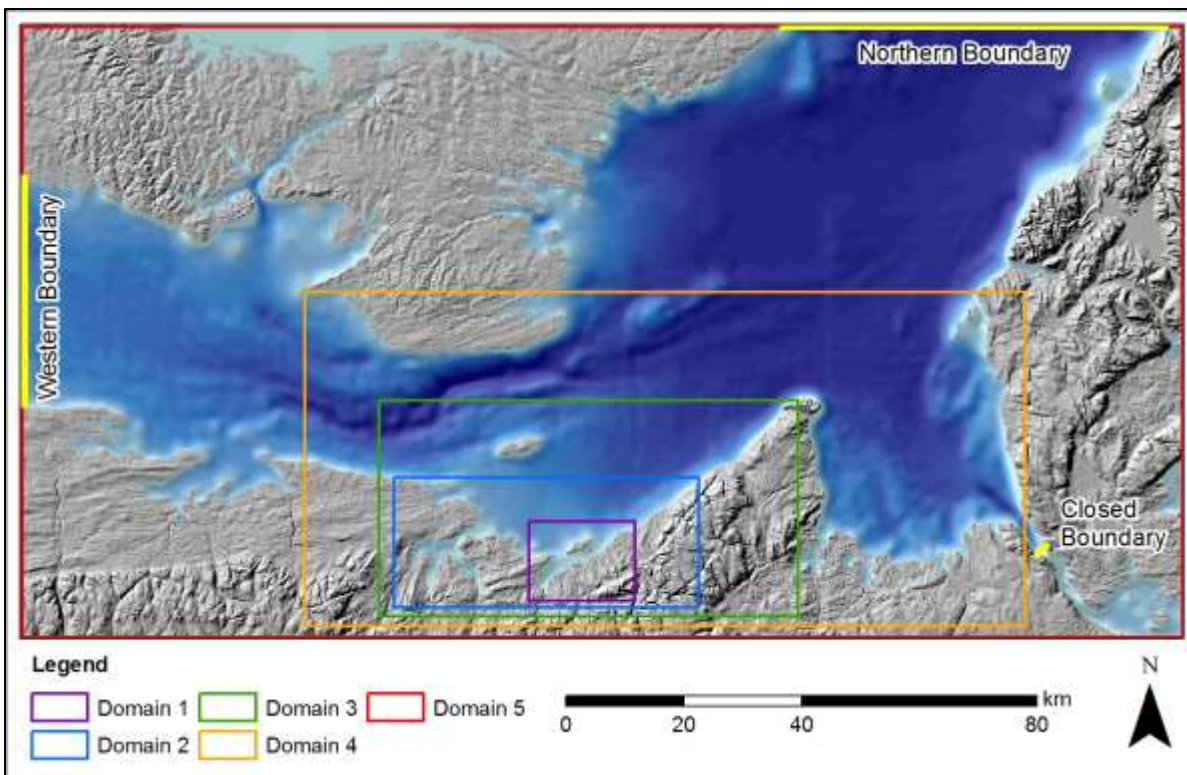


Figure 4.4: Mike 21 hydrodynamic model domain extents for Merigomish showing boundaries, and Domain 5 grid draped over a 5x hillshade.

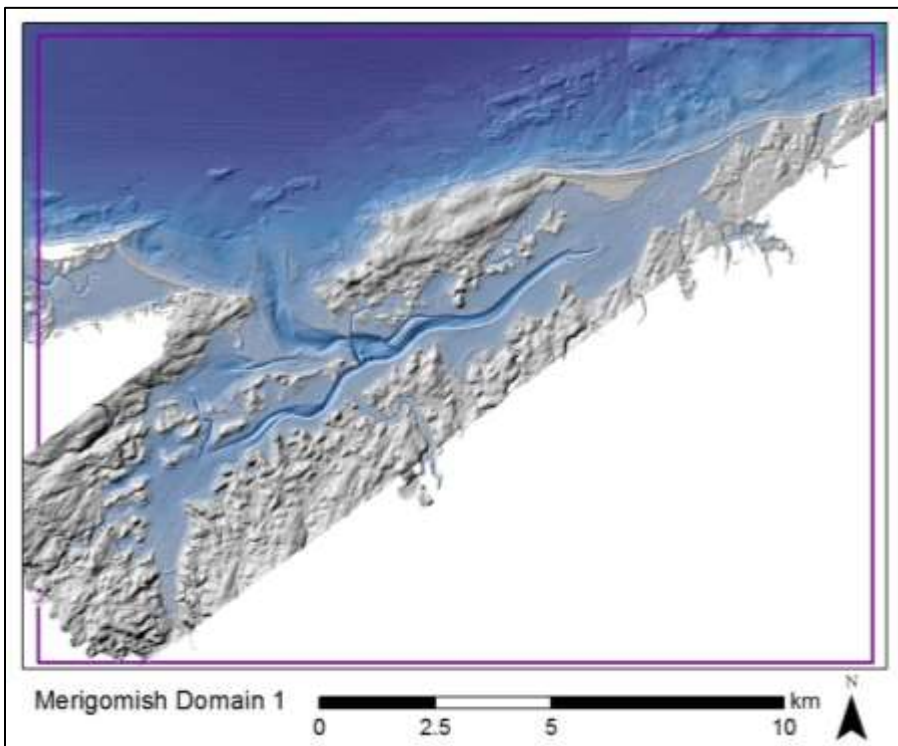


Figure 4.5: Merigomish Domain 1: 9 m model grid draped over a 5x hillshade. The topographic lidar is draped over the modelled topography, which was clipped more closely to the coast.

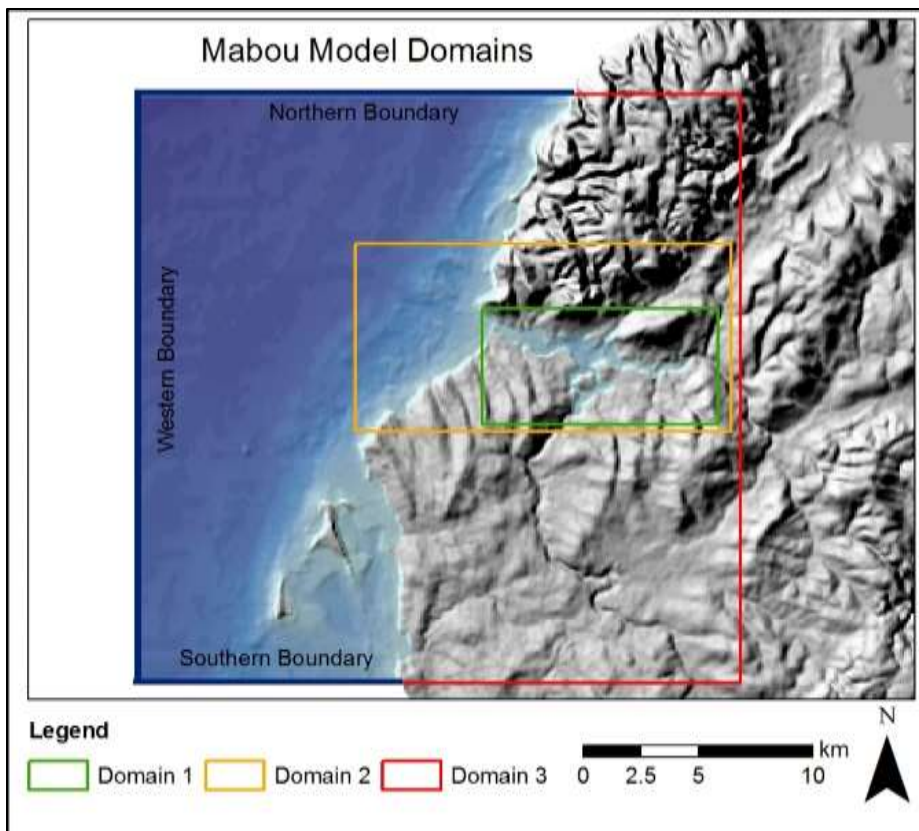


Figure 4.6: Mike 21 hydrodynamic model domain extents for Mabou showing boundaries, and Domain 3 grid draped over a 5x hillshade.

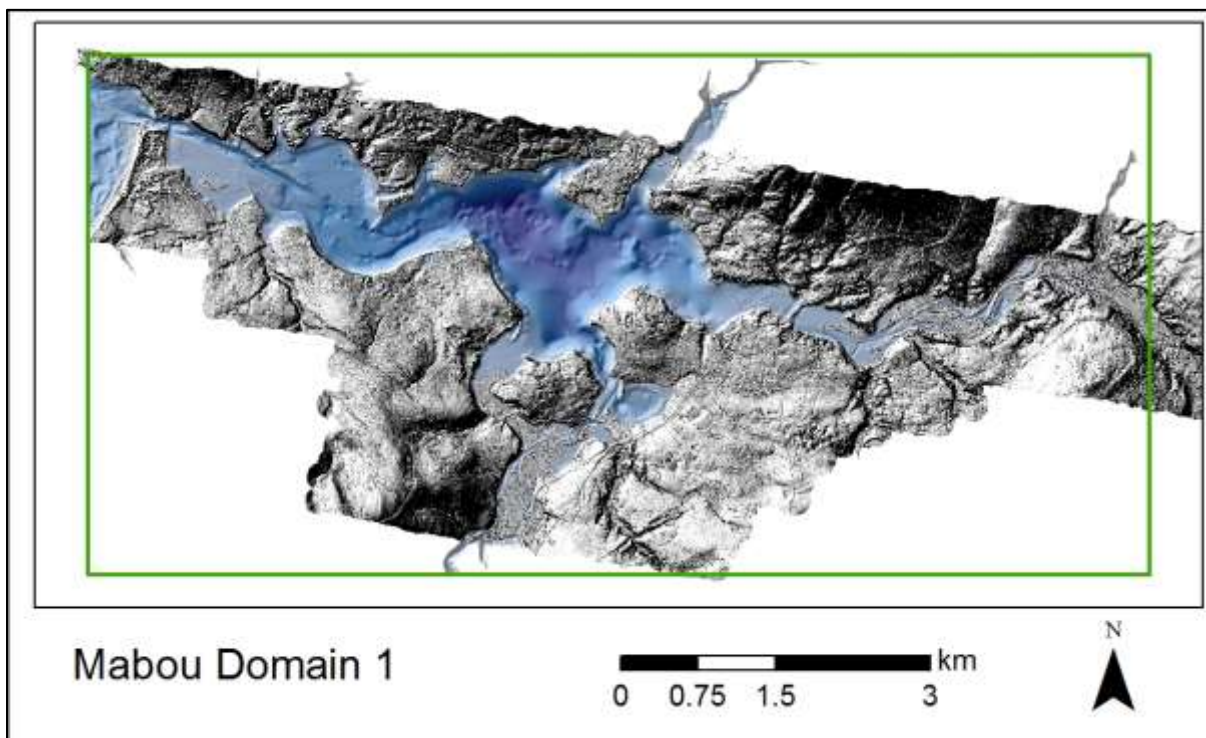


Figure 4.7: Merigomish Domain 1: 9 m model grid draped over a 5x hillshade. The topographic lidar is draped over the modelled topography, which was clipped more closely to the coast.

4.1.2 Boundary Conditions

Each model simulated water level variations over the interpolated bathymetry surface in response to a forcing tidal boundary condition at two different locations, noted in the figures above. All of the boundaries were forced with predicted tidal elevations at 5-minute resolution extracted from WebTide (Dupont et al., 2005).

At PWRP tidal elevations across the Northern Boundary varied by 0.05 m and at the Eastern Boundary elevations across the boundary varied by at most 0.03 m (Figure 4.8).

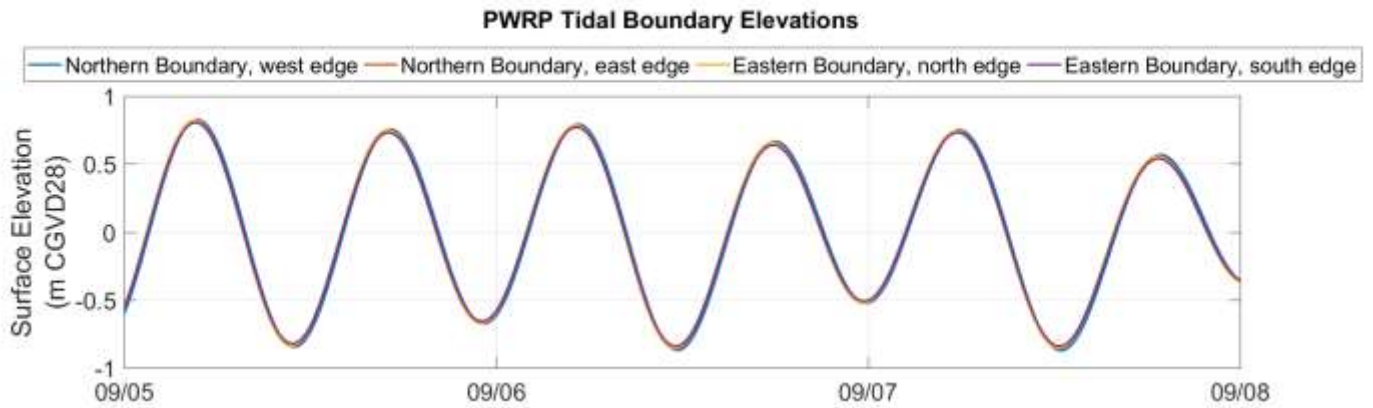


Figure 4.8: Tidal elevations predicted for the duration of the PWRP model simulation across the boundaries.

At Merigomish, tidal elevations across the Western Boundary varied between 0.01 m and 0.05 m and at the Northern boundary elevations across the boundary varied by as much as 0.15 m. The Canso Causeway represented a closed boundary; data south of the causeway were not included in the model domain (Figure 4.9).

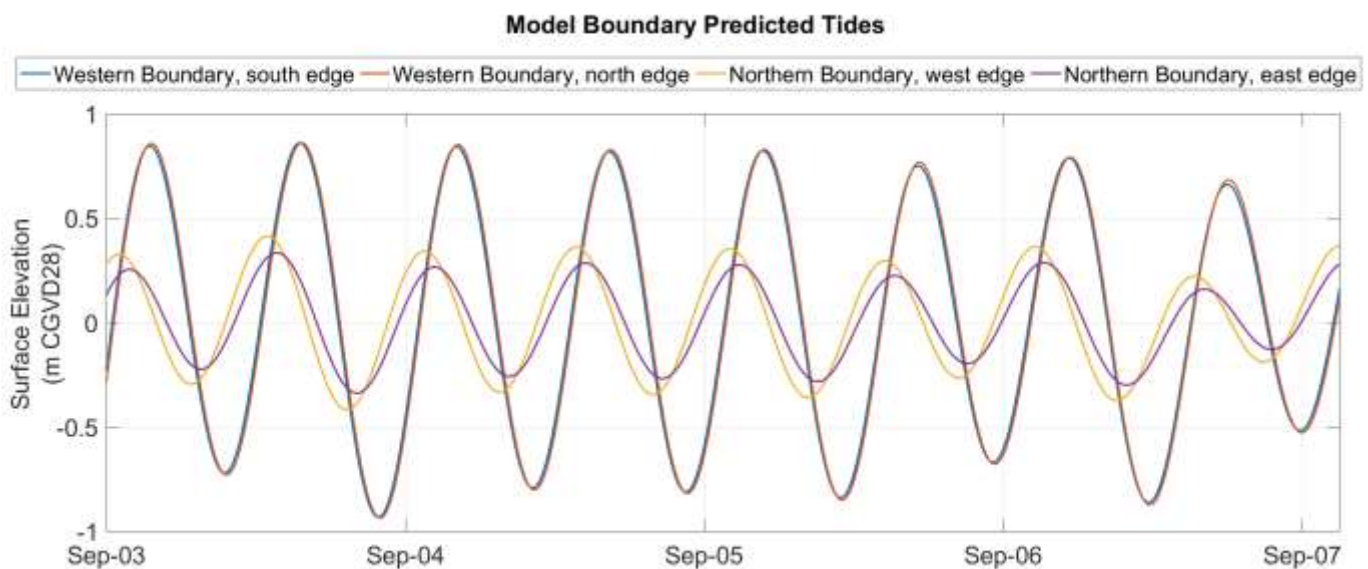


Figure 4.9: Tidal elevations predicted for the duration of the Merigomish model simulation across the boundaries.

At Mabou tidal elevations across the Southern Boundary varied less than 0.02 m; across the Western Boundary up to 0.04 m, and across the Northern Boundary by 0.06 m at most (Figure 4.10). The Mull River was represented by a point source with flow = 9.4 m³/s and velocity = 0.1 m/s, values based on observations made in the field on a falling High Tide using the RiverRay ADCP.

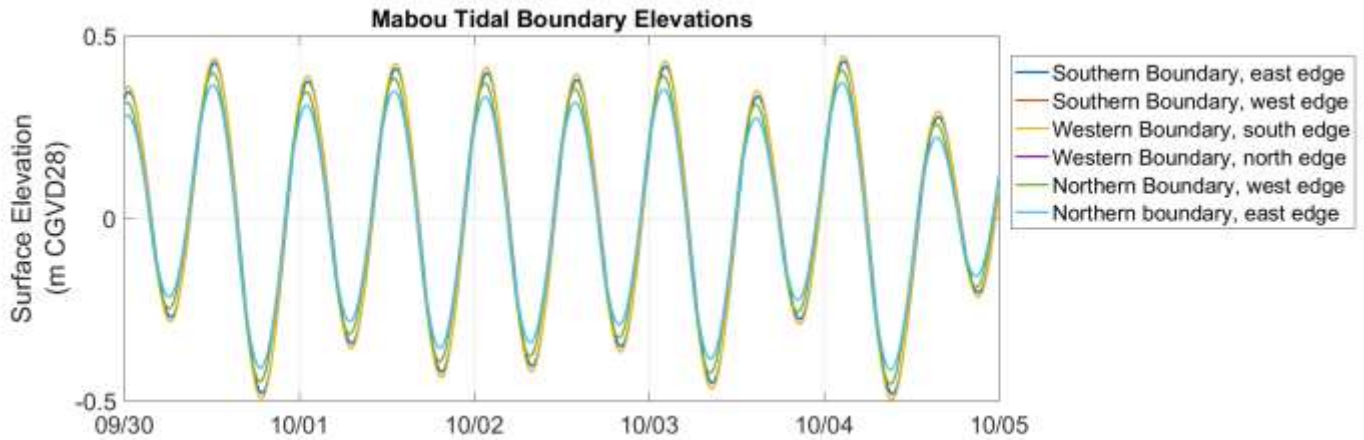


Figure 4.10: Tidal elevations predicted for the duration of the Mabou model simulation across the boundaries.

4.1.3 Model Parameters and Calibration

Parameters used in each model simulation are reported in Table 4.2. The model simulation start times were chosen to overlap with observed currents and surface elevation, and to coincide with a high tide, for model stability. Model parameters were optimized during the calibration process by comparing model results to ADCP observations. The timestep (Δt) was chosen in order to minimize the Courant number, C , which was calculated based on

$$C = \sqrt{g \times z_{max}} \times \frac{\Delta t}{\Delta x}$$

where z_{max} is the maximum depth for each model grid, g is gravity, and Δx is the model resolution. For PWRP and Merigomish a grid-dependent, velocity-based eddy viscosity scheme produced the best results. A constant eddy viscosity value, E , was chosen for each model domain such that

$$\frac{E \times \Delta t}{\Delta x^2} \leq 0.5$$

For Mabou a time-varying function of the local gradients in the velocity field, the Smagorinsky scheme, was employed as it captured the small-scale complex nature of the currents observed there. The Smagorinsky factor, C_s , required to be in the interval of 0.25 and 1, was chosen based on a best-fit model solution. Initially, the bed resistance value for each model was varied between a constant Manning's M of 32 m^{1/3}/2 and 48 m^{1/3}/2. To improve model fit, a spatially varying bed resistance maps was used for each study area. PWRP and Merigomish were insensitive to changes in the bed resistance,

and were not improved by the spatially varying map; the constant value of $32 \text{ m}^{1/3}/2$ was ultimately chosen. At Mabou, the spatially varying bed resistance map produced the best model results. The orthophotos and bathymetry were used to identify sandy and vegetated areas, which were assigned high (75) and low (25) Manning's numbers; the remainder of the values fell somewhere in this range. Initial surface elevation values were extracted from the boundary condition, and represent the tidal stage at the start of the simulation. Flooding and drying depth were lowered at Merigomish to better simulate flow in the shallow eastern portion of the harbour, where a water level sensor was located; the other models were insensitive to the flooding and drying depth and were left at default values. Wind was added to the model simulations but the model results proved insensitive to adding the wind, perhaps as there were no major wind events during the modelled time period, and the wind was removed in the interest of computational efficiency. Effects of waves were not modelled at this time.

Study Area	Domain	Timestep (s) Δt	Resolution (m) Δx	Model Simulation Period	Courant Number	Eddy Scheme and E/C _s	Resistance ($\text{m}^{1/3}/2$ Manning's M)	Initial surface elevation (m)	Drying Depth (m)	Flooding Depth (m)
PWRP	1	3	9	Sept. 5 5:00 AM – Sept. 7 5:00 AM	3.51	Constant, velocity-based; E = 0.1	32	0.8	0.1	0.2
	2		27		1.47					
	3		81		0.56					
MERI	1	3	9	Sept. 17 2:00 AM – Sept. 24 2:00 AM	4.72	Constant, velocity-based; E = 0.02	32	0.7	0.01	0.02
	2		27		1.88					
	3		81		0.88					
	4		243		0.33					
	5		729		0.11					
MAB	1	2	9	Sept. 30 1:00 PM – Oct. 5, 12:00 AM	2.84	Smagorinsky; C _s = 0.5	Spatially varying	0.4	0.1	0.2
	2		27		1.56					
	3		81		0.59					

Table 4.2: Model Parameters for each study area.

4.2 Modelling Validation and Results

4.2.1 Pugwash-River Philip

The modelled and observed surface elevation and north-south currents at PWRP agreed well in amplitude and in phase, but the model underestimated the direction of flow by approximately 50° and the east-west currents by approximately 0.1 m/s (Figure 4.11). A sand bar or area of elevated bathymetry (~2.5 m depth) near the ADCP (deployed at ~3.5 m depth, location shown on Figure 2.4) appeared to have played a role in the underestimated current amplitude and direction; model results from a grid cell on the river side of the sand bar matched the ADCP observations exactly. The ADCP suggests that during the ebb tide water flowed over the sand bar and towards the east, but the model simulated flow directly north over the sandbar. Adjustments to the bed resistance did not improve results significantly. Refinement of model bathymetry in the area east of the ADCP with multibeam echosounder data from CHS may have improved the accuracy of the water movement downstream of the ADCP in the east-west direction. The depth-averaged flow at PWRP was a good representation of flow at all depths (Figure 4.12).

The two-dimensional results show the flow approaching Pugwash Harbour on the flood tide initially from the northwest, then rotating to flow from the northeast; the flow then enters River Philip and Pugwash River and flows upstream, flooding the dry mudflats along the riverbanks (Figure 4.13, Figure 4.14). The river flats drain on the ebb tide and flow leaves the estuary flowing north, and then turning to the northeast once it enters the deeper portion of the Northumberland Strait (Figure 4.14). Plotting current speed as the contour plot instead of water depth in Figure 4.15 shows how the current changes on either side of the sandbar, which appears in the figure as the area just south of the ADCP (red diamond) where the current speed goes from blue to green. Just south of the sandbar the current vectors turn sharply to the west on the flood tide, and sharply to the east on the ebb tide, following the deeper water there, while modelled current speed at the ADCP is weaker and more northerly. The observations at the ADCP suggest that the flow at the ADCP should be more similar to the modelled flow behind the sandbar.

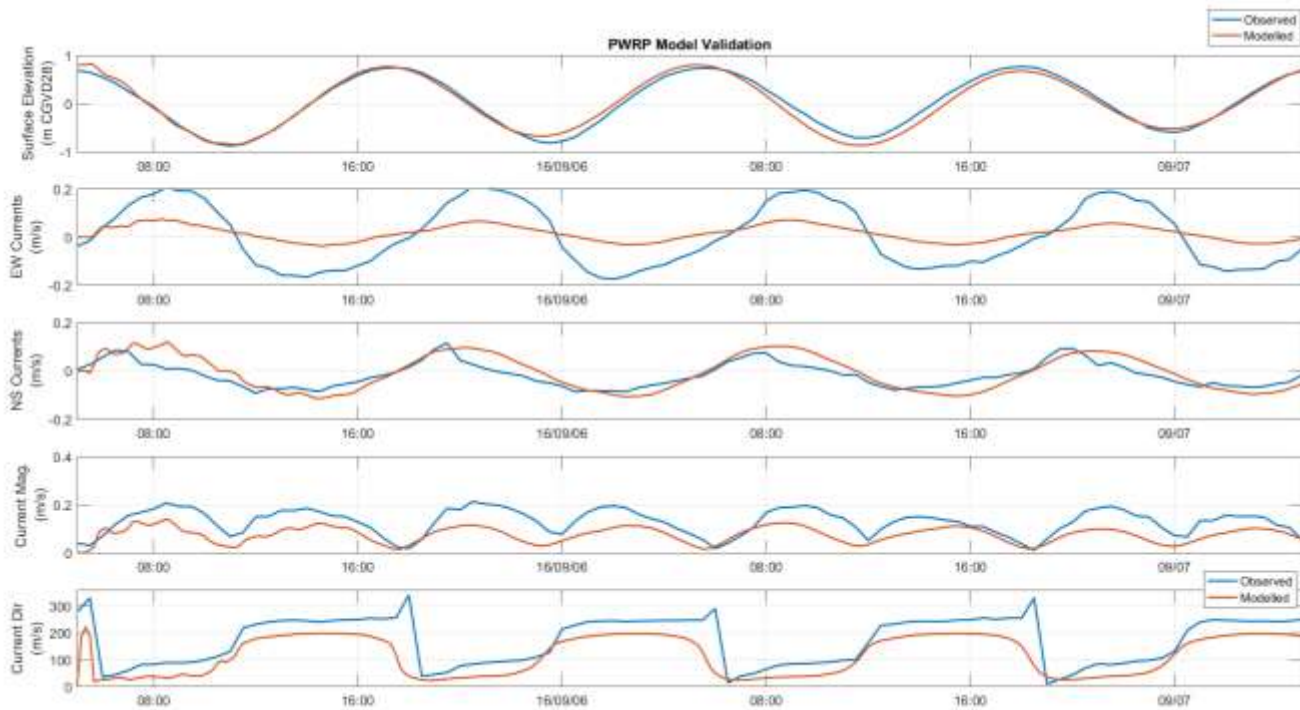


Figure 4.11: PWRP modelled and observed surface elevation and currents. Panels, from top to bottom: surface elevation; east-west current; north-south current; current speed; current direction.

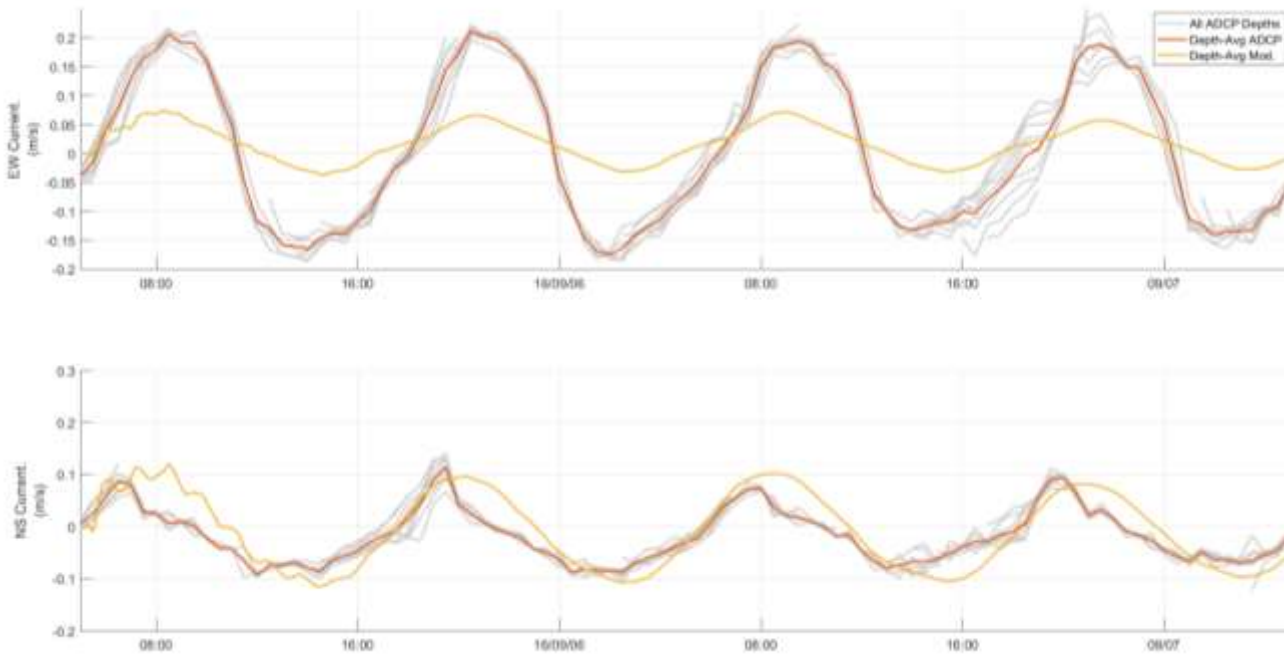


Figure 4.12: Comparison of PWRP depth-averaged currents to currents observed by the ADCP at all depths.

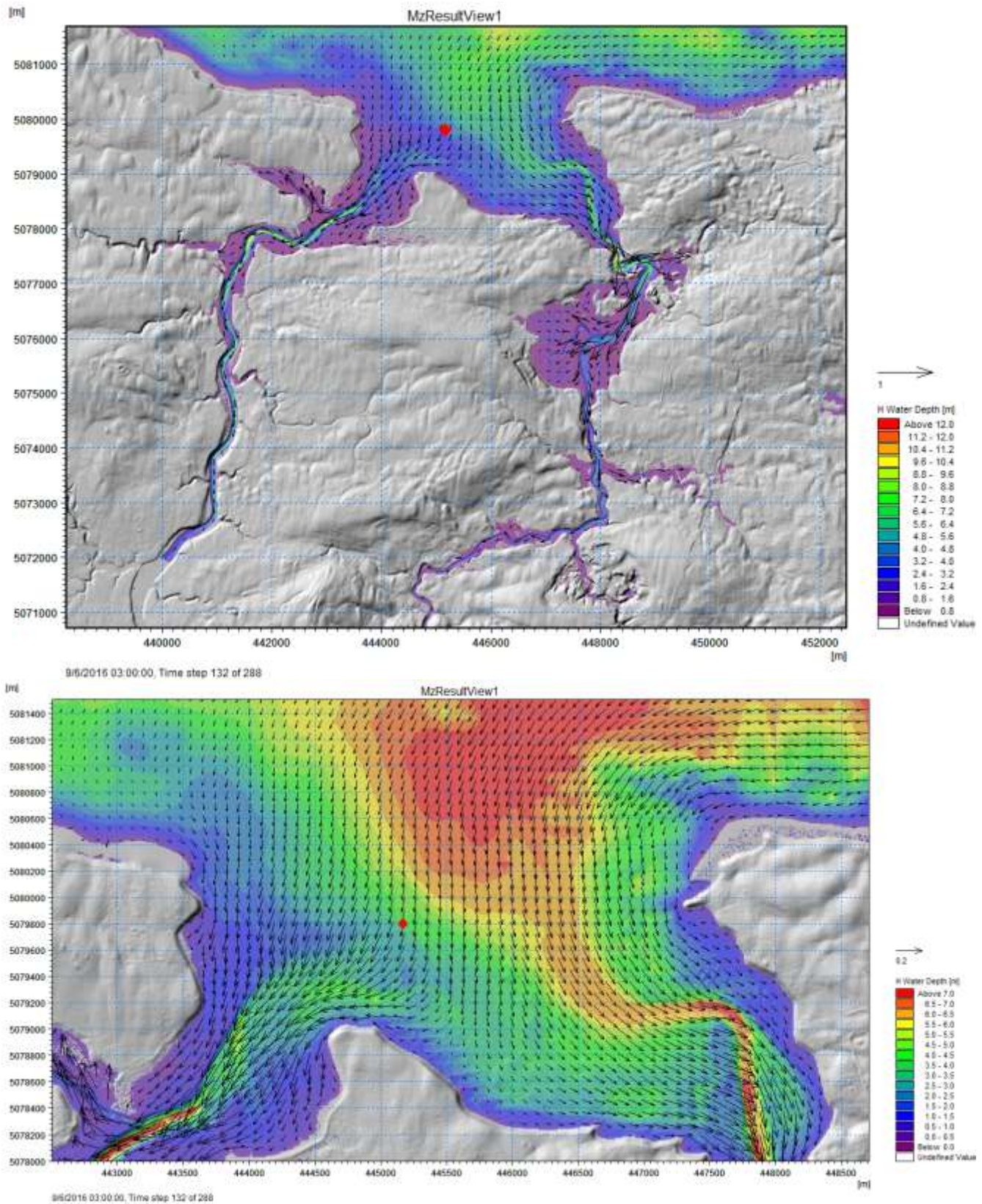


Figure 4.13: PWRP model results for (top) domain 1, and (bottom) cropped to an area near the ADCP during maximum flood tide on Sept. 6 at 3:00. The contour map is water depth and the vectors represent current speed and direction.

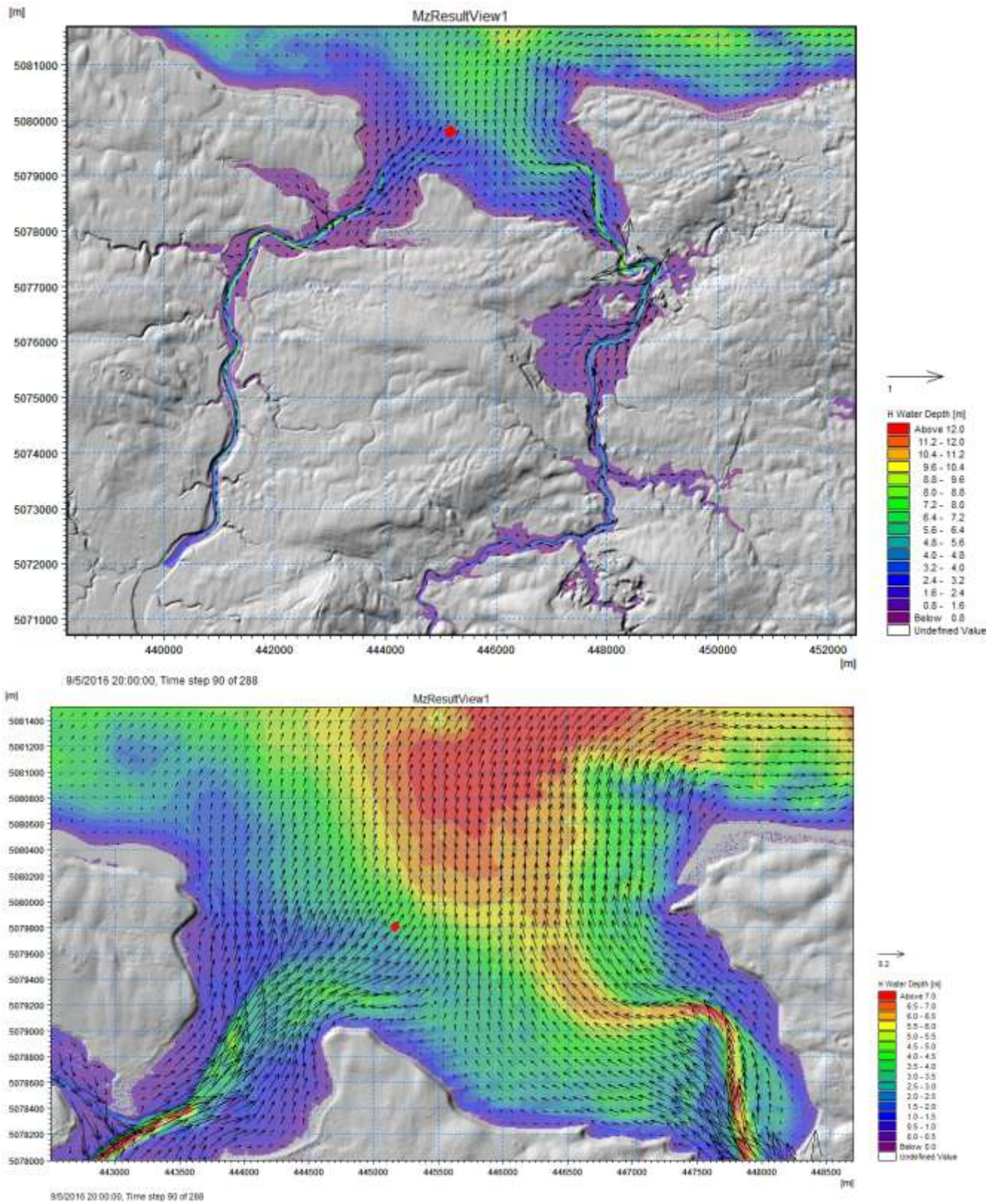


Figure 4.14: PWRP model results for (top) domain 1, and (bottom) cropped to an area near the ADCP during maximum ebb tide on Sept. 5 at 20:00. The contour map is water depth and the vectors represent current speed and direction.

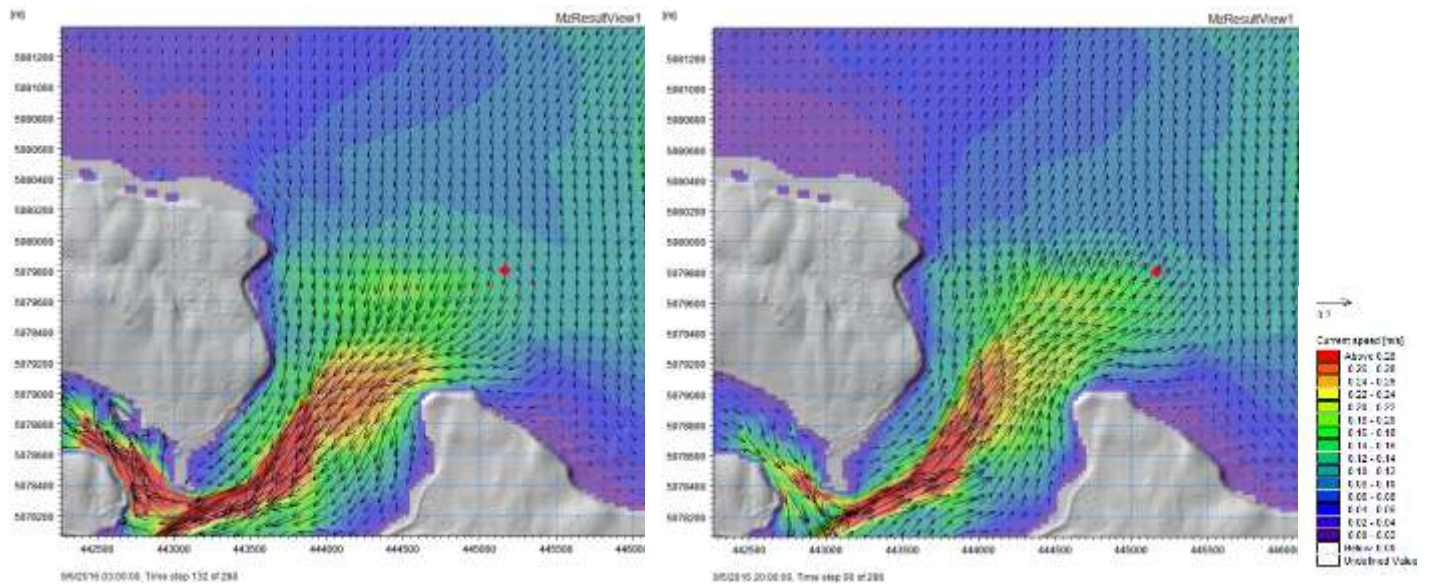


Figure 4.15: Current vectors at (left) flood tide and (right) ebb tide draped over a contour plot of current speed.

4.2.2 Merigomish

The model was successful at simulating tidal flow in and out of Merigomish Harbour. The water level sensors deployed in the fall by DFO were used for model surface elevation validation, and the ADCP deployed by DFO was used for current validation (Figure 4.16) (the ADCP’s pressure sensor malfunctioned and so no pressure record was available from the ADCP for model validation). Surface elevation was well-modelled at MGH1 and MGH3, but the modelled water depth at MGH4 caused it to be classified as a ‘dry cell’ on low tides (Figure 4.17).

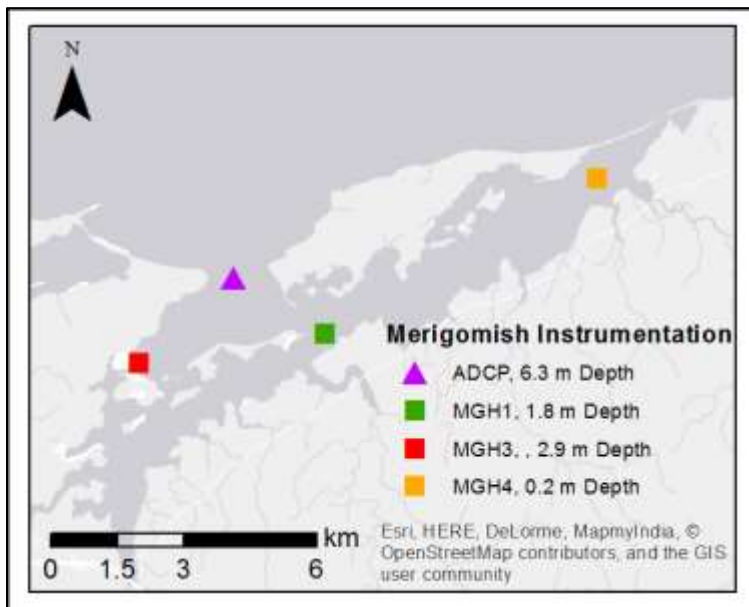


Figure 4.16: Merigomish instrumentation by DFO: one ADCP and three Hobo water level sensors; also displayed is the mean modelled depth.

The data show that NS currents were well-modelled, but there was a 40° offset in current direction on the ebb tide, such that the model simulated flow leaving the mouth of the harbour at ~350°, e.g., along the axis of the harbour mouth, the ADCP recorded water on the ebb flow passing over the ADCP at a direction of ~30°, moving more towards the east (Figure 4.18). That difference in modelled and observed direction is evident in the mismatch between modelled and simulated east-west current. The ADCP shows that the flood tide is typically 0.2 m/s slower than the ebb tide, but this difference varies with the nature of the tidal cycle; the model simulated the amplitude of the flood tide consistently well, but did not model the difference in amplitude between ebb and flood tide.

It is possible that the model was unable to simulate fine-scale and complex current patterns at the site of the ADCP near the edge of the channel leaving Merigomish Harbour. Model parameters were varied in an attempt to improve the simulation of flow at the ADCP, a large nested grid system was employed to better simulate the flow outside of the harbour, a spatially varying bed resistance map was developed but did not improve model results, the eddy viscosity scheme was varied, and numerous other adjustments were made; to no avail. Despite this small discrepancy in modelled direction, the overall circulation of water throughout Merigomish Harbour appeared realistic and the surface elevation was well matched throughout the model domain, the model was considered overall successful.

The two-dimensional model shows water flowing towards Merigomish Harbour on a flood tide from the northeast, entering Merigomish Harbour and splitting to fill each side of the estuary with water, while flow outside the harbour is towards the east (Figure 4.20). The flow leaves the harbour on the ebb tide, flowing north through the center of the channel, northeast on the east side and northwest on the western side; the flow outside the harbour is easterly during the ebb tide (Figure 4.21). A closer inspection of EW current in the channel shows the modelled current flowing northwest on the ebb tide and southeast on the flood tide (Figure 4.22). The ADCP observations showed the ebb tide flowing over the ADCP moving northeast, and southwest on the flood. Figure 4.22 shows that the current flows in EW direction over the ADCP but flows in the EW opposite direction only a few cells away, suggesting that the flow in the channel is complex, and that even a small error in the GPS coordinates of the ADCP, or a shift in its location, could account for the errors in modelled EW current.

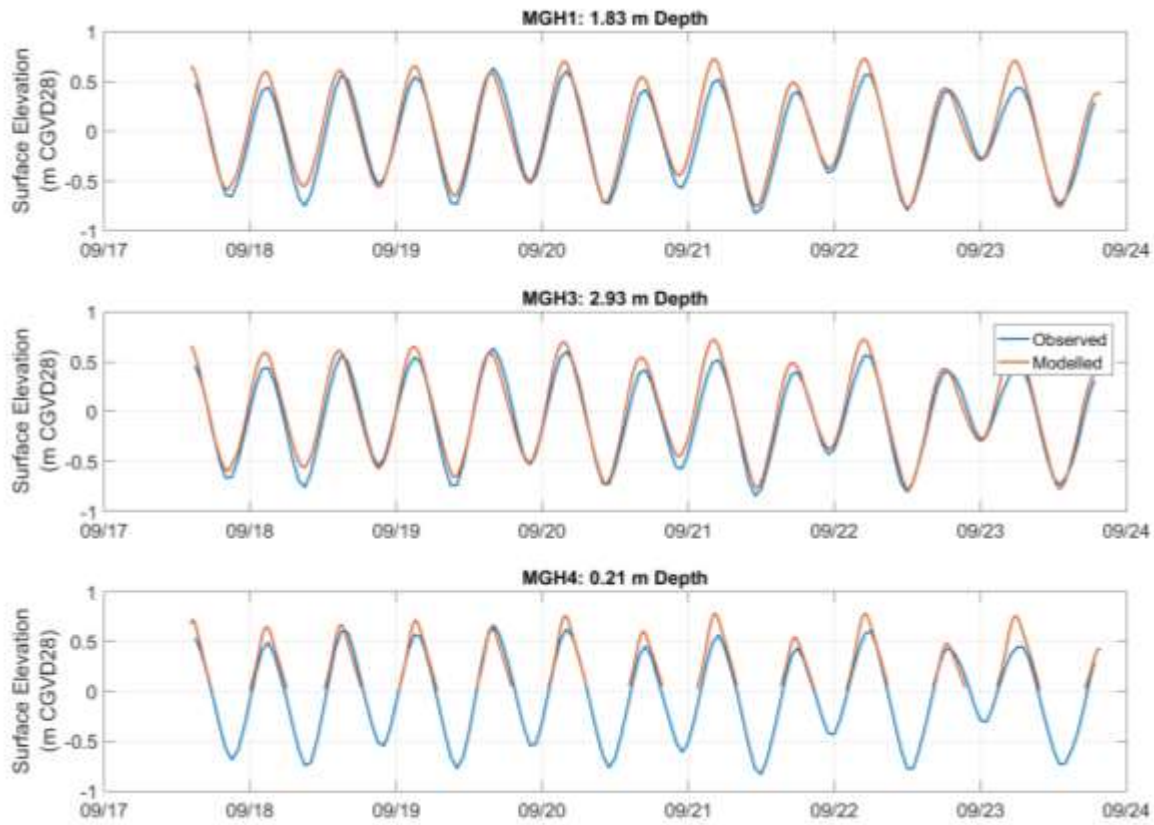


Figure 4.17: Merigomish modelled and observed surface elevations.

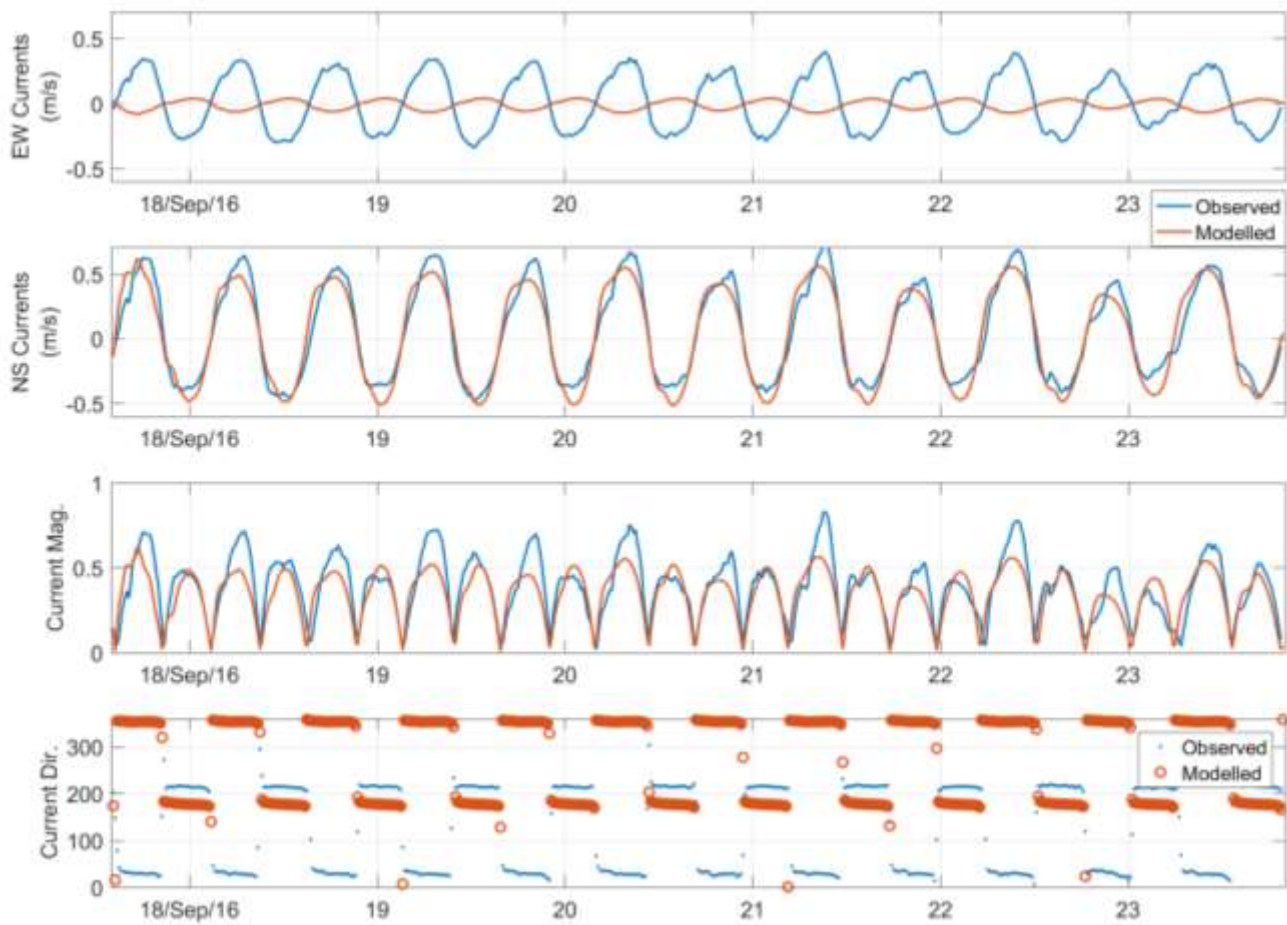


Figure 4.18: Merigomish modelled and observed ADCP currents. Panels, from top to bottom: east-west current; north-south current; current speed; current direction.

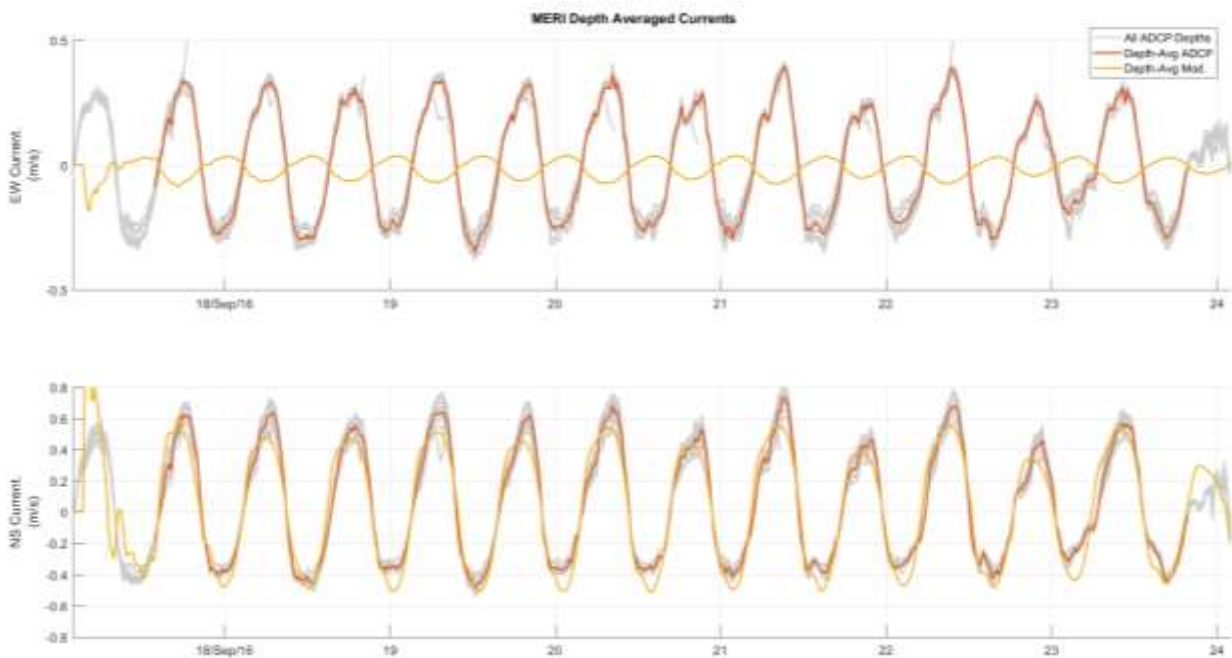


Figure 4.19: Comparison of Merigomish depth-averaged currents to currents observed by the ADCP at all depths

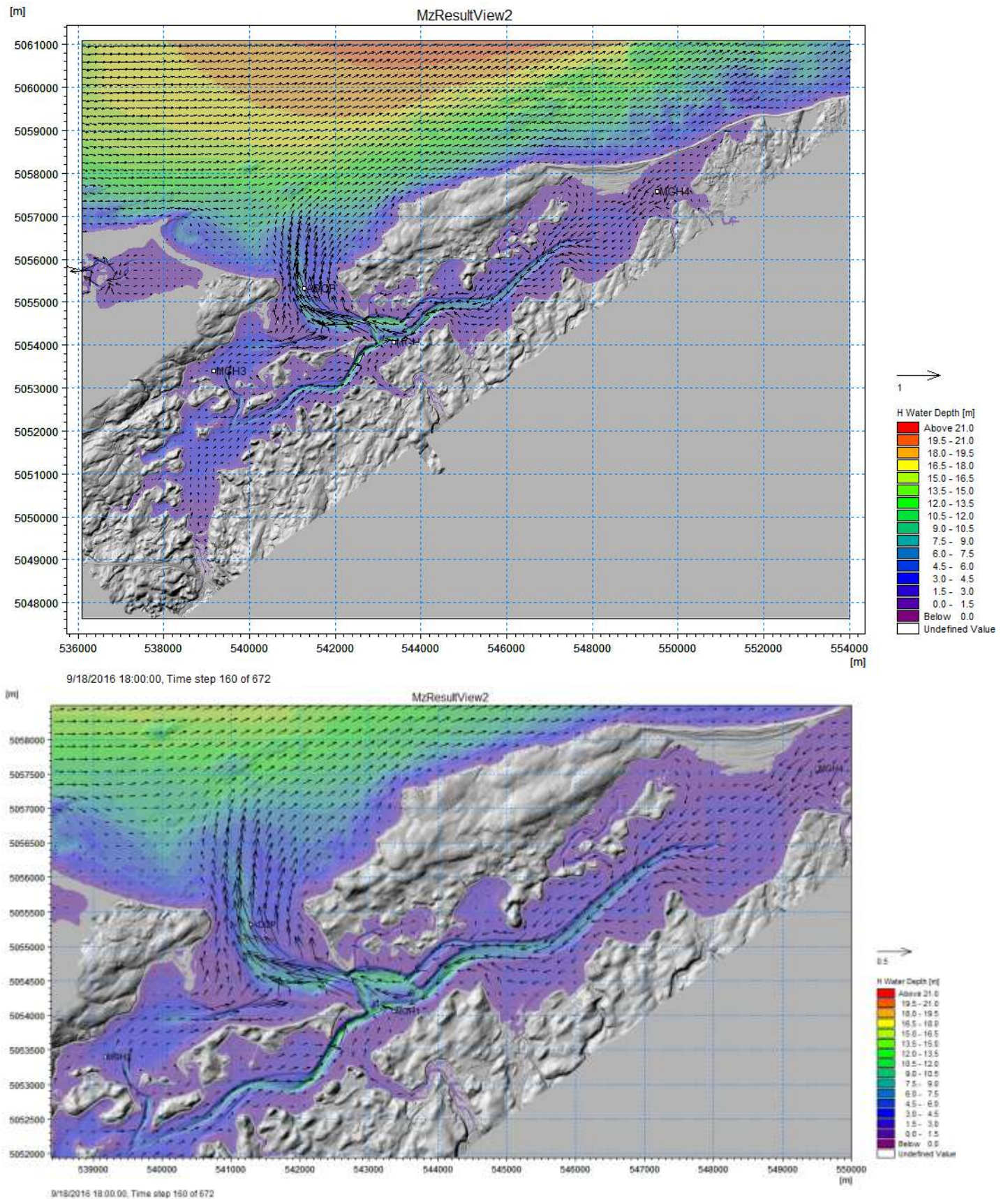


Figure 4.20: Merigomish model results for (top) Domain 1, and (bottom) cropped to an area near the ADCP and water level sensors during maximum ebb tide on Sept. 18 at 18:00. The contour map is water depth and the vectors represent current speed and direction.

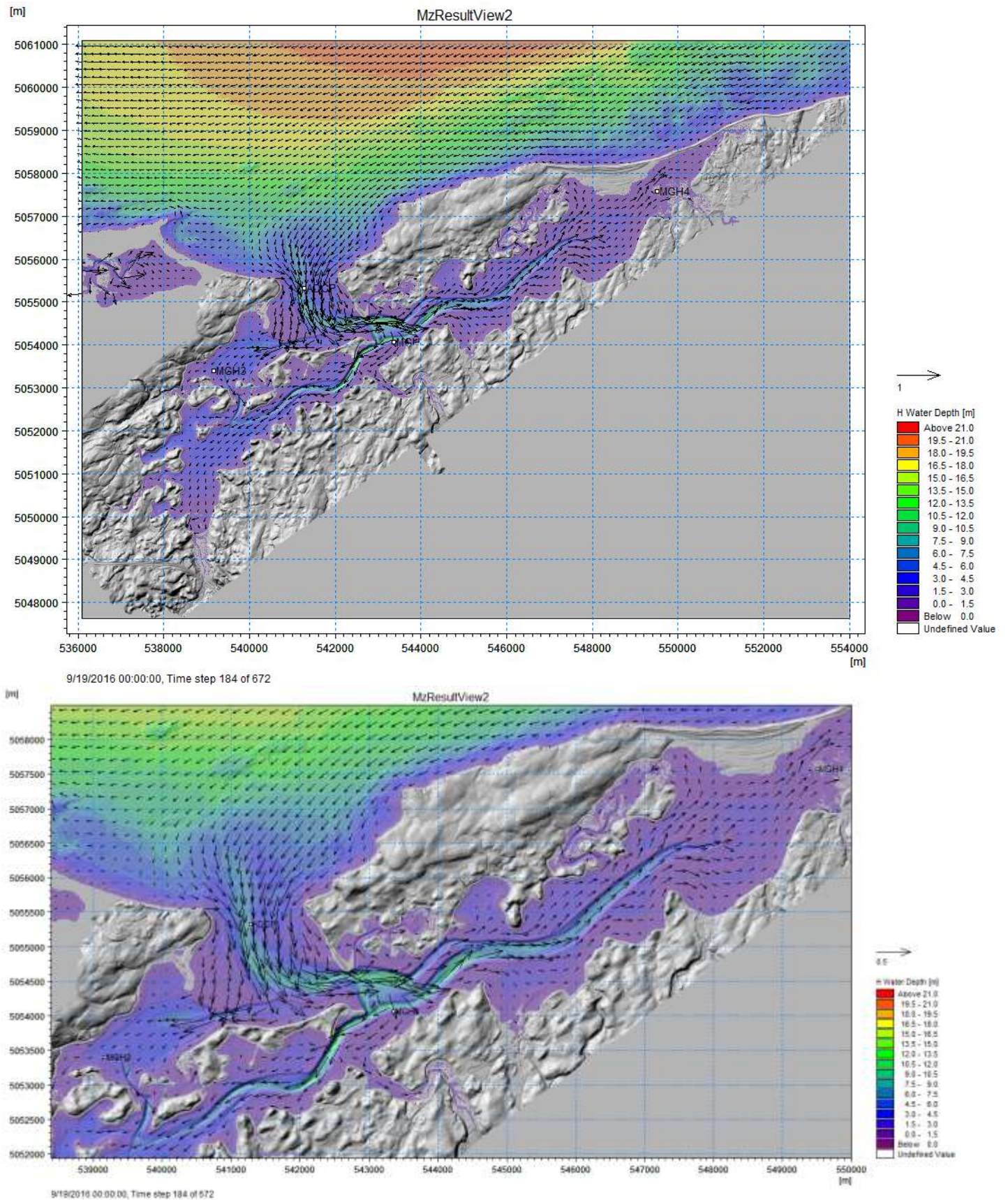


Figure 4.21: Merigomish model results for (top) Domain 1, and (bottom) cropped to an area near the ADCP and water level sensors during maximum flood tide on Sept. 19 at 00:00. The contour map is water depth and the vectors represent current speed and direction.

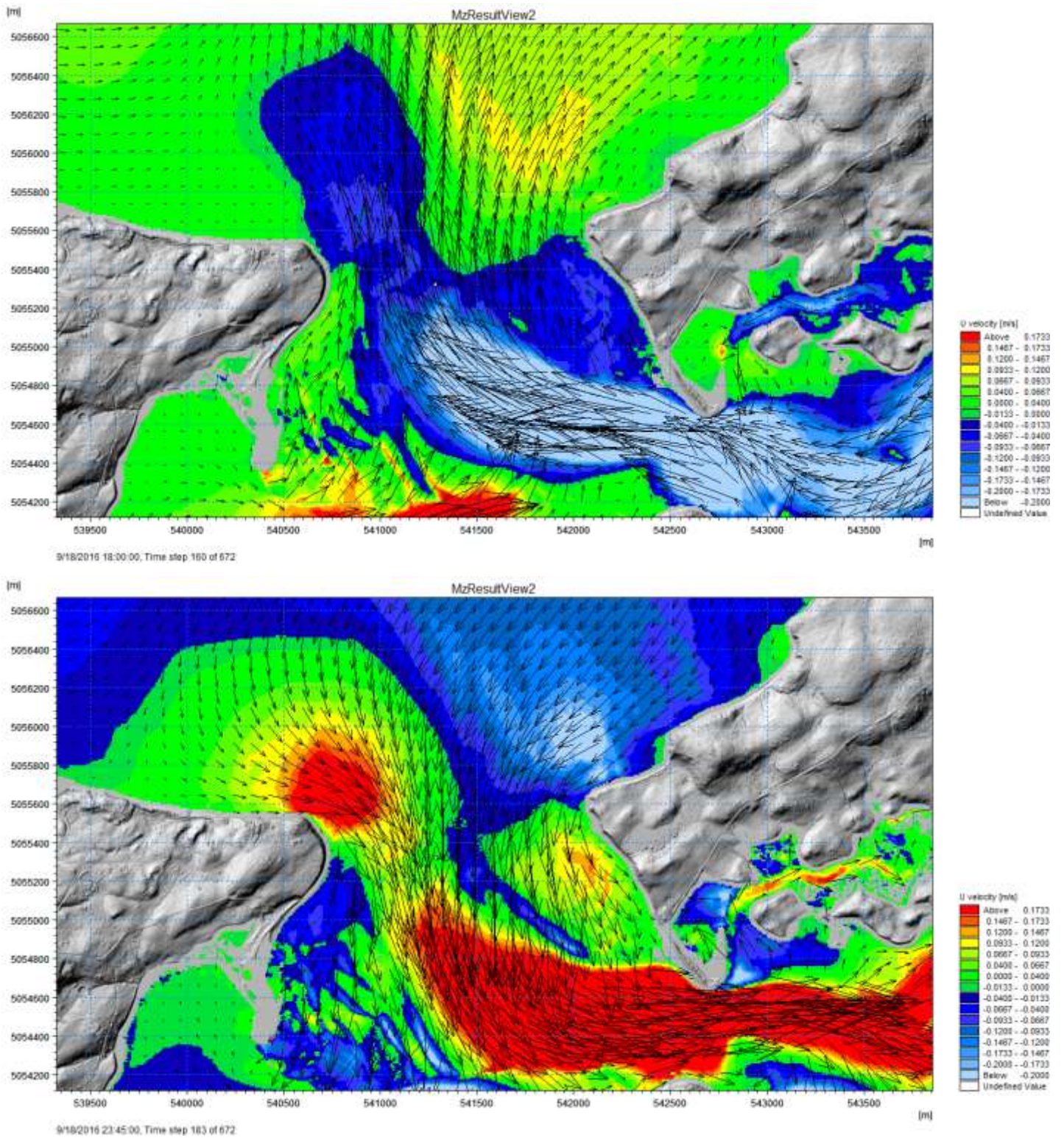


Figure 4.22: Current vectors at (top) ebb tide and (bottom) flood tide draped over EW current speed (U velocity).

4.2.3 Mabou

The modelled overpredicted surface elevation at Mabou by approximately 0.10 m, but phase was well matched (Figure 4.23). The ADCP (deployed at approximately 3 m depth, location shown on Figure 2.4) observations of current were quite different, and far more complex, from the simple sinusoidal tidal signal recorded at PWRP and Merigomish. At low slack tide the current observed at the ADCP “spiked” in both current directions, changing very rapidly from slack tide and its low current to 0.1 m/s to the northwest and then back to the southeast; this signal is seen in the east-west, north south, magnitude and direction panels of Figure 4.23. The morphology of the inlet, along with the placement of the ADCP on the edge of a slope, are likely contributors to the unusual flow patterns, and explain why model parameterizations for Mabou differed from the PWRP and Merigomish model parameterizations. Given the nature of the observations, it makes sense that the Mabou model simulations were very sensitive to changes in the eddy viscosity scheme. Model results show good comparison with the overall nature of flow at the ADCP in Mabou, with agreement in timing and amplitude of the rotation at low tide, agreement of current magnitude on the flood tide; however, current amplitude was underestimated on the ebb tide. A closer look at the currents measured at 0.25 m bins through the 3 m deployment shows homogeneity through the water column on the flood tide, but a great deal of variation, especially in the north-south currents, on the ebb tide (Figure 4.24). This further illustrates the complex nature of flow in Mabou, and helps explain why the model simulated the flood tide better than the ebb tide.

Two dimensional model results show water flowing north up the shore of Cape Breton out past the 14 m contour on the flood tide and turning towards Mabou Harbour as the bathymetry shallows (Figure 4.25). Some of the water flows through the channel and into Mabou Harbour as a jet, partially splits off into eddies on either side of the channel, while still continuing upstream at reduced velocity; some of the flow outside the harbour rotates to the south and flows along the shallow coastal water. During the ebb tide water follows a similar but opposite eddy pattern before entering the channel and leaving the harbour; water outside the harbour flows north from the shore out to past the 14 m contour (Figure 4.26). Flow coming out of the Mull River diminishes in speed past the bridge at flood tide, but maintains velocity farther into the harbour on the ebb tide.

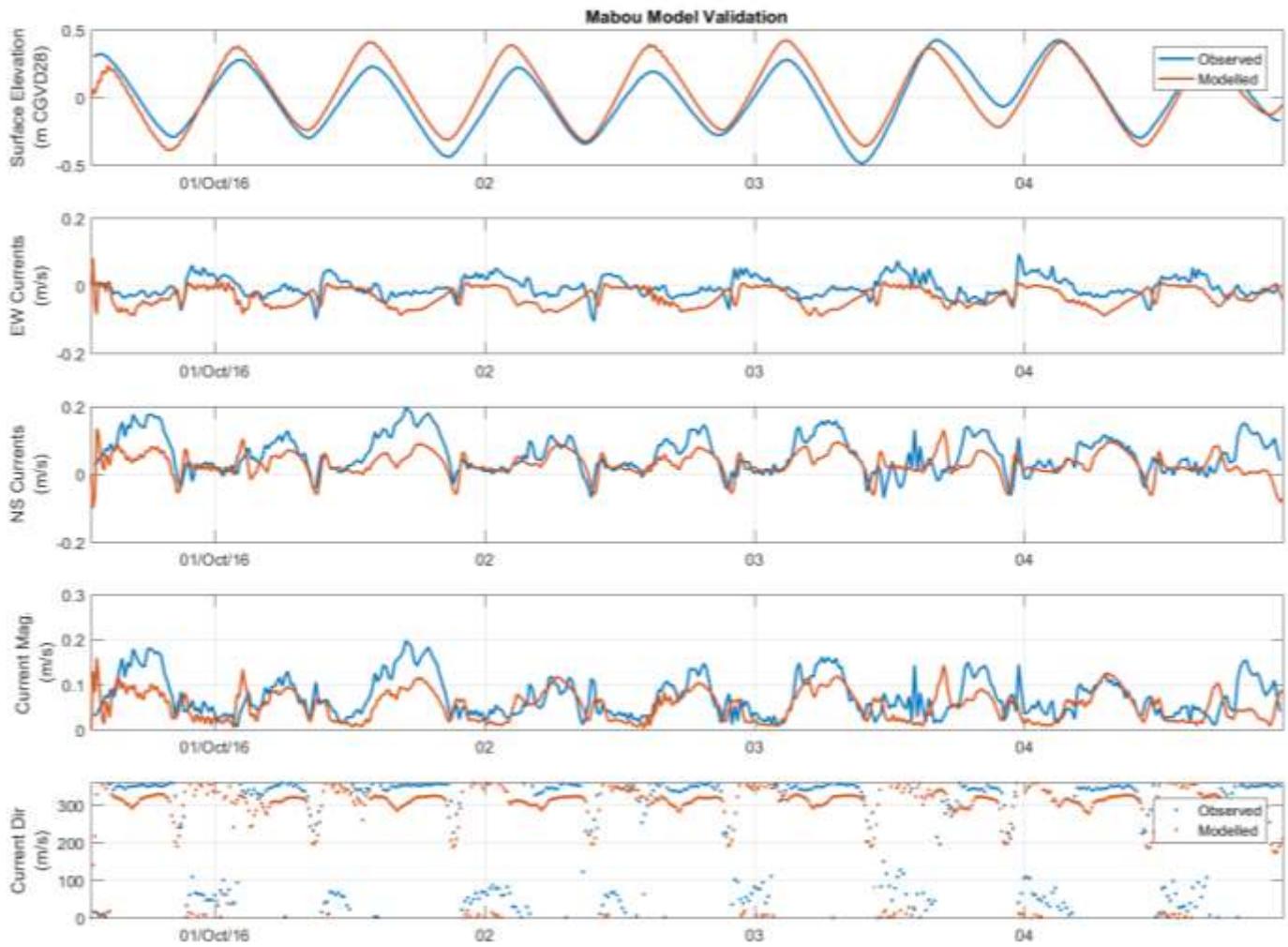


Figure 4.23: Mabou modelled and observed surface elevation and currents.

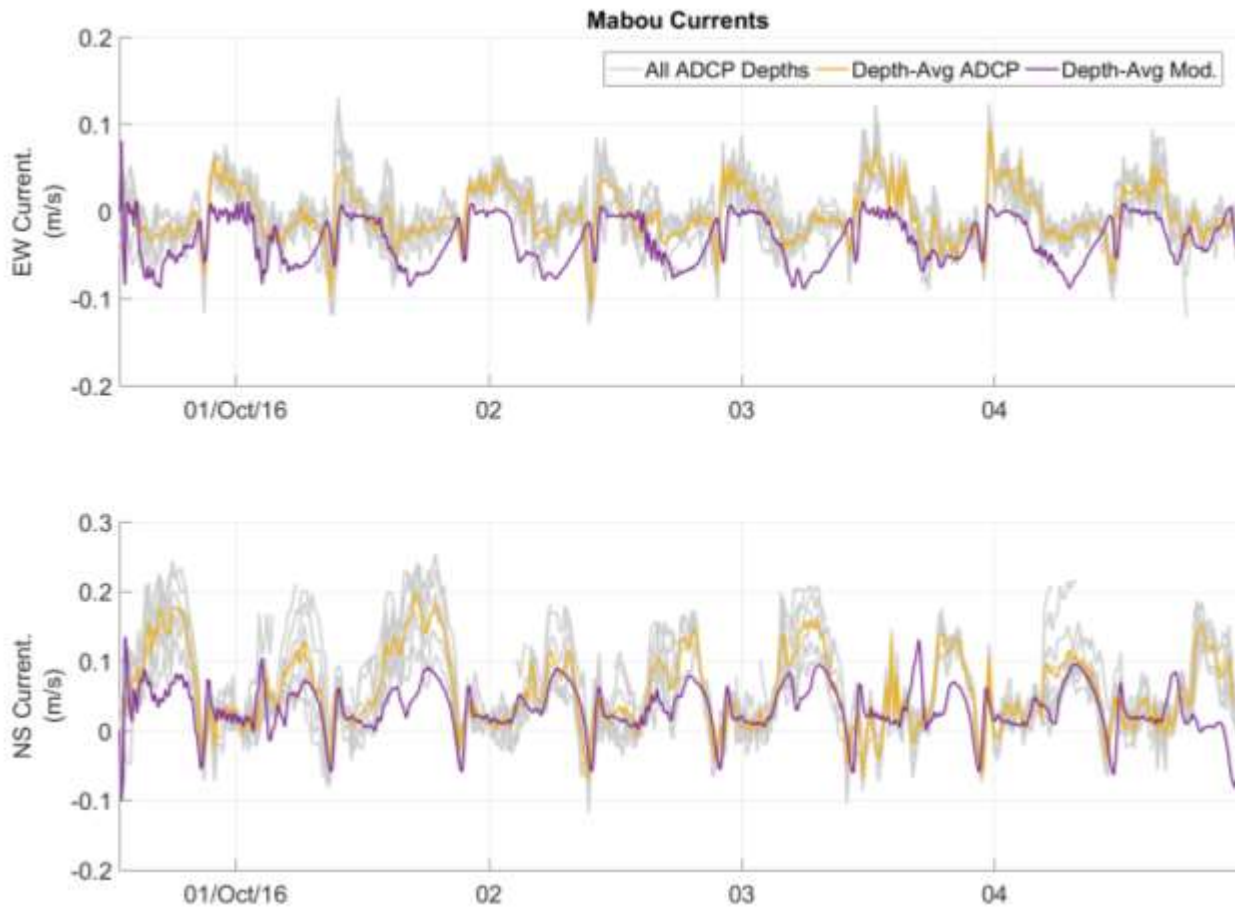


Figure 4.24: Comparison of Mabou depth-averaged currents to currents observed by the ADCP at all depths.

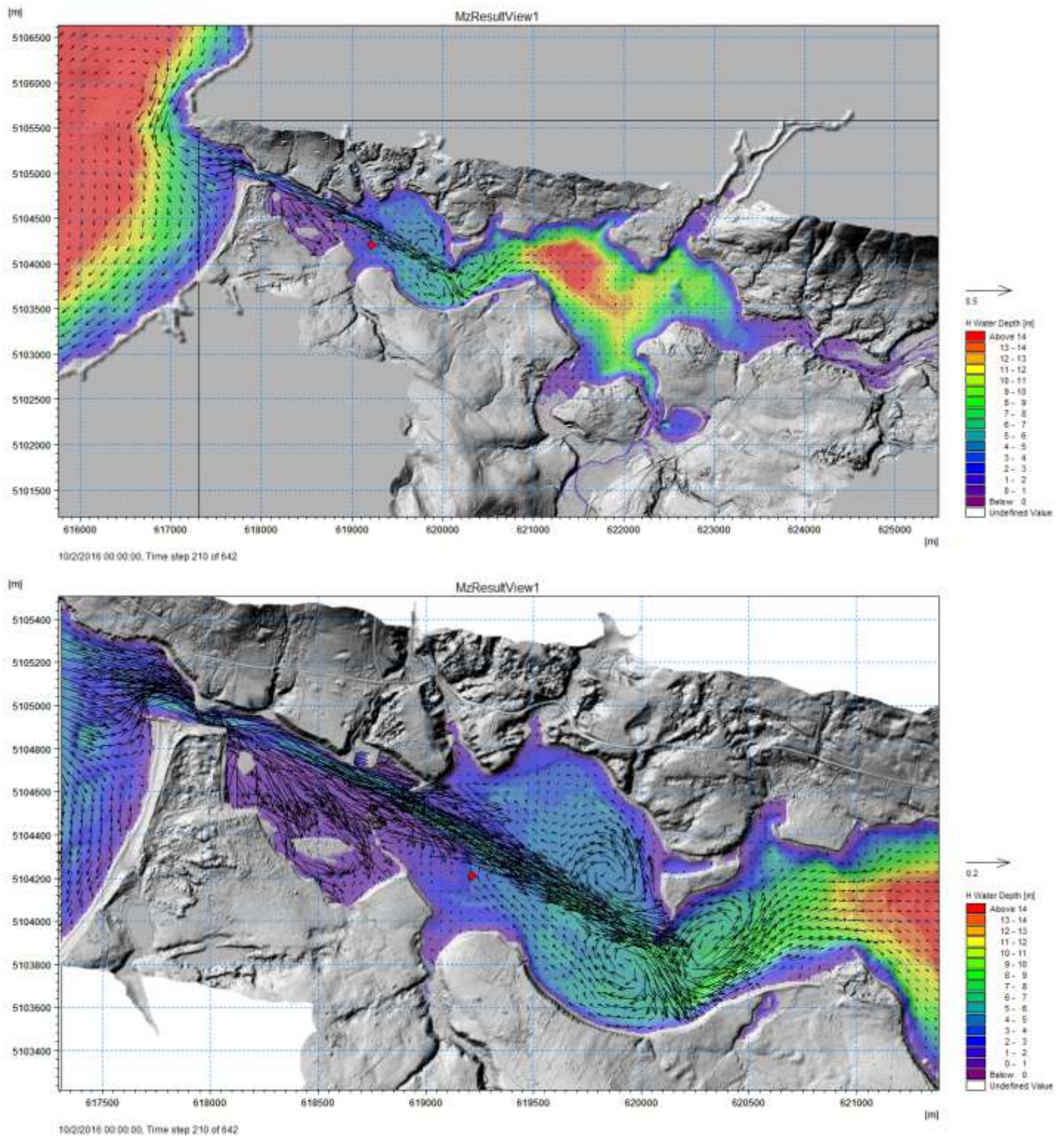


Figure 4.25: Mabou model results for (top) Domain 1, and (bottom) cropped to an area near the ADCP during maximum flood tide on Oct. 2 at 6:00. The contour map is water depth and the vectors represent current speed and direction.

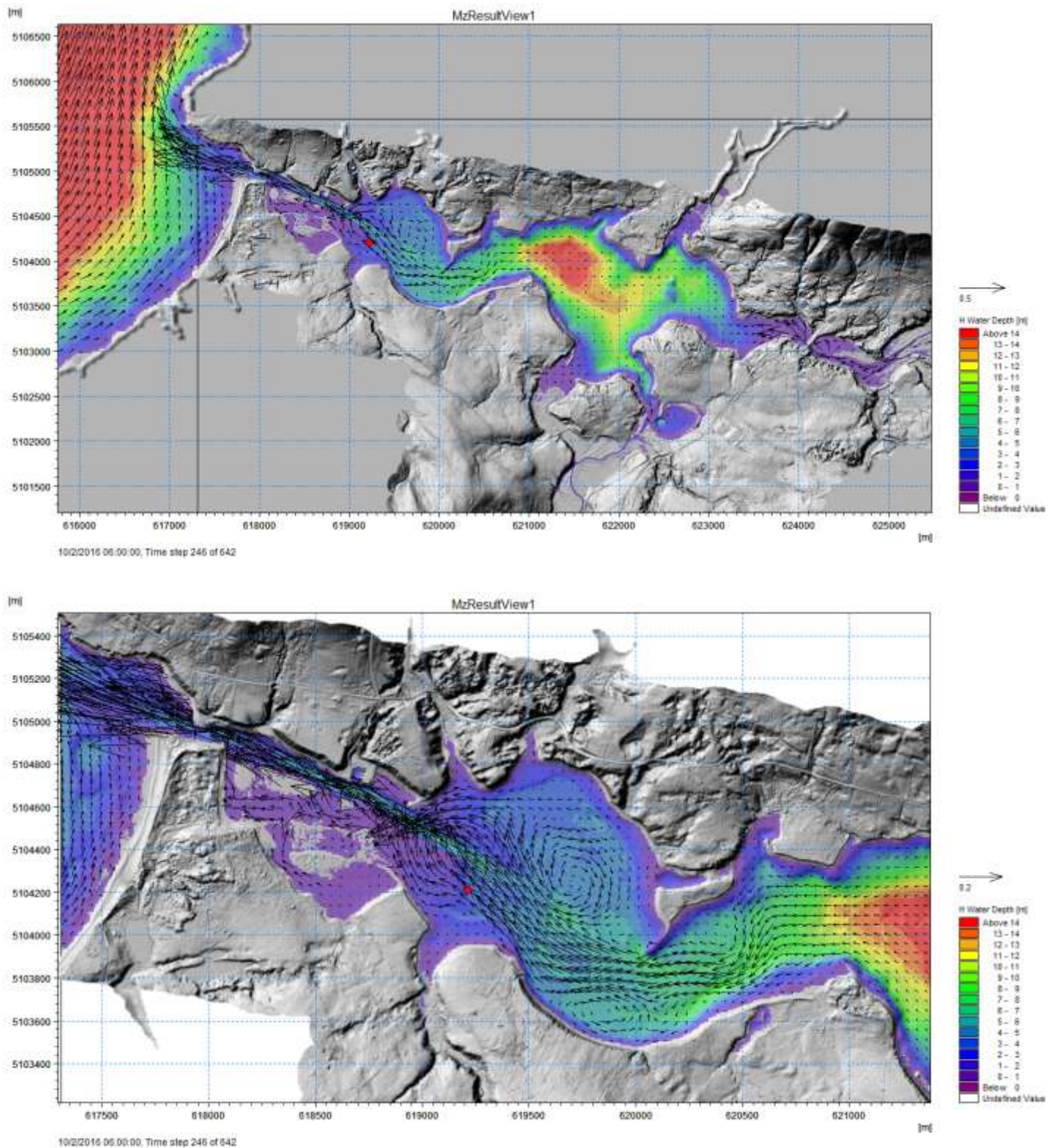


Figure 4.26: Mabou model results for (top) Domain 1, and (bottom) cropped to an area near the ADCP during maximum ebb tide on Oct. 2 at 00:00. The contour map is water depth and the vectors represent current speed and direction.

5 Discussion and Conclusions

The lidar survey at PWRP was successful in penetrating to the seabed up to ~-5 m CGVD28 (all elevations referenced to CGVD28) in coastal waters, which is in accordance with similar study areas along the Northumberland Strait, and penetrated to the edge of the river channel in Pugwash River and River Philip. A combination of depth (up to 10 m deep) and water clarity prevented the lidar from penetrating to the river channels. The study area was mainly shallow, with 58% of the lidar elevations falling between -1 and 0 m elevation. 27 % of the study area was classified as eelgrass, with an 80% agreement with ground truth data. Features such as submerged sand ripples and river tributaries are revealed in the lidar and photo products. The hydrodynamic model was validated by ADCP data and simulated tidal flow throughout the estuary, showing depth-averaged current speeds and directions at each 9 m model cell during a two day simulation period.

In Merigomish Harbour the lidar penetrated to the seabed in most of the harbour outside of the deep channels, and maximum lidar penetration was ~-6.5 m near the seaward edge of the study area. The study area consisted of mainly shallow regions, with 66% of the lidar elevations falling between -2 and 0 m CGVD28. 33 % of the study area was classified as eelgrass, with an 83% agreement with ground truth data, both underwater imagery and acoustic data. Features such as dense eelgrass beds evolving coastal morphology are revealed in the lidar and photo products. The hydrodynamic model bathymetry was completed with the support of CHS multibeam bathymetry to fill in the missing lidar data in the deep channel; the model was validated by ADCP data and simulated tidal flow throughout the estuary. The model allows the user to access depth-averaged current speeds and directions at each 9 m model cell during a seven day simulation period.

At Mabou Harbour the lidar penetrated to ~-13 m in the clear water outside of the harbour but only to ~-6 m in the inner harbour where water clarity was poor. At Mabou the lidar coverage in the rivers entering the harbour was excellent, but in most of the harbour coverage was limited by a combination of the steep-sided basin and suspended sediment. A real-time turbidity buoy was deployed in Mabou in advance of the flight in order to survey the estuary during optimal water clarity conditions, but poor water clarity ultimately did negatively affect lidar penetration. The hydrodynamic model bathymetry was completed with the addition of single beam echo sounding data supplied by DFO. The current observations from the ADCP showed complex and interesting current dynamics at Mabou, and the model was able to simulate those currents and surface elevations despite variations through the water column. The orthophotos and lidar products revealed a fascinating pattern of sandbars outside the harbour, and classified the pools and meanderings of the rivers entering the harbour in high relief.

The combination of aerial photographs, high resolution bathymetry, classified bottom maps, and modelled currents provides NSFA with an excellent dataset for characterizing these estuaries to enable future sustainable development.

6 References

DHI Water & Environment (2008). MIKE 21 FLOW MODEL HINTS AND RECOMMENDATIONS IN APPLICATIONS WITH SIGNIFICANT FLOODING AND DRYING.

Dupont, F., Hannah, C.G., and Greenberg, D. (2005). Modelling the Sea Level in the Upper Bay of Fundy. *Atmos-Ocean* 43, 33–47.

Varma, H., Hannah, C., MacNab, R., Costello, G., Spears, T., Woodford, W., and Delbridge, C. (2008). The Complexities in the Design and Definitions of the North West Atlantic Data Set; Searching for Rational Architecture to Implement Diverse Bathymetric Data. *Proc. Can. Hydrogr. Conf. Natl. Surv. Conf.*

Webster, T.L., McGuigan, K., Crowell, N., Collins, K., and MacDonald, C. (2016). Optimization of data collection and refinement of post-processing techniques for Maritime Canada’s first shallow water topographic-bathymetric lidar survey. *J. Coast. Res.*

7 Acknowledgements

We would like to thank Nova Scotia Fisheries and Aquaculture for funding and fieldwork support of this project. Thanks to staff from Leica Geosystems, Leading Edge Geomatics staff for operations and AGRG staff for administrative support. We would like to acknowledge CHS, especially Stephen Parsons for sharing bathymetric multibeam data, and DFO Science Gulf Region, especially Marc Ouellette, Monique Niles, and Thomas Guyondet, for conducting fieldwork and sharing fieldwork data.

8 Appendix: Oceanographic Data

8.1 ADCP

Three Acoustic Doppler Current Profiler (ADCP) instruments were deployed for this project during the field season to be used for hydrodynamic model validation. The data recorded by each instrument are presented in the figures in this section.

8.1.1 PWRP

An RDI Sentinel V 20, 1000 kHz ADCP was deployed by AGRG at Pugwash in ~3.9m depth on Aug 5 2016 and recovered on Sept 9 2016. Data were recorded in 0.30 m depth bins and processed using RDI's Velocity software to remove side-lobe interference and to average pings. ADCP observed depth compared well to predicted tidal elevations from the nearest tide station at Pugwash; (Figure 8.1). Depth averaged current during the deployment ranged from ~-0.2 m/s south to ~0.2 m/s north, and ~-0.2 m/s west to ~0.2 m/s east and varied in strength through the tidal cycle (Figure 8.2, Figure 8.3). Currents were uniform throughout depth (Figure 8.3).

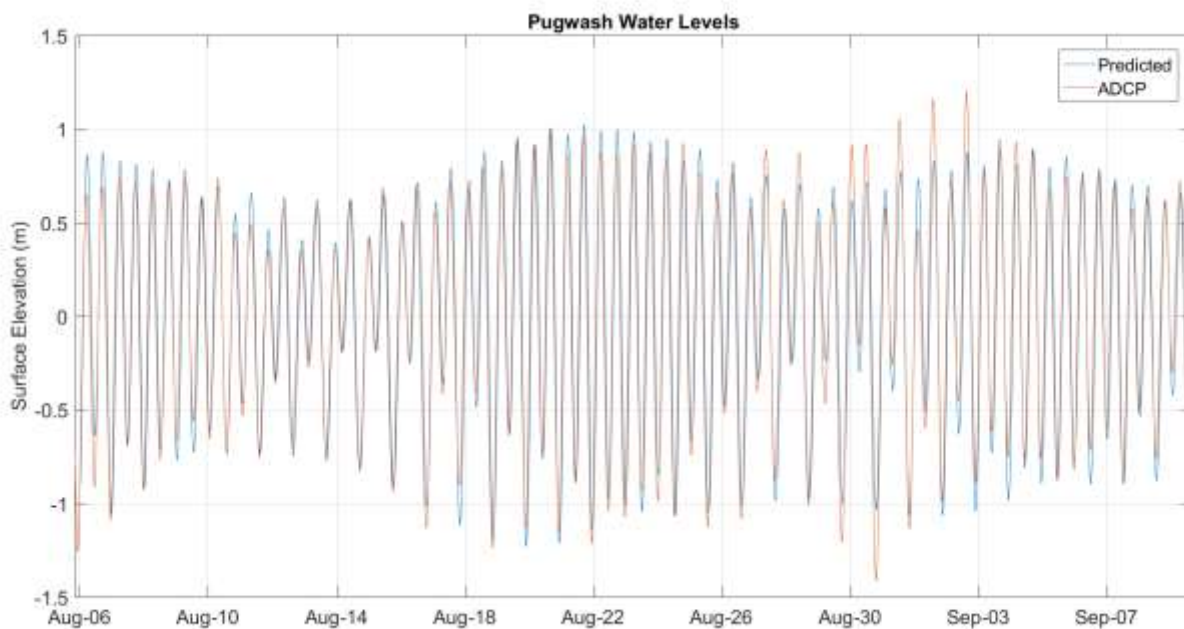


Figure 8.1: Predicted tidal elevation for Pugwash and observed tidal elevation as recorded by the ADCP.

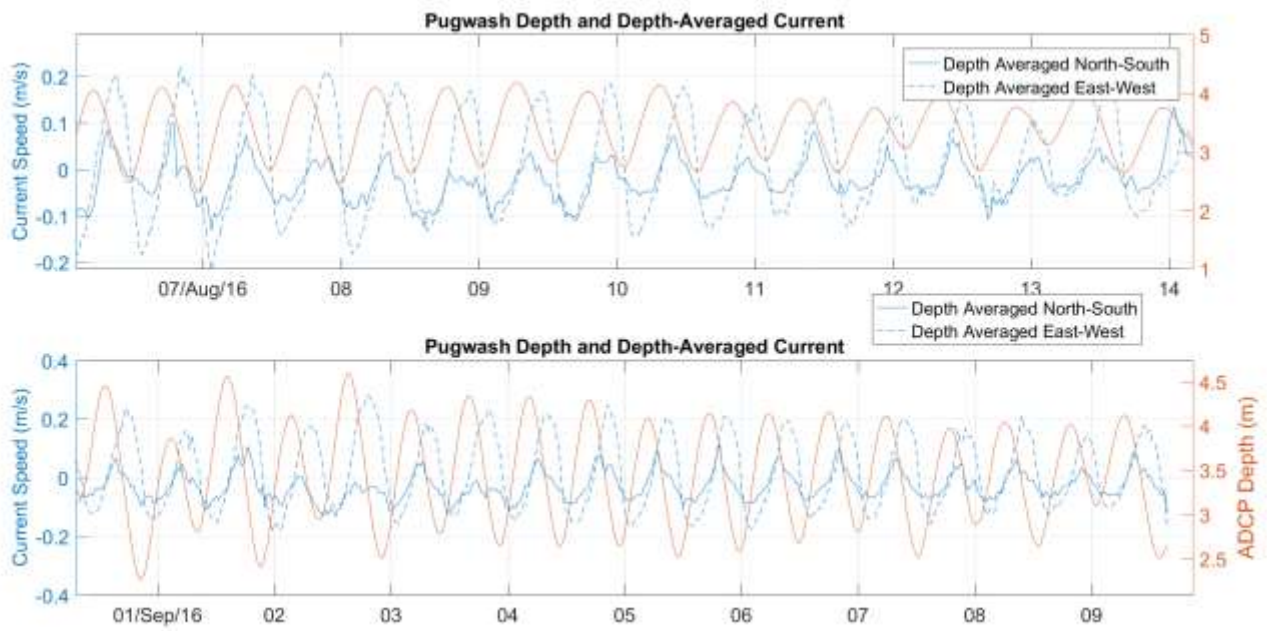


Figure 8.2: Depth averaged current speeds at Pugwash on the left y-axis with NS: solid blue line, EW: dashed blue line; ADCP depth on the right y-axis with solid orange line.

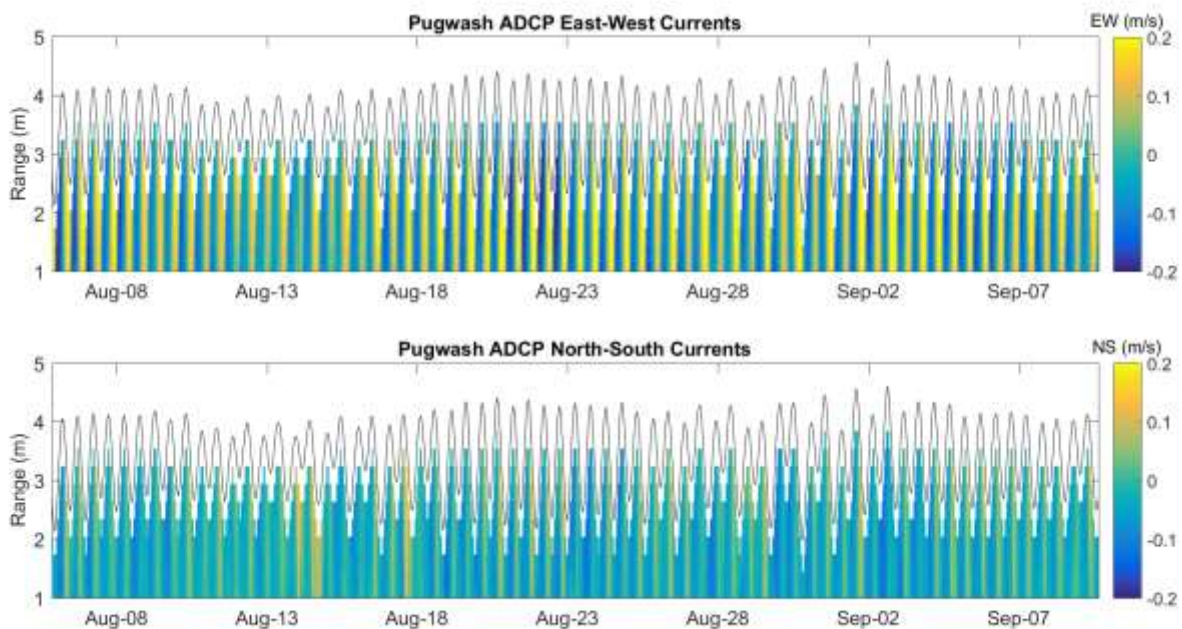


Figure 8.3: Contour plots of EW (top panel) and NS (lower) currents at Pugwash, with observed depth plotted as a black line. Current speed is represented by colour. The y-axis represents range away from the ADCP, the x-axis represents time.

8.1.2 Merigomish

An RDI Workhorse, 1229 kHz ADCP was deployed by DFO Science Gulf Region at Merigomish in ~6.6 m depth on Sept 7 2016 and recovered on Nov 22 2016. Data were recorded in 0.50 m depth bins and processed using RDI's Velocity software to remove side-lobe

interference and to average pings. ADCP observed depth did not compare well to predicted tidal elevations from the nearest tide station at Merigomish, and was not used for further analysis, but the Hobo water level sensors agreed well with each other and with the predicted tide (Figure 8.4). A ~1 m storm surge was recorded on Oct 11 that had north currents reaching ~0.9 m/s (Figure 8.4, Figure 8.5). Depth averaged current during the deployment ranged from ~-0.5 m/s south to ~0.5 m/s north, and ~-0.5 m/s west to ~0.9 m/s east (Figure 8.5, Figure 8.6). Current magnitude varied through the month with the tidal cycle, and currents were not continuously uniform throughout depth (Figure 8.6).

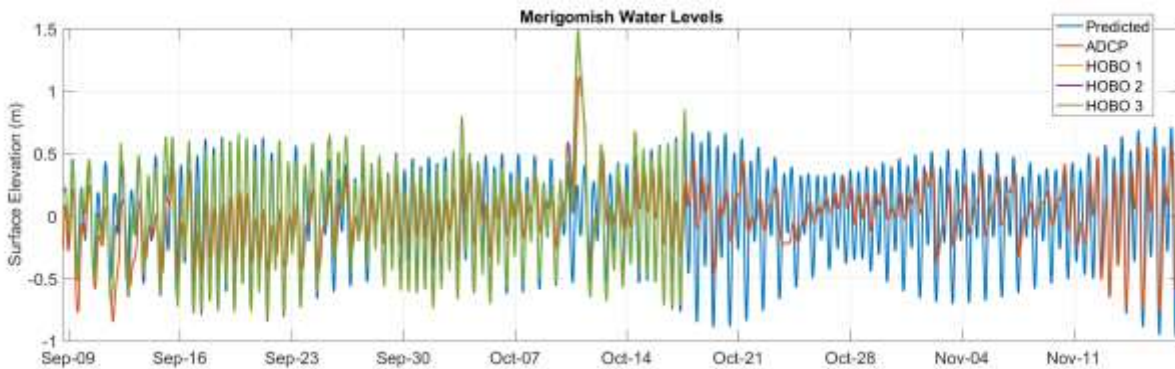


Figure 8.4: Predicted tidal elevation for Merigomish, observed tidal elevation as recorded by the ADCP and the three Hobo water level sensors.

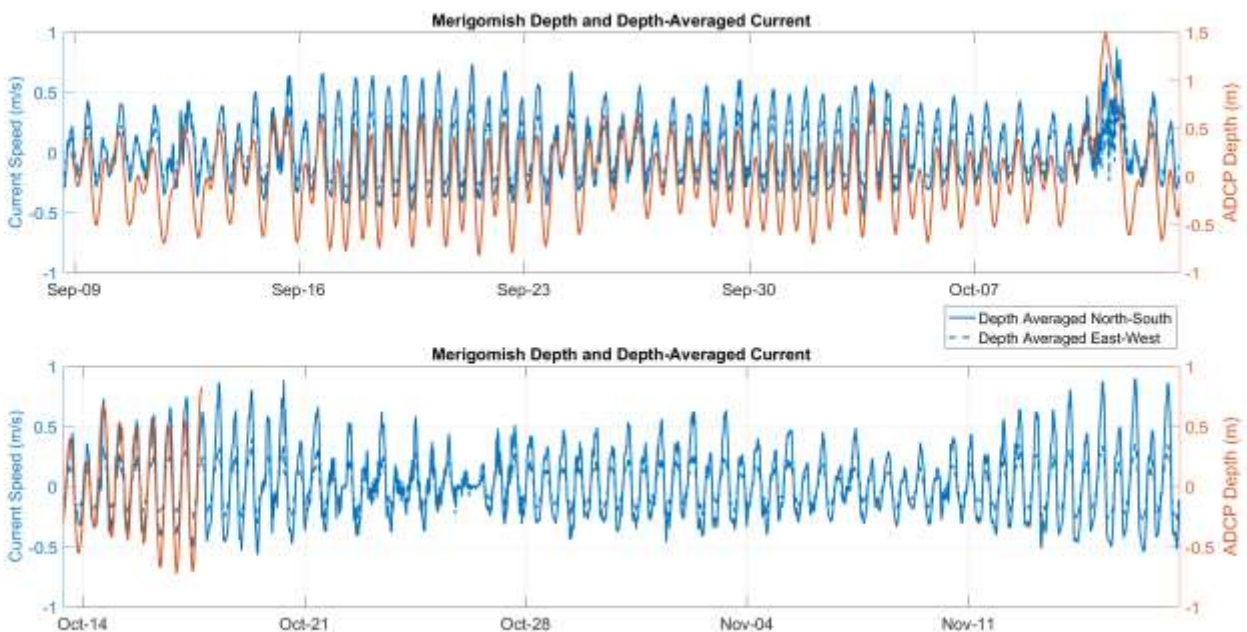


Figure 8.5: Depth averaged current speeds at Merigomish on the left y-axis with NS: solid blue line, EW: dashed blue line; ADCP depth on the right y-axis with solid orange line.

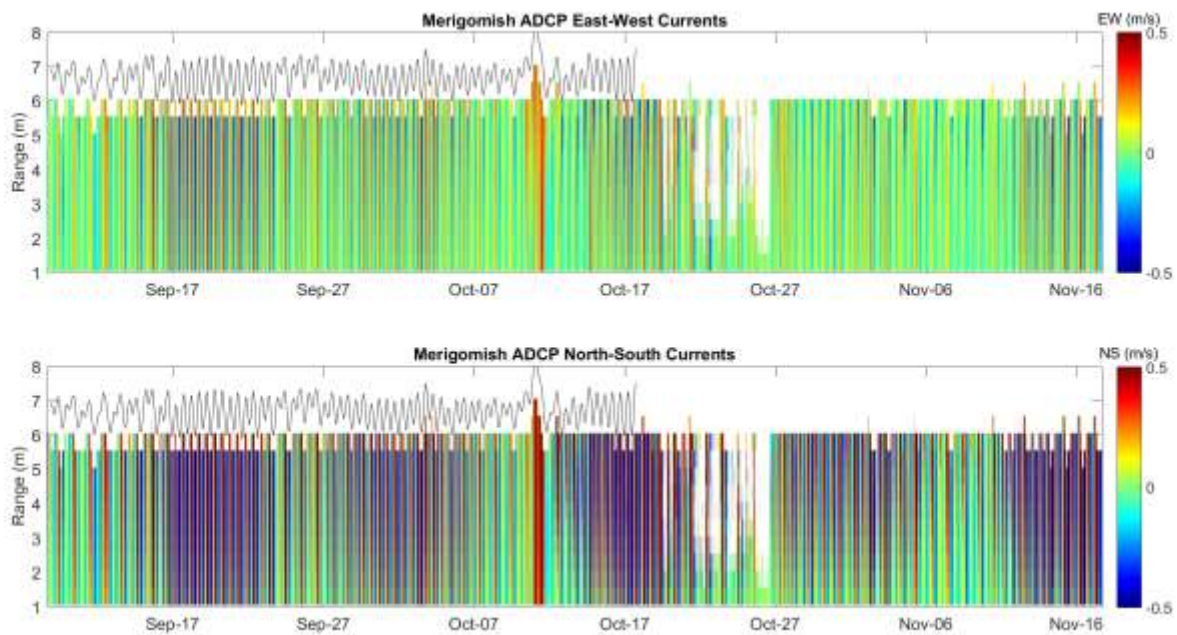


Figure 8.6: Contour plots of EW (top panel) and NS (lower) currents at Merigomish, with depth observed by MGH1 plotted as a black line. Current speed is represented by colour. The y-axis represents range away from the ADCP, the x-axis represents time.

8.1.3 Mabou

An RDI Sentinel V 20, 1000 kHz ADCP was deployed by AGRG at Mabou in ~3m depth on Sept 15 2016 and recovered on Oct 27 2016. Data were recorded in 0.25 m depth bins and processed using RDI’s Velocity software to remove side-lobe interference and to average pings. ADCP observed depth compared well to predicted tidal elevations from the nearest tide station at Port Hood; differences in amplitude are expected given the difference in the two locations (Figure 8.7). A ~1 m storm surge was recorded on Oct 11 that had north currents reaching ~0.35 m/s (Figure 8.7, Figure 8.8). Depth averaged current during the deployment ranged from ~-0.1 m/s south to ~0.2 m/s north, and ~0.13 m/s east to ~-0.13 m/s west (Figure 8.8, Figure 8.9). Current magnitude varied through the month with the tidal cycle, and currents were not continuously uniform throughout depth.

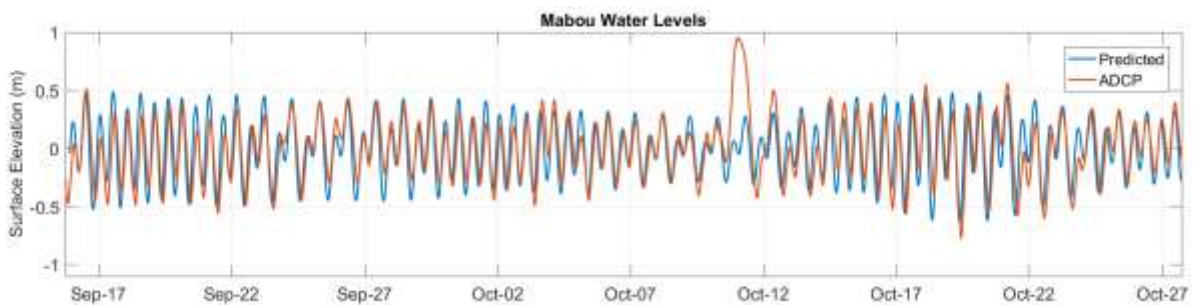


Figure 8.7: Predicted tidal elevation for Mabou and observed tidal elevation as recorded by the ADCP.

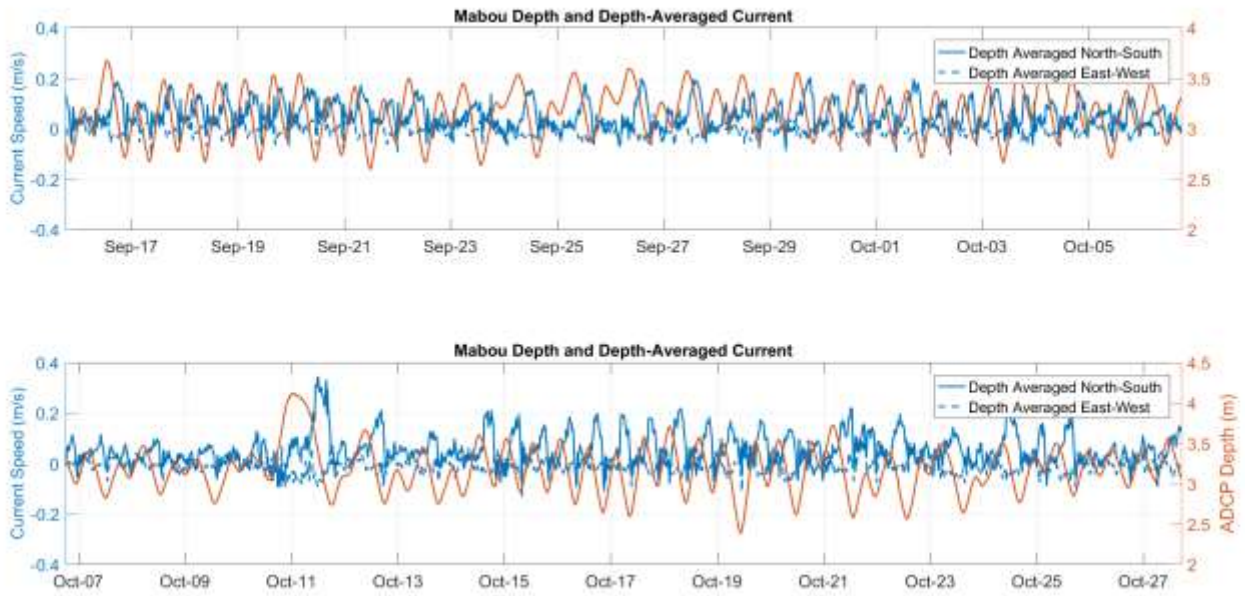


Figure 8.8: Depth averaged current speeds at Mabou on the left y-axis with NS: solid blue line, EW: dashed blue line; ADCP depth on the right y-axis with solid orange line.

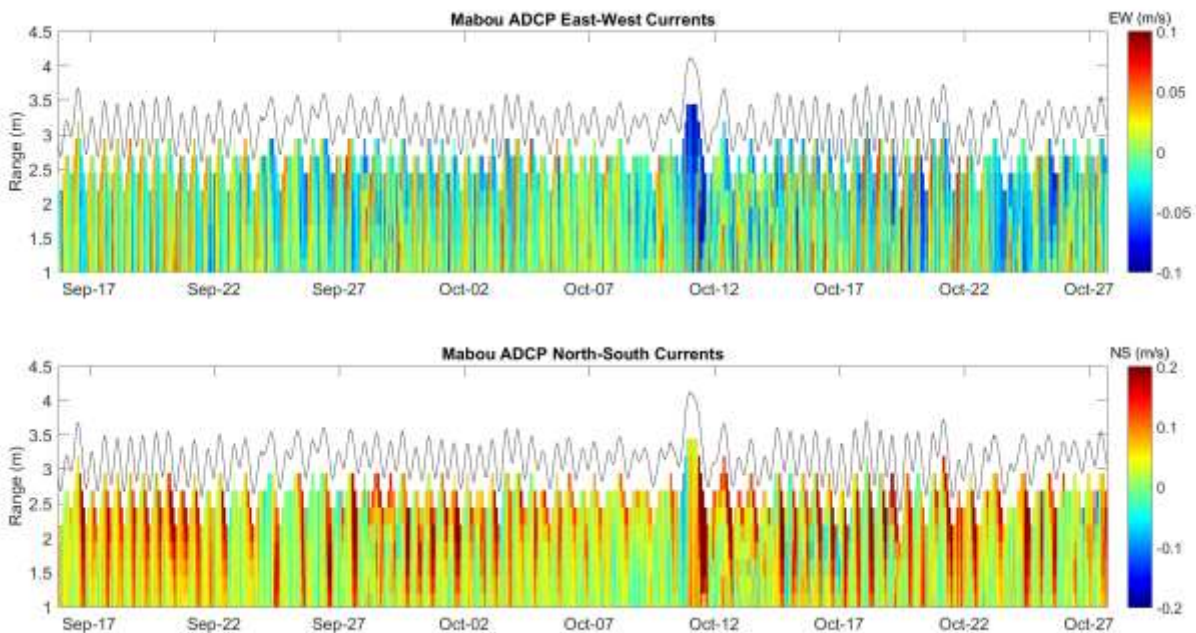


Figure 8.9: Contour plots of EW (top panel) and NS (lower) currents at Mabou, with observed depth plotted as a black line. Current speed is represented by colour. The y-axis represents range away from the ADCP, the x-axis represents time.

CTD

A Seabird 25plus Conductivity Temperature Depth (CTD) sensor was used during the ground truth surveys at Pugwash and Mabou to measure changes in salinity, temperature, turbidity and chlorophyll through the water column across the study area. The CTD data provided insight into the structure of the water column, e.g. whether it was well-mixed or stratified; this information was valuable in evaluating lidar penetration. The data also provided an additional depth validation method. The data recorded by each instrument are presented in the figures in this section.

8.1.4 PWRP

Five CTD profiles were collected in the Pugwash River on July 7, ranging in depth from 1 m to 9 m (Figure 8.10, Figure 8.11).

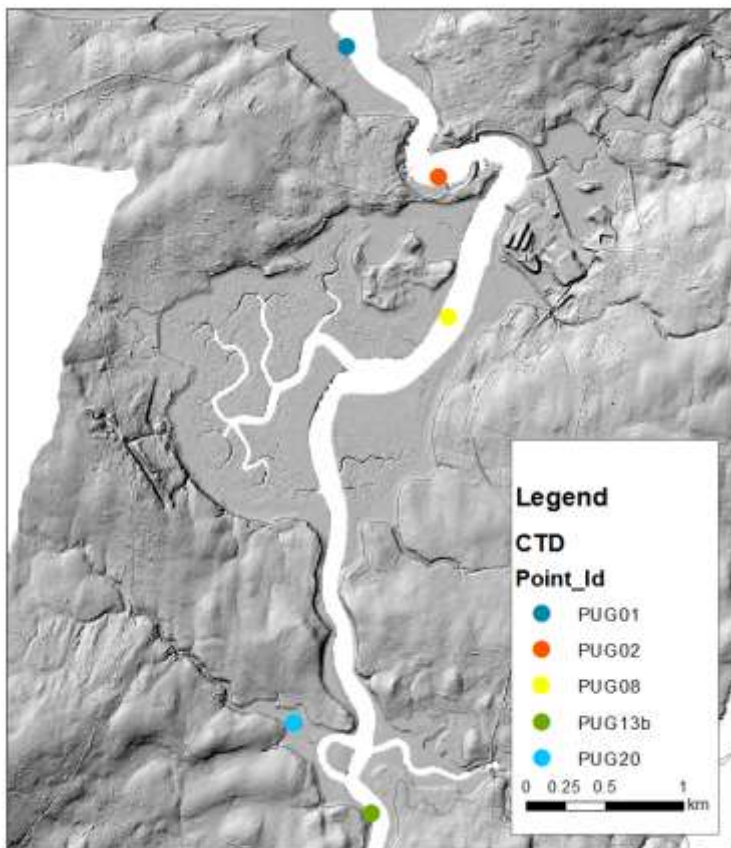


Figure 8.10: Locations and IDs of Pugwash River CTD profiles.

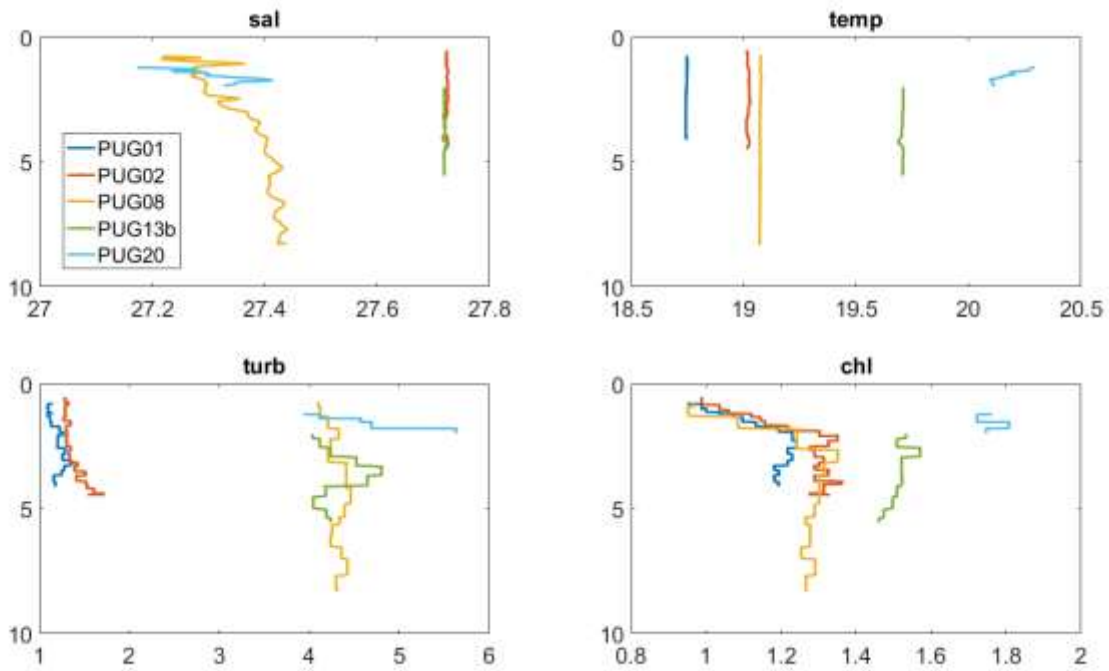


Figure 8.11: Results of CTD depth profiles for salinity (in PSU), temperature (in °C), turbidity (in NTU), and chlorophyll (unitless). Each y-axis represents depth and each x-axis represents the parameter being measured.

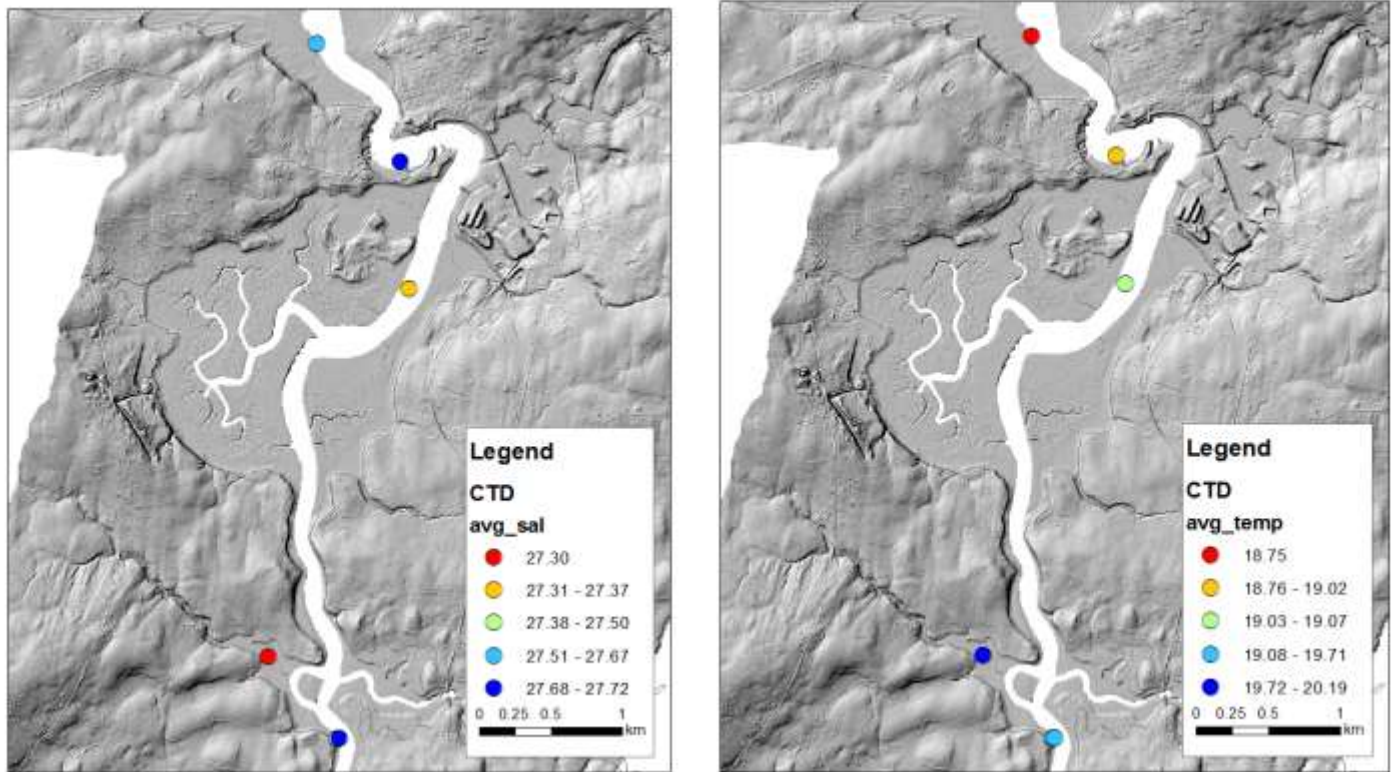


Figure 8.12: Depth averaged salinity (left); and temperature (right) turbidity at each CTD profile location.

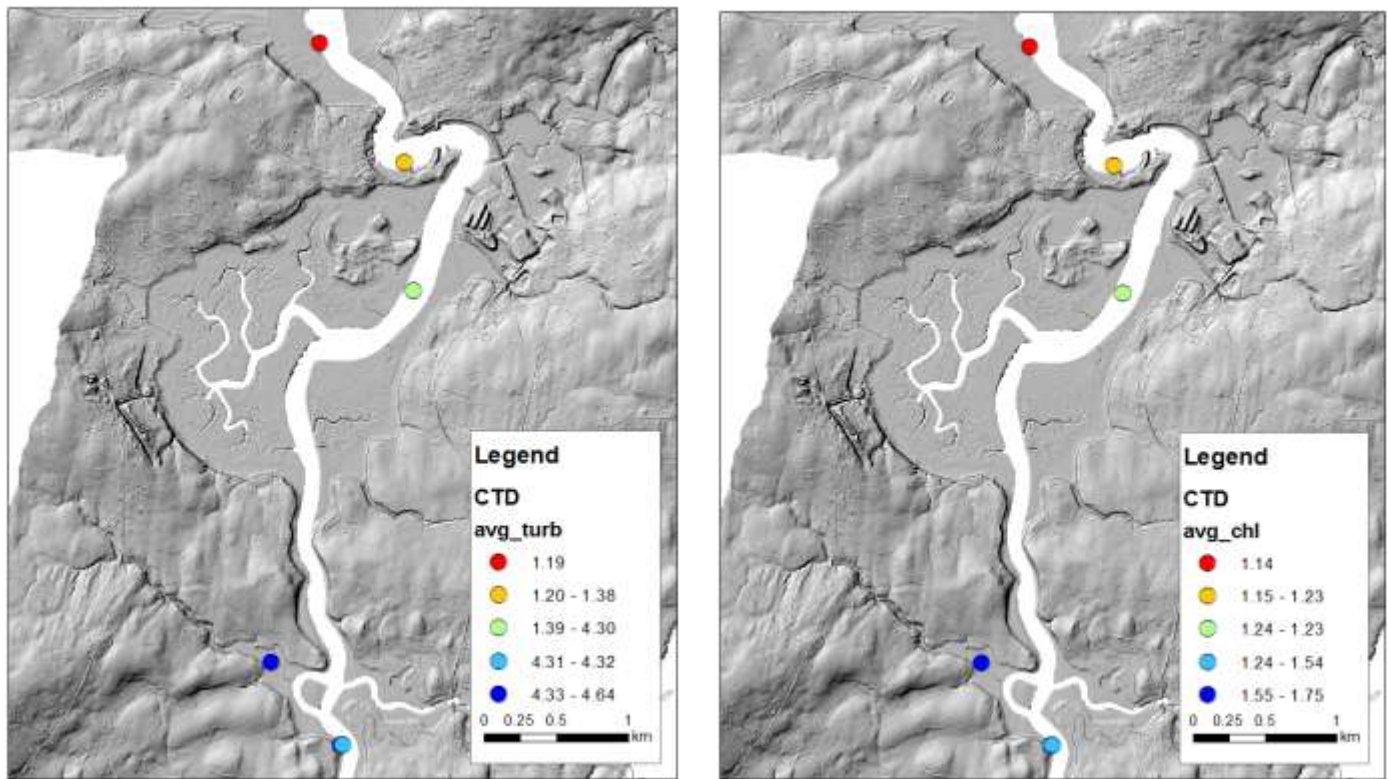


Figure 8.13: Depth averaged turbidity (left); and chlorophyll (right) turbidity at each CTD profile location.

8.1.5 Mabou

Nineteen CTD profiles were obtained on July 13 and July 21 at Mabou, ranging in depth from 1 m to 15 m (Figure 8.14, Figure 8.15).

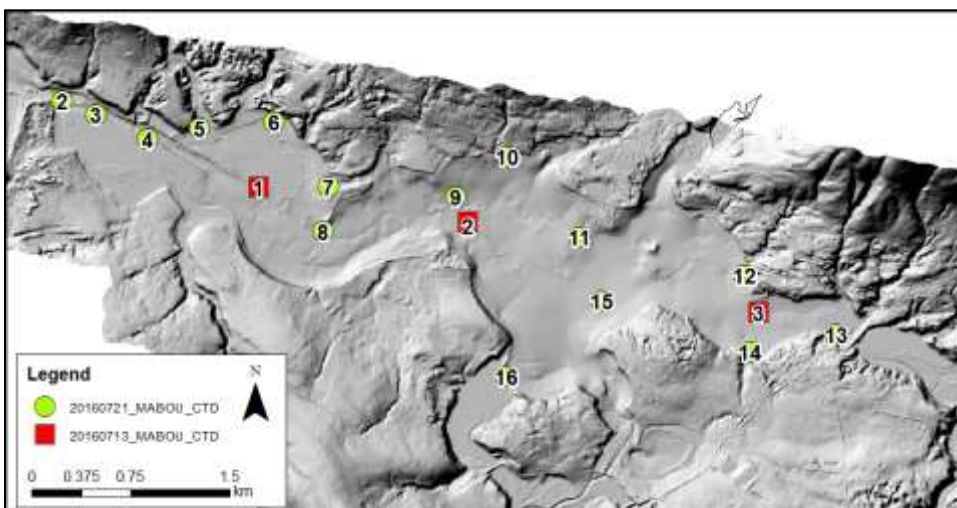


Figure 8.14: Locations and IDs of Mabou CTD profiles.

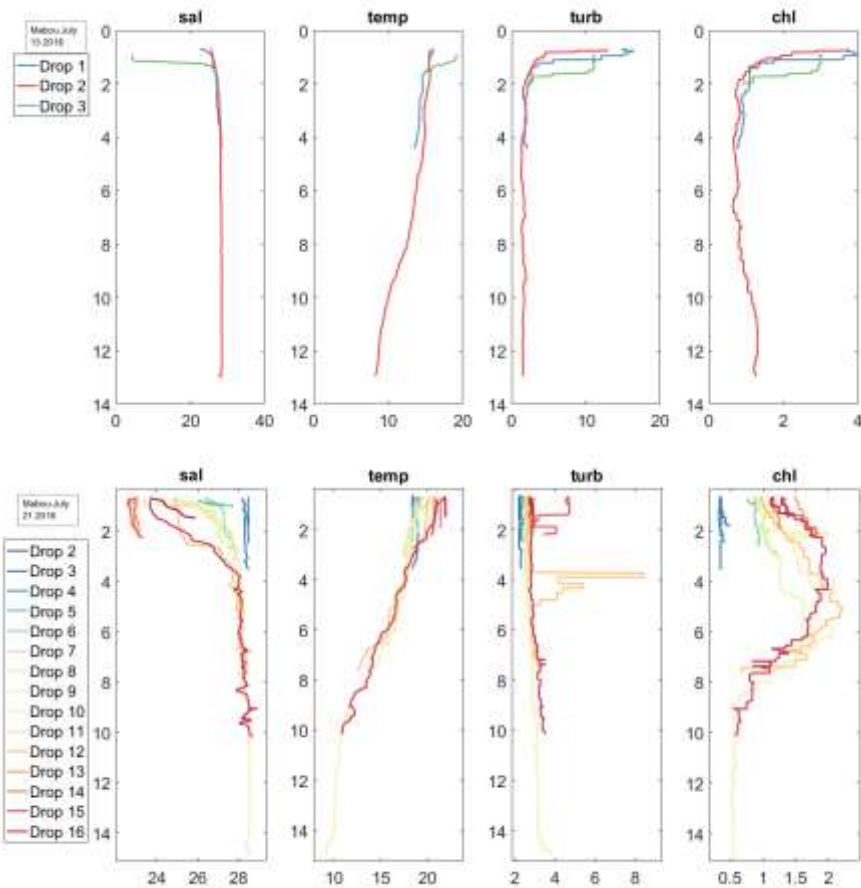


Figure 8.15: Results of Mabou CTD depth profiles for salinity (in PSU), temperature (in °C), turbidity (in NTU), and chlorophyll (unitless). Each y-axis represents depth and each x-axis represents the parameter being measured. The top panel shows data from July 13 and the lower panel shows data from July 21.

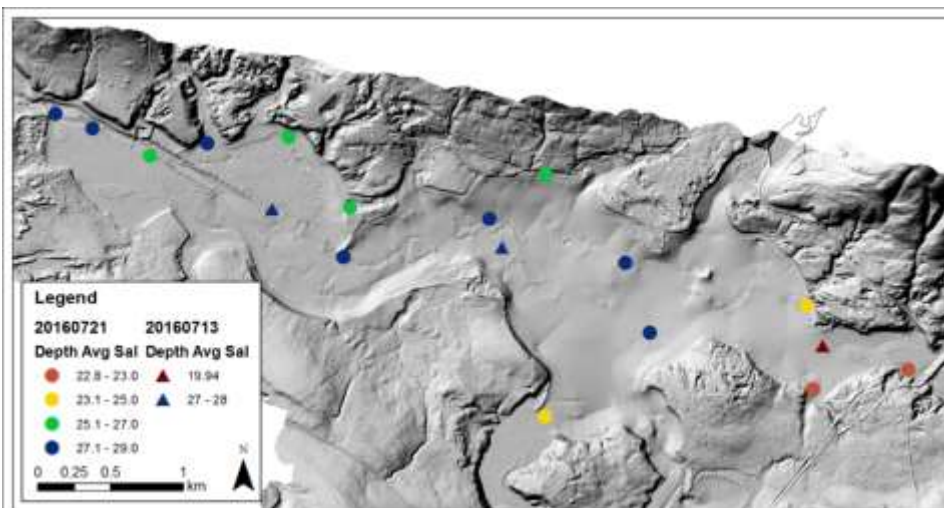


Figure 8.16: Depth averaged salinity values at each CTD profile location.

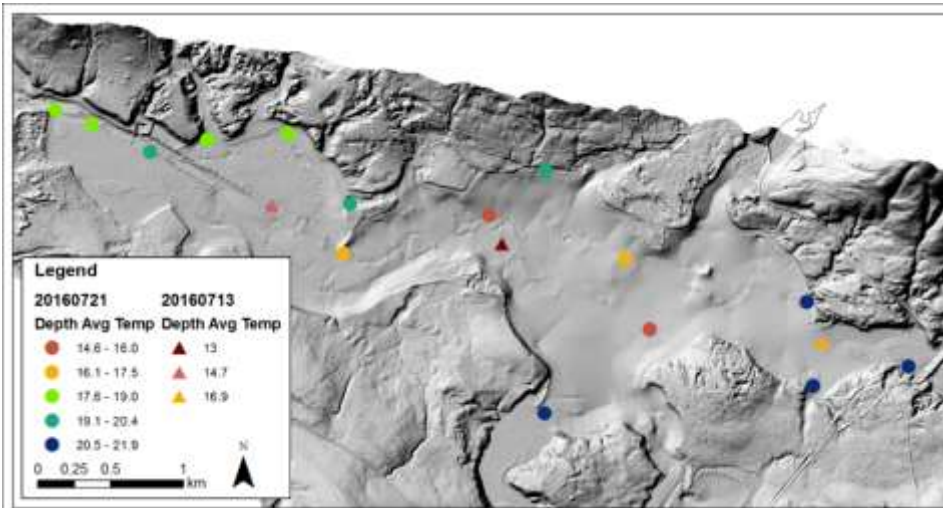


Figure 8.17: Depth averaged temperature values at each CTD profile location.

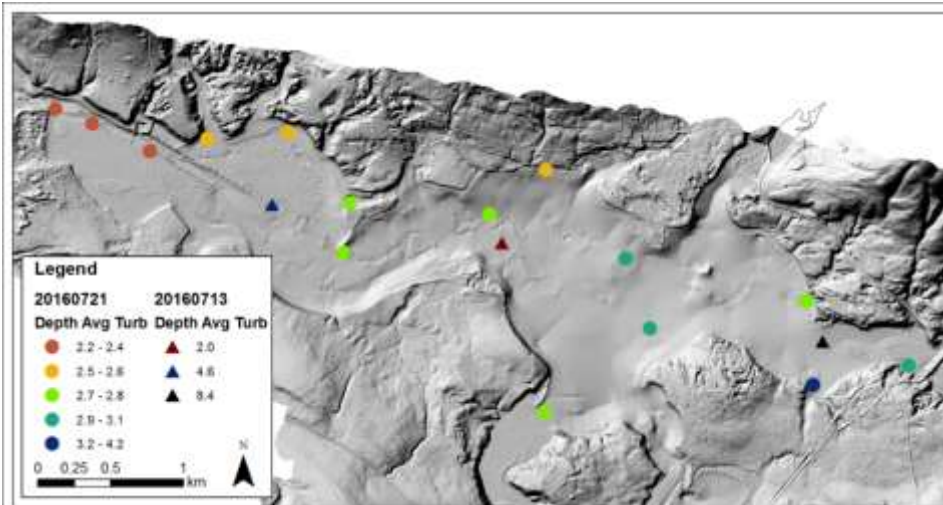


Figure 8.18: Depth averaged turbidity values at each CTD profile location.

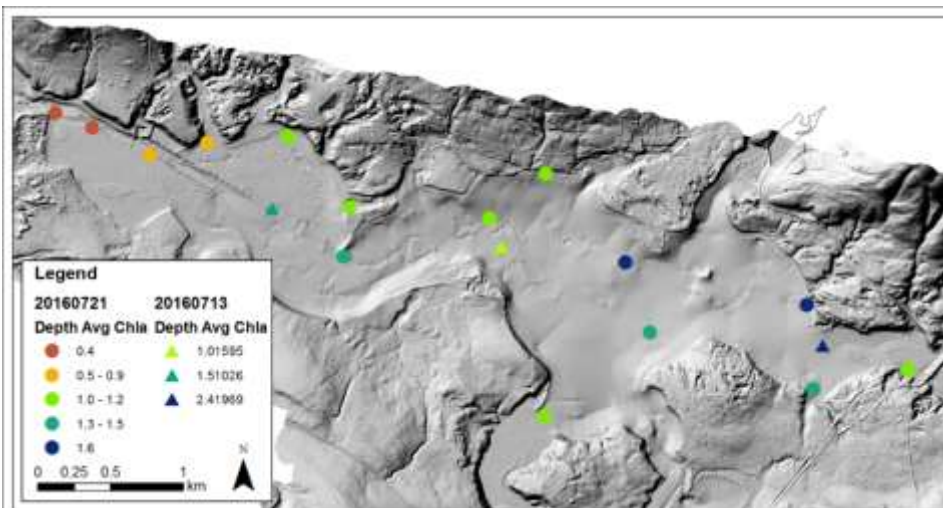


Figure 8.19: Depth averaged chlorophyll values at each CTD profile location.